

TECHNISCHE UNIVERSITÄT MÜNCHEN

Fachgebiet Organische Chemie

**Novel Methods for NMR -
Single-SHOT Correlation Spectroscopy
and
Diffusion of ^{13}C -Metabolites
utilizing both
Hyperpolarization and Optimal Control**

Franz Schilling

Vollständiger Abdruck der von der Fakultät für Chemie der Technischen Universität München zur Erlangung des akademischen Grades eines

Doktors der Naturwissenschaften

genehmigten Dissertation.

Vorsitzender:

Univ.-Prof. Dr. Bernd Reif

Prüfer der Dissertation:

1. Univ.-Prof. Dr. Steffen J. Glaser
2. Univ.-Prof. Dr. Axel Haase
3. Prof. Silvio Aime, Universität Turin/Italien

Die Dissertation wurde am 26.2.2013 bei der Technischen Universität München eingereicht und durch die Fakultät für Chemie am 9.4.2013 angenommen.

Abstract

Nuclear magnetic resonance (NMR) has outstanding potential as a non-destructive technique to study a broad range of specimens. It ranges from quantum objects like single spins over macromolecules to living organisms. Although being one of the most powerful spectroscopic techniques, NMR has been suffering from its low sensitivity ever since. Ten years ago, dissolution dynamic nuclear polarization (DNP) revolutionized the field by bringing nuclear spins into a so-called hyperpolarized state, thereby increasing NMR's sensitivity by more than four orders of magnitude. My research concentrates on the development of novel methods for NMR of hyperpolarized nuclei in combination with the numerical optimization of radiofrequency (RF) pulses by optimal control theory. Major progress of my work is a promising technique for quantitative characterization of tumor necrosis and a method for measurements of heteronuclear chemical shift correlations within a single scan. Ranging from theoretical and methodical concepts in RF pulse design to measurements of low concentrated metabolite diffusion coefficients up to the quantitative determination of lipid content in living insects, my research is structured in four sections:

- Using optimal control pulse optimization, it is shown that virtually arbitrary off-resonance scaling of the effective J -coupling constant in heteronuclear coupled spin systems can be achieved. A new class of tailored decoupling pulses named SHOT (Scaling of Heteronuclear couplings by Optimal Tracking) is introduced.
- Combining dissolution DNP with SHOT pulses effects that chemical shift correlations from hyperpolarized molecules can be accurately obtained from information contained in a single scan.
- A method for measurements of apparent diffusion coefficients (ADCs) from hyperpolarized ^{13}C -metabolites is presented. Investigations in tumor cells demonstrate that ^{13}C ADC detection can yield sensitive information on changes in membrane permeability and subsequent cell death. *In vivo* measurements employing optimal control pulses demonstrate the feasibility of this technique for preclinical research.
- In contrast to destructive conventional photometric and mass measurements, we demonstrate exemplarily in the European spruce bark beetle that NMR can be efficiently used to quantify and image absolute fat and water content in living insects.

Molecular structure, metabolic processes, and microscopic physiology are investigated by NMR in this work altogether reflecting its wealth of applications at fundamentally different scales.

Kurzzusammenfassung

Die Kernspinresonanz (NMR, engl.: nuclear magnetic resonance) bietet als zerstörungsfreie Technik herausragende Möglichkeiten zur Untersuchung einer großen Bandbreite an Proben. Diese reichen von Quantenobjekten wie einzelnen Spins über Makromoleküle bis hin zu Organismen. Obwohl sie eine der bedeutendsten spektroskopischen Techniken ist, war die geringe Sensitivität der NMR schon immer ihre Schwachstelle. Vor zehn Jahren revolutionierte die DNP-Technik (engl.: dynamic nuclear polarization) für Flüssigkeiten bei Raumtemperatur das Fachgebiet, indem Kernspins in einen hyperpolarisierten Zustand gebracht werden konnten, was zu einem Sensitivitätsgewinn von mehr als vier Größenordnungen führte. In diesem Zusammenhang konzentriert sich meine Forschung auf die Entwicklung von NMR-Methoden für hyperpolarisierte Kerne in Kombination mit der numerischen Optimierung von Radiofrequenzpulsen durch die Steuerungstheorie. Zentrale Entwicklungen meiner Arbeit sind sowohl eine Technik zur quantitativen Charakterisierung von Nekrose in Tumoren als auch eine Methode zur Messung von heteronuklearen chemischen Verschiebungskorrelationen mit einer einzigen Akquisition. In einem Bereich, welcher sowohl theoretische und methodische Konzepte der Pulsentwicklung als auch Messungen der Diffusionskoeffizienten niedrig konzentrierter Metabolite sowie die quantitative Bestimmung von Lipiden in lebenden Insekten umfasst, gliedert sich meine Forschung in vier Teile:

- Mittels steuerungstheoretischer Optimierung von Radiofrequenzpulsen wird gezeigt, dass eine praktisch beliebige Off-Resonanz-Skalierung der effektiven Kopplungskonstante J in heteronuklear gekoppelten Spinsystemen erreicht werden kann. Eine neue Klasse maßgeschneiderter Pulse namens SHOT (engl.: Scaling of Heteronuclear couplings by Optimal Tracking) wird entwickelt.
- Durch die Kombination von DNP mit SHOT Pulsen wird demonstriert, dass chemische Verschiebungskorrelationen von hyperpolarisierten Molekülen aus einer einzigen Akquisition bestimmt werden können.
- Eine Methode zur Messung von ADCs (engl. apparent diffusion coefficients) hyperpolarisierter ^{13}C -Metabolite wurde entwickelt. An Tumorzellen wird herausgestellt, dass ^{13}C ADCs sensitive Informationen über Veränderungen der Membranpermeabilität und anschließenden Zelltod liefern können. *In vivo*-Messungen auf Basis mit Steuerungstheorie optimierter Pulse stellen die Umsetzbarkeit dieser Technik für die präklinische Forschung heraus.
- Am Beispiel des Borkenkäfers wird exemplarisch dargestellt, dass NMR effizient eingesetzt werden kann, um den Fett- und Wassergehalt in lebenden Insekten zu quantifizieren und zu lokalisieren.

Molekulare Strukturen, metabolische Prozesse und mikroskopische Physiologie werden in dieser Arbeit mit NMR untersucht, welche zusammengenommen deren breites Anwendungsspektrum auf einer enorm weiten Größenordnungsskala widerspiegeln.



Contents

Abstract	i
Kurzzusammenfassung	iii
1 Introduction	1
2 Theory and Methods	7
2.1 Spin angular momentum and the density matrix	7
2.2 Heteronuclear spin decoupling	10
2.3 Optimal control of coupled spin dynamics	12
2.3.1 Outline of the GRAPE and the GRAPE tracking algorithm	13
2.4 Hyperpolarization	15
2.5 Measurement of diffusion properties by NMR	18
2.6 Magnetic Resonance Imaging	20
3 Tailored real-time scaling of heteronuclear couplings	25
Summary	25
3.1 Introduction	26
3.2 Theory	27
3.3 Results	30
3.3.1 Linear J scaling as a function of offset	30
3.3.2 Arbitrarily tailored J scaling as a function of offset	33
3.3.3 Chemical shift correlations from linear scaling of heteronuclear couplings	37
3.4 Discussion and conclusion	41
3.5 Acknowledgements	43
3.6 Appendix A: Gradient for the optimization of amplitude-modulated J scaling sequences	43
3.7 Appendix B: Robustness of SHOT decoupling to different coupling topologies	45
4 Chemical Shift Correlations from Hyperpolarized NMR using a single SHOT	51
Summary	51
4.1 Introduction	52
4.2 Experimental Section	54

4.2.1	Dynamic Nuclear Polarization and NMR Spectroscopy	57
4.3	Results and Discussion	58
4.4	Conclusions	64
4.5	Acknowledgements	65
4.6	Appendix A: Pulse sequences and calibration	66
4.6.1	SHOT Pulse Parameters	66
4.6.2	NMR Pulse Sequences	66
4.7	Appendix B: Figures and Tables	68
5	Diffusion of hyperpolarized ^{13}C-metabolites in tumor cell spheroids using real-time NMR spectroscopy	71
	Summary	71
5.1	Introduction	72
5.2	Methods	73
5.2.1	Hyperpolarized diffusion-weighted NMR spectroscopy	73
5.2.2	Data analysis	74
5.2.3	Calibration and hyperpolarized carbon diffusion	76
5.2.4	Hyperpolarization and NMR measurements	77
5.2.5	MCF-7 tumor cell spheroids	79
5.2.6	Determination of dead cells	79
5.3	Results	80
5.3.1	^{13}C -diffusion coefficients of live and dead tumor cell spheroids	80
5.3.2	^{13}C -diffusion coefficients of tumor cell spheroids following gradual membrane permeabilization	82
5.4	Discussion	87
5.5	Acknowledgements	90
5.6	Appendix A: Supplementary figures	91
5.7	Appendix B: Measurement of ADCs of hyperpolarized ^{13}C -metabolites <i>in vivo</i>	94
5.7.1	Introduction	94
5.7.2	Methods	94
5.7.3	Results and discussion	96
6	Non-invasive lipid measurement in living insects using NMR microscopy	99
	Summary	99
6.1	Introduction	100
6.2	Materials and Methods	101
6.2.1	Animal handling	101
6.2.2	NMR methods	101
6.2.3	Conventional water and lipid measurements	102
6.3	Results and Discussion	102
6.3.1	Anatomy	102
6.3.2	Spectroscopy	104
6.3.3	Relative fat distribution	105
6.3.4	Conclusions	106
6.4	Acknowledgements	106
6.5	Appendix A: Supplementary figures	107

Conclusion	109
Bibliography	111
Curriculum vitae	a
List of publications	c
Acknowledgements	g

1 Introduction

“I remember, in the winter of our first experiments, just seven years ago, looking on snow with new eyes. There the snow lay around my doorstep - great heaps of protons quietly precessing in the earth’s magnetic field. To see the world for a moment as something rich and strange is the private reward of many a discovery. But I am afraid it has little bearing on the sober question we must, as physicists, ask ourselves: What can we learn from all this about the structure of matter?”

— Edward Mills Purcell (* 1912; † 1997)

Since the discovery of nuclear magnetic resonance (NMR) by *Felix Bloch* and *Edward Mills Purcell* in 1945 NMR has gone through a rapid series of developments. NMR spectroscopy has become a standard method for structural analysis of complex molecules and magnetic resonance imaging (MRI) has been established as a valuable non-invasive tool in medical diagnostics¹⁻⁵. Novel contrast mechanisms such as functional MRI (fMRI) have extended MRI’s abilities from solely studying morphology to the mapping of neural activity, allowing unprecedented insights in neurology and brain function⁶. A new frontier in MRI development is the visualization of biological processes on a cellular and molecular level, a field known as ‘Molecular Imaging’. It promises a better diagnosis and clearer characterization of many diseases than possible with conventional techniques, for example for cancer as well as for neurological and cardiovascular diseases⁷.

The main limiting factor in detecting molecular events by MRI is its inherently low sensitivity, resulting from low spin polarization at thermal equilibrium. This limitation can be overcome temporarily by pushing the polarization more than four orders of magnitude beyond thermal equilibrium which is possible by several so-called hyperpolarization techniques⁸. The most prominent technique, dissolution dynamic nuclear polarization⁹ (DNP) has led to a breakthrough in molecular imaging by means of MRI. Detection of biologically relevant ¹³C-labelled substrates in the micromolar concentration range such as [1-¹³C]pyruvate, [1-¹³C]lactate, or [1,4-¹³C]fumarate and their metabolic products has become possible and can give new

insights into biochemical pathways *in vivo*. The evaluation of the clinical potential is currently a major challenge and a clinical trial on imaging the metabolic conversion of ^{13}C -labelled pyruvate to lactate in patients with prostate cancer¹⁰ shows great promise for the future. Nevertheless, novel efficient imaging and spectroscopy sequences need to be developed in this young research field and strategies have to be found in order to extend the lifetime of the hyperpolarized spins as far as possible to tap the full potential of this promising technique^{11–14}.

My research addresses methodical development in this context. It bridges from numerical optimization of radiofrequency (RF) pulses by optimal control theory to novel NMR spectroscopy methods based on hyperpolarization techniques and is structured in the following four chapters.

Tailored real-time scaling of heteronuclear couplings

The interaction of nuclear spins with an RF pulse irradiated from a coil is the basic step of each NMR experiment. The optimization of the pulse shape therefore is of central importance to tailor NMR sequences consisting of multiple pulses to specific applications. The simplest form of an RF pulse is a rectangular pulse with constant amplitude and phase, also denoted as hard pulse. However, such a pulse is very limited for large tip-angles in terms of bandwidth and is not robust to variations of the transmitted field from the coil. These errors can partly be compensated by composite or shaped pulses^{15,16}. Nevertheless, such pulses are not flexible enough to guarantee the optimal pulse shape for each application. A more general strategy for the design of pulses can be achieved if the tailoring of RF pulses is treated as an optimization problem of a fully controllable dynamic system. The group of Prof. Steffen Glaser has achieved to translate and apply elements of optimal control theory to the field of NMR spectroscopy and imaging. The GRAPE (gradient ascent pulse engineering) algorithm is a numerical tool for optimal control of spin systems which has been successfully used for both NMR and MRI, in the field of quantum control and quantum information, as well as in Electron Paramagnetic Resonance (EPR)^{17–30}. A generalized variation of the GRAPE algorithm has been developed for the design of efficient heteronuclear decoupling sequences²³. The goal of decoupling sequences in NMR is to simplify a multiplet to a singlet peak in the spectrum of a coupled spin pair and thereby to increase the signal-to-noise ratio. This approach, which is termed 'GRAPE tracking', allows to optimize decoupling sequences numerically as has successfully been demonstrated for the case of heteronuclear decoupling at low power²³, showing improved performance compared to conventional decoupling sequences^{31,32}.

In **chapter 3** of this work an extension of the GRAPE tracking algorithm is developed. We investigate to which extent the effective J -coupling constant can be manipulated dependent on the offset during a decoupling pulse. Modifying the effective J -coupling at will would for the first time permit to establish a linear correlation between the J -splittings in a 1D spectrum of an observed spin and the heteronuclear chemical shifts from a decoupled spin.

Chemical shift correlations from hyperpolarized NMR using a single SHOT

Hyperpolarization techniques in NMR are inspiring since they allow an increase in the inherently low sensitivity by more than four orders of magnitude. Therefore, they open up new spectroscopic applications in analytical chemistry currently ranging from structural analysis of molecules to the observation of chemical reactions in real-time^{9,33,34}. Ultrafast correlation spectroscopy allows to observe molecular dynamics even by multidimensional NMR in real-time³⁵⁻³⁷. However, current ultrafast correlation methods employ pulsed field gradients and, therefore, are suffering from incomplete refocusing caused by convection and diffusion³⁸. This is especially critical for experiments with hyperpolarized molecules, as they are injected into an NMR sample tube as quickly as possible after the hyperpolarization process to avoid loss of hyperpolarization due to fast T_1 relaxation.

In this work, an efficient, fast, and easy-to-implement method for pseudo-multidimensional spectroscopy of hyperpolarized molecules based on principles of optimal control theory is introduced. It builds on the results of **chapter 3** and does not necessarily employ pulsed field gradients. In collaboration with researchers from *Texas A&M University*, we examined whether this technique can be used in combination with hyperpolarization techniques to obtain chemical shift correlations within a single scan (see **chapter 4**).

Diffusion of hyperpolarized ^{13}C -metabolites in tumor cell spheroids using real-time NMR spectroscopy

Another part of this work deals with the development of NMR pulse sequences to allow an accurate analysis of exchange kinetics and diffusion of hyperpolarized ^{13}C -metabolites in tumor cells (see **chapter 5**). Quantifying and understanding tumor metabolism is key for diagnosis and treatment-response monitoring of tumors. Significant progress in this field has been made since the introduction of dissolution DNP which enabled real-time metabolic imaging⁹. Metabolic activity in tumors, e.g. characterized by pyruvate-to-lactate exchange, has the potential of becoming a clinical tool for monitoring early response-to-treatment, as has been demonstrated in several preclinical *in vivo* studies^{39,40}. However, a careful analysis of the observed ^{13}C label exchange kinetics will require separation of the contributions of pyruvate delivery, membrane transport, and intracellular ^{13}C label exchange with lactate, catalyzed by lactate dehydrogenase (LDH)⁴¹. Several kinetic models have been proposed^{39,42-45} which allow analysis of isotopic label exchange after injection of hyperpolarized $[1-^{13}\text{C}]$ pyruvate. Nevertheless, these models and their respective acquisition schemes cannot separate extra- and intracellular metabolite contributions which would allow to separate the relative contributions from exchange, transport and perfusion to the observed label flux. This problem therefore is a methodological challenge in hyperpolarized ^{13}C spectroscopy. The need for accurate quantitative analysis of the kinetics is of particular importance in the clinical setting, where interpretation of the kinetics will be complicated by a variety of different tumor types and stages. For example, pyruvate-to-lactate label exchange has been shown to decrease in breast but not prostate cancer cells upon treatment, indicating the

complexity of different factors affecting the exchange⁴⁶.

Previous studies have shown that extracellular signals can be attenuated with RF pulses⁴⁷, T_2 weighting⁴⁸, or diffusion weightings⁴⁹ leading to a qualitative confirmation that [1-¹³C]pyruvate is mainly distributed in the extracellular tumor space, while [1-¹³C]lactate is predominantly intracellular. Recently, a new approach based on spin-echo measurements showed that quantitative analysis of hyperpolarized metabolite kinetics might be possible: it was observed in tumors that an increasing echo/FID ratio of hyperpolarized metabolites can be measured after injection of [1-¹³C]lactate. This increase can be explained by longer T_2 relaxation time constants and reduced ADCs by extravasation of the metabolite into the tumor's interstitial space⁵⁰. By comparison to experiments with additional inhibition of the monocarboxylate transporter, it was shown that the increase of echo/FID ratio was partly due to uptake into the cells. However, the problem of quantitatively separating intra- and extracellular compartments has not been solved yet.

Our study investigates, whether it is possible to separate metabolite signals from different compartments via their diffusion characteristics, since the metabolite diffusion coefficients depend on their relative cellular compartments^{51,52}. There is evidence that the intracellular apparent diffusion coefficient (ADC) is lower than the extracellular ADC, because diffusion inside the cell is restricted and hindered⁵³⁻⁵⁵. In this work, metabolite diffusion in breast cancer cells is explored with hyperpolarized ¹³C diffusion-weighted spectroscopy⁵⁶. We emphasize the question, whether ¹³C ADCs of metabolites are sensitive to physiological changes of the cell, which potentially could make them a biomarker for tumor response to treatment.

Recently, other groups have focused on hyperpolarized ¹³C diffusion-weighted spectroscopy as a tool to separate low concentrated molecules of different size by their self-diffusion coefficient and on creating diffusion weighted ¹³C-metabolite images by a STEAM sequence^{57,58}.

Based on the results of **chapter 5** we investigated in cooperation with researchers from the *Danish Technical University of Copenhagen* if quantitative ADC detection of hyperpolarized metabolites *in vivo* is feasible by using slice-selective optimized refocusing pulses (see **chapter 5.7**).

Non-invasive lipid measurement in living insects using NMR microscopy

Quantification of NMR signals in terms of determining the number of molecules present in a sample is usually a challenging task. This is especially important for metabolic studies involving hyperpolarized substrates, where detecting absolute metabolic conversion rates instead of relative dimensionless exchange rate constants is desired. While the quantification issue in hyperpolarized ¹³C *in-vivo*-spectroscopy is an active area of research, we investigate in **chapter 6** how absolute fat and water content can be quantified in living insects by ¹H NMR spectroscopy.

Bark beetles cause huge damage in forests worldwide. However, their epidemic spreading is not very well understood. One key to understanding outbreak patterns is to explain dispersal flight distances which are assumed to be limited by lipid reserves. NMR microscopy offers nondestructive and spatially resolved separation of water and fat signals and is therefore ideally suited for studying lipid consumption during flight⁵⁹. One of the most prominent features of NMR is exploited, namely

separating chemical environments by their different chemical shift. We show that NMR microscopy can be used to quantify and visualize fat and water distribution in small living insects non-invasively which allows to address biological questions that could not be answered so far.

In summary, novel NMR methods are developed in this work based on an innovative RF pulse design by optimal control theory and dissolution DNP for increasing sensitivity. In addition, a method for absolute fat and water quantification in living insects is developed. Major goals are the virtually arbitrary control of heteronuclear couplings by tailored decoupling sequences and the quantitative characterization of tumor metabolism by separation of intra- and extracellular compartments.

2 Theory and Methods

“There is nothing that nuclear spins will not do for you, as long as you treat them as human beings”

— Erwin Louis Hahn (* 1921)

Nuclear magnetic resonance (NMR) is based on the magnetic properties of nuclei in atoms as defined by their nuclear spin angular momentum. Even though the magnetic properties of nuclei have very little effect on the chemical and physical properties of matter, they give rise to an interaction with local magnetic fields created by their molecular environment. The main theme of NMR is to use these intrinsically weak interactions of nuclear spins with their environment to obtain information about microscopic and macroscopic structure. Nuclear spins can be manipulated without destroying or interfering with their environment making them ideal “spy agents” for the experimentalist to obtain molecular information non-destructively. In this chapter, the physical fundamentals and methods of the work described in this thesis are covered briefly. First, two important theoretical concepts for NMR, the spin angular momentum and the density matrix formalism, are introduced (see section 2.1). For detailed explanations the reader is referred to standard NMR textbooks^{3,60–63}

In addition, relevant methodological concepts for the presented work are introduced, including heteronuclear decoupling and optimal control methods for coupled spin systems (see section 2.2 and 2.3), hyperpolarization techniques (see section 2.4), the measurement of diffusion properties using NMR (see section 2.5), and the basics of MRI (see section 2.6).

2.1 Spin angular momentum and the density matrix

In 1922, *Otto Stern* and *Walther Gerlach* studied the deflection of a beam of silver atoms in a highly inhomogeneous magnetic field. Their experiment beautifully demonstrates basics of quantum mechanics, such as quantization, uncertainty, and

the process of measurement. Considering silver atoms in the electronic ground state, the magnetic moment μ of the silver atom is only created by an intrinsic angular momentum of the outer electron which is called spin. In the *Stern-Gerlach experiment*, classical mechanics would predict an isotropic distribution of magnetic moments forming a single pattern of the beam after passing an inhomogeneous magnetic field. However, *Stern* and *Gerlach* observed two discrete distributions and proved quantization of angular momentum for the silver atom.

In 1924, *Wolfgang Pauli* postulated that in addition to electrons, atomic nuclei also possess spin which was shown experimentally in 1926 by *Samuel Goudsmit* and *Ernst Back*, who performed the first measurement of nuclear spin and its *Zeeman effect*. Atoms with an odd number of protons and/or odd number of neutrons possess a nuclear spin angular momentum defined as

$$\mathbf{S} = \frac{h\mathbf{I}}{2\pi} = \hbar\mathbf{I}, \quad (2.1)$$

with h being *Planck's constant* and \mathbf{I} being the spin operator with $\mathbf{I} = (I_x, I_y, I_z)^{64}$. The operator I_z has $2I + 1$ eigenstates denoted $|m\rangle$ for a nuclear spin with quantum number I :

$$I_z |I, m\rangle = m |I, m\rangle. \quad (2.2)$$

The azimuthal quantum number m is quantized:

$$m = -I, -I + 1, -I + 2, \dots, +I. \quad (2.3)$$

The ^1H nucleus, for example, contains one single proton and has spin $I = 1/2$. Spins of other nuclei are formed by combining spins of protons and neutrons according to the quantum mechanical rules of combining angular momenta. They can be divided into three major groups: zero-spin nuclei, spin $1/2$ nuclei, and quadrupolar nuclei. For example, nuclei with both even numbers of protons (e.g. ^{12}C or ^{16}O) and neutrons have a ground state nuclear spin $I = 0$ and display no nuclear Zeeman effect. Therefore magnetic resonance cannot be observed. Nuclei with spin $I = 1/2$ such as ^1H , ^{13}C , ^{15}N , or ^{31}P are of major importance for NMR since such nuclei have convenient magnetic properties. Nuclei with spin $I > 1/2$ are called quadrupolar nuclei, e.g. Sodium-23 has a spin $I = 3/2$. Unlike spin $1/2$ nuclei, these quadrupolar nuclei have electric influences on their nuclear spin angular momentum.

Nuclear spin gives rise to nuclear magnetism. The spin angular momentum and the magnetic moment are proportional:

$$\boldsymbol{\mu} = \gamma\mathbf{S}. \quad (2.4)$$

The proportionality constant γ - denoted as the gyromagnetic ratio - is unique for nuclear species.

In typical NMR experiments we do not want to consider the behavior of a single isolated spin rather than the behavior of the entire spin ensemble containing a large number of single spins. This is achieved by an elegant statistical description of central importance in NMR - the so-called spin density operator formalism.

The spin density operator ρ is defined as the average over all members of the ensemble

described by a wavefunction Ψ :

$$\rho = |\Psi\rangle\langle\Psi|. \quad (2.5)$$

Calculation of an operator expectation value A is defined by its trace:

$$\langle A \rangle = \text{Tr}\{A \rho\}. \quad (2.6)$$

The dynamics of a nuclear spin is described by solving the time-dependent *Schrödinger equation* for the wavefunction $|\Psi\rangle$. However, this seems to be a difficult task at first glance since the Hamiltonian must include all interactions between electrons and nuclei. This equation would be complete but could not be solved in any realistic situation. For the purposes of NMR we can instead consider a simpler equation, in which only the nuclear spin states appear in the wavefunction $|\Psi_{\text{spin}}\rangle$:

$$\frac{d}{dt} |\Psi_{\text{spin}}(t)\rangle \cong -i\mathcal{H} |\Psi_{\text{spin}}(t)\rangle. \quad (2.7)$$

In this approximation known as spin Hamiltonian hypothesis it is assumed that magnetic and electric influences of the electrons are blurred out so that only their average is seen. It derives from the separation of time-scales for nuclear and electronic motions⁶². The spin Hamiltonian consists of external and internal spin interactions:

$$\mathcal{H} = \mathcal{H}_{\text{ext}} + \mathcal{H}_{\text{int}} = \underbrace{\mathcal{H}_{\text{Z}} + \mathcal{H}_{\text{RF}}}_{\mathcal{H}_{\text{ext}}} + \underbrace{\mathcal{H}_{\text{DD}} + \mathcal{H}_{\text{CS}} + \mathcal{H}_{\text{J}} + \mathcal{H}_{\text{Q}}}_{\mathcal{H}_{\text{int}}}. \quad (2.8)$$

The external spin interactions include the *Zeeman interaction* with an external magnetic field (\mathcal{H}_{Z}) as well as the interaction with a radiofrequency (RF) field (\mathcal{H}_{RF}). Internal spin interactions consist of direct dipole-dipole coupling of nuclear spins with each other (\mathcal{H}_{DD}), the chemical shift interaction caused by induced magnetic fields of electrons (\mathcal{H}_{CS}), the indirect spin-spin coupling via electrons (\mathcal{H}_{J}) and the quadrupolar coupling due to electric field gradients (\mathcal{H}_{Q}).

From the time dependent *Schrödinger equation* for a single spin we can derive the *Liouville-von-Neumann equation* for an ensemble of spins

$$\frac{d}{dt}\rho = -i[\mathcal{H}, \rho]. \quad (2.9)$$

The solution of the *Liouville-von-Neumann equation* yields the time evolution of the nuclear spin system. For a time-independent Hamiltonian we have

$$\rho(t) = U(t)\rho(0)U^\dagger(t) = e^{-i\mathcal{H}t}\rho(0)e^{i\mathcal{H}t}, \quad (2.10)$$

with $U = e^{-i\mathcal{H}t}$ being a unitary propagator applying a unitary transformation to the spin state.

2.2 Heteronuclear spin decoupling

Heteronuclear decoupling is mostly used in NMR to remove the peak splittings arising from the effects of heteronuclear scalar coupling thereby simplifying spectra and increasing the SNR. The general principle underlying all decoupling techniques is that selective inversion on one spin leads to refocusing of the scalar coupling evolution on the other observed spin. If these selective inversion pulses are applied synchronously between acquisition points of a free induction decay (FID), the scalar coupling evolution can be effectively inhibited. Since typical heteronuclear scalar coupling constants are in the range of ${}^1J_{CH} = 120 - 170$ Hz, the coupling evolution is much slower than the data acquisition sampling rate, such that the inversion pulses can be stretched out over multiple dwell-times without losing performance. In the limit of continuous RF irradiation the sequence is referred to as continuous wave (CW) decoupling.

We consider a spin 1/2 pair of spin I and spin S , where we continuously irradiate spin S near resonance at offset ν with an RF amplitude u . The relevant rotating frame Hamiltonian is

$$\mathcal{H} = 2\pi\nu S_z + 2\pi J S_z I_z + 2\pi u S_x. \quad (2.11)$$

Transformation to a tilted frame along the effective field of spin S is achieved by a rotation around S_y with an angle Θ defined by

$$\cos(\Theta) = \frac{\nu}{\sqrt{u^2 + \nu^2}} = \frac{\nu}{\nu_{\text{eff}}} \quad (2.12)$$

which leads to the Hamiltonian⁶⁵

$$\mathcal{H} = 2\pi\nu_{\text{eff}} S_z + 2\pi J I_z (S_z \cos(\Theta) + S_x \sin(\Theta)). \quad (2.13)$$

We now switch to a rotating frame along the effective field defined by $2\pi\nu_{\text{eff}} S_z$ and calculate the average Hamiltonian of the $I - S$ coupling term given by the first term of the *Magnus Expansion*⁶⁵⁻⁶⁷:

$$\overline{\mathcal{H}}_{IS}^{(0)} = 2\pi J I_z S_z \cos(\Theta). \quad (2.14)$$

This leads to an effective scaling of the J -coupling constant J_{eff} by the factor $\cos(\Theta)$:

$$J_{\text{eff}} = J \cos(\Theta) = J \frac{\nu}{\sqrt{u^2 + \nu^2}}. \quad (2.15)$$

We note that for small offsets $\nu \ll u$ the J -splitting depends linearly on ν . In Fig. 2.1 the effects of off-resonance CW irradiation at three different RF amplitudes $u = [1000 \text{ Hz}, 5000 \text{ Hz}, 10000 \text{ Hz}]$ are depicted for an I - S -coupled spin system with $J_{IS} = 160$ Hz over a bandwidth of 15 kHz centered at resonance. As can be seen from the simulations in Fig. 2.1, decoupling by CW irradiation becomes rapidly ineffective as the irradiation offset is shifted from resonance. Increasing the effective decoupling bandwidth without the need for excessive power dissipation can be achieved by

iterative schemes relying on supercycles of robust composite 180° pulses such as for example MLEV which consists of a supercycle of the element $90_x^\circ 180_y^\circ 90_x^\circ$ or WALTZ $90_x^\circ 180_{-x}^\circ 270_x^\circ$ ^{15,16,32,68,69}.

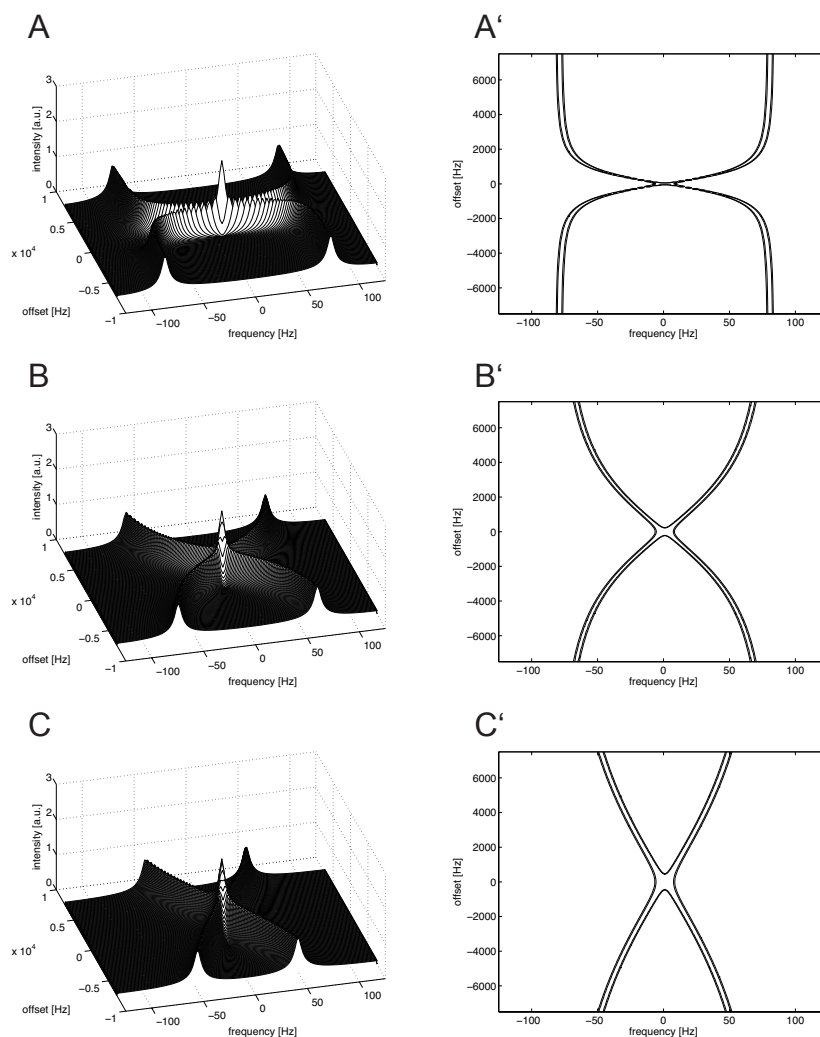


Figure 2.1: Simulated multiplet splitting of spin I for CW decoupling (with constant RF amplitude $u_A = 1000$ Hz (A, A'), $u_B = 5000$ Hz (B, B'), $u_C = 10000$ Hz (C, C')) of spin S as a function of frequency offset ν (A,B,C: stacked plots; A',B',C': contour plots with contour levels at 0.4, 0.45 of the decoupled peak amplitude). Note that for small frequency offsets, the effective J -coupling constant depends linearly on the frequency offset. At increasing RF amplitude u , the bandwidth of the linear range can be expanded at the cost of a decreased slope of the linear relationship.

2.3 Optimal control of coupled spin dynamics

The evolution of a spin system during an NMR experiment is described by the *Liouville-von-Neumann* equation of motion (equation 2.16) and can be actively steered through the control of system independent irradiation of RF pulses created by a radiofrequency coil in proximity to the spins. The optimization of pulse sequences under certain quality criteria based on methods of control theory can be achieved through algorithms which numerically optimize the external controls, namely the RF pulses. This approach has for example been applied for frequency selective pulses⁷⁰ and robust inversion pulses²². The GRAPE algorithm (Gradient ascent pulse engineering) which has been developed in the group of *Prof. Steffen Glaser* allows to optimize NMR pulse sequences very efficiently even in very large parameter spaces¹⁷. It has been successfully used for the design of broadband and robust excitation, inversion, and refocussing pulses in uncoupled spin systems^{18,20,21,26,29}. Furthermore, it has been demonstrated that in heteronuclear coherence transfer experiments, the numerically optimized pulses achieved the analytically derived maximal transfer efficiency in terms of time-optimal and relaxation-optimal pulses⁷¹. The GRAPE approach only requires two full time evolutions to calculate the gradient for the optimization of the control amplitudes and therefore outperforms conventionally used difference methods. Since the algorithm is based on gradient ascent, there is no guarantee that it will converge to the global optimum. However, different starting conditions and iterated optimization procedures can help in finding local optima that are close to the desired quality.

A generalized variation of the GRAPE algorithm has been developed for the design of efficient low-power heteronuclear decoupling sequences²³. Instead of optimizing the evolution of the spin system from an initial state to a target state, this approach tracks the evolution of the magnetization over a number of acquisition points throughout the whole pulse sequence. The so-called GRAPE tracking approach is especially suited for optimizing heteronuclear decoupling sequences with the goal of inhibiting the coupling evolution throughout the free induction decay (FID) acquisition by irradiation on one spin, while the other spin is observed. In contrast to conventional approaches based on average Hamiltonian theory which are based on periodic patterns of inversion pulses, optimal tracking can steer the coupled spin system to a desired trajectory as closely as possible without imposing a periodicity on the RF control amplitudes. In addition, constraints on the optimization, such as power reduction, or robustness with regard to B_1 miscalibration can be taken into account.

Low power irradiation during decoupling is especially beneficial for applications in biomedical imaging in human patients⁷². In contrary to conventional decoupling sequences (WALTZ-16, MLEV-16)^{31,32}, it has been shown both in simulations and experiments that optimal tracking can lead to large improvements with regard to the decoupling efficiency and the robustness²³.

Besides in NMR spectroscopy, optimized decoupling sequences can also be applied in research areas such as quantum information processing or quantum control to achieve longer coherence times of the spins^{73,74}.

2.3.1 Outline of the GRAPE and the GRAPE tracking algorithm

The GRAPE algorithm¹⁷ is concerned with the problem of steering a spin system characterized by the density operator ρ to a target operator C . It can also be extended to track the density operator to a set of N target states C_N (GRAPE tracking)²³. We consider a time evolution of the form

$$\frac{d}{dt}\rho(t) = -i [(\mathcal{H}_0 + u_x(t)S_x + u_y(t)S_y), \rho(t)], \quad (2.16)$$

with \mathcal{H}_0 being the free evolution Hamiltonian and $S_{x,y}$ representing the RF control fields S_x and S_y with the available control amplitudes u_x and u_y that are changed during the optimization.

The goal of the optimization is to find control amplitudes that steer the spin system such that the evolution of the density operator has maximum overlap with the target operator(s) C_k at all acquisition time points T_k , for $k = [1, \dots, N]$. We define the number of digitization in between two acquisition points as M . For Hermitian operators this maximum overlap can be measured by the standard inner product and we define the quality factor Φ_k for each acquisition point

$$\Phi_k = \langle C | \rho(T) \rangle \quad (2.17)$$

which can also be expressed as the inner product of the backpropagated target state λ_j at a time $j = j\Delta t$ and the forward propagated initial state ρ_0 :¹⁷

$$\Phi_k = \langle U_{j+1}^\dagger \cdots U_k^\dagger C U_k \cdots U_{j+1} | U_j \cdots U_1 \rho_0 U_1^\dagger \cdots U_j^\dagger \rangle. \quad (2.18)$$

As a good approximation for the gradient we obtain:¹⁷

$$\frac{\partial \Phi_0}{\partial u_{x,y}(j)} = - \langle \lambda_j | i\Delta t [S_{x,y}, \rho_j] \rangle. \quad (2.19)$$

The gradient allows to update the control amplitudes u_x and u_y for optimization of the quality factors and therefore gives us the basis for the GRAPE and GRAPE tracking algorithms (see Figs. 2.2 and 2.3 for a depiction of the algorithms). An efficient way of calculating the gradient for all acquisition points at once has been found such that the GRAPE tracking algorithm still manages on a single backwards and forwards propagation of the spin system²³. The algorithm can be summarized as follows:

1. Guess initial controls $u_x(j)$ and $u_y(j)$ for all timesteps $1 \leq j \leq NM$
2. Starting from the initial state ρ_0 calculate $\rho(t)$ for all time points by forward propagation
3. Starting from the final states ρ_N calculate $\rho(t)$ for all time points by backward propagation
4. Calculate the gradients $\frac{\partial \Phi_0}{\partial u_{x,y}(j)}$ for all time points

5. Repeat steps 2.-4. in loop structure for all B_1 scaling factors and offsets and calculate the average gradients
6. Update the $2NM$ control amplitudes $u_x(t_j)$ and $u_y(t_j)$
7. With the new controls go to step 2

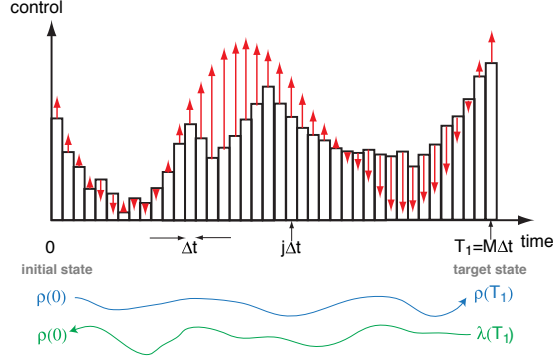


Figure 2.2: Schematic representation of a control amplitude consisting of M steps of duration $\Delta t = T_1/M$ during an update step of the GRAPE algorithm for steering a spin system from the initial state $\rho(0)$ to the desired target state $\lambda(T_1)$. The gradient steps for the update of the control amplitudes are depicted as red arrows indicating how the controls should be changed in the next update step for an improved performance function.

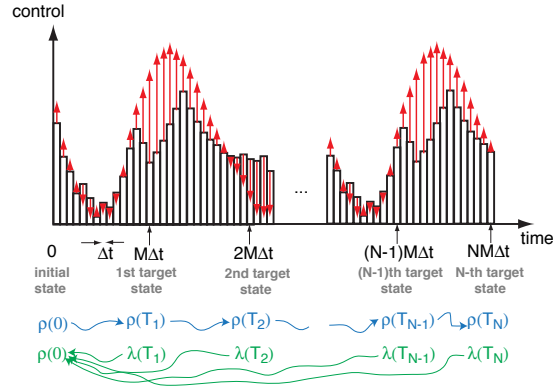


Figure 2.3: Schematic representation of a control amplitude consisting of NM steps of duration $\Delta t = T_N/(NM)$ during an update step of the GRAPE tracking algorithm for steering a spin system from the initial state $\rho(0)$ to a set of desired target states $\lambda(T_k)$, with $k = [1, \dots, N]$. The gradient steps for the update of the control amplitudes are depicted as red arrows indicating how the controls should be changed in the next update step for an improved performance function.

2.4 Hyperpolarization

If an ensemble of spin $1/2$ particles is exposed to an external field B_0 , one observes an energy separation because of the Zeeman interaction. The spin population tends to have a slight excess in the lower energy state, which can be either parallel ($m = +1/2$) or antiparallel ($m = -1/2$) to the magnetic field depending on the sign of γ . Two populations of spins are created, from which we denote the antiparallel one as N_\downarrow and the parallel one as N_\uparrow . A state, in which one population is larger than the other one indicates a net polarization of the spins. The energy difference of the two Zeeman states ($\Delta E = \gamma\hbar B_0$) is typically very small compared to the thermal energy ($k_B T$) and the ratio of the two populations is determined by the Boltzmann distribution:

$$\frac{N_\downarrow}{N_\uparrow} = e^{-\Delta E/kT}. \quad (2.20)$$

The excess of spins in the lower energy state creates an effective net magnetization that is characterized by the polarisation P :

$$P = \frac{N_\uparrow - N_\downarrow}{N_\uparrow + N_\downarrow}. \quad (2.21)$$

At thermal equilibrium, temperature T , and external field B_0 , we get:

$$P = \tanh\left(\frac{\gamma\hbar B_0}{2kT}\right). \quad (2.22)$$

For protons in an external field at $7 T$, the polarization is $P \approx 2.4 \times 10^{-5}$ at room temperature, leading to an excess of about 24 spins in the parallel state out of a million total spins. The magnitude of the observable net magnetic moment \mathbf{M} is directly proportional to P and the number of spins N_S in the sample⁷⁵:

$$M = \frac{1}{2}N_S\gamma\hbar P. \quad (2.23)$$

This low net spin polarization even at high magnetic fields is the reason of the inherent low sensitivity in both NMR and MRI. Several techniques have been developed to overcome the low net spin polarization imposed by the Boltzmann distribution at thermal equilibrium. A non-thermal nuclear polarization state with much higher polarization can be achieved. This process is known as hyperpolarization. Several methods can be used to create a hyperpolarized spin state for different nuclear isotopes:

- "Brute force" methods exploiting low temperatures and high B_0 field^{76,77}
- Spin exchange optical pumping (SEOP), primarily applied to ^{129}Xe . Applications include the observation of lung ventilation and molecular imaging at ultralow concentrations using the HYPER-CEST detection method for xenon

in functionalizable molecular cages^{8,78–85}

- Dissolution dynamic nuclear polarization (DNP), where electron polarization can be transferred to e.g. ^{13}C nuclear spins in biologically relevant molecules at room temperature^{9,86–88}
- Parahydrogen induced polarization (PHIP) uses a chemical reaction to transfer high para-state spin order of hydrogen to bonded atoms through J -coupling^{89–91}

From the above described techniques for hyperpolarization of nuclear spins, dynamic nuclear polarization (DNP) is most commonly used and the work described here relies on this technique. It is based on the fact that nuclear spin polarization can be increased by selectively exciting electron transitions from electrons which are coupled to the nuclei via the hyperfine interaction through microwave irradiation. This effect was predicted by *Albert Overhauser* for metals⁹² and has been described by *Abragam* and *Procter* for electrons in liquids later - a phenomenon they named 'solid effect'⁹³. The experimental demonstration of this effect has been shown by *Carver* and *Slichter*⁹⁴ in 1953. The combination of nuclear spin-state-selective excitation and a fast relaxation process of the electronic spin state to the ground state ($T_{1,e} \approx 1$ ms) increases the population of the nuclear spin ground state, thereby continuously increasing the polarization of the nuclear spins until it reaches the level of the electrons. This leads to a major increase in polarization, since at low temperatures below 4 K the electron spin polarization becomes $> 95\%$ which is almost two orders of magnitude larger than the corresponding nuclear spin polarization. This effect is caused by the large gyromagnetic ratio of the electrons as compared to nuclei.

DNP theory has been further extended to involve many electrons and thermal mixing. However, so far no quantitative general theoretical description of DNP has been found^{95,96}.

To ensure that the sample to be hyperpolarized contains enough unpaired electrons, a stable chemical radical is usually added to the sample in the liquid state or the solid state sample is exposed to ionizing radiation. It has taken 60 years after the original discovery of DNP by *Albert Overhauser* until its potential has been made available to the liquid state NMR and MRI community by *Jan Henrik Ardenkjær-Larsen*, *Klaes Golman*, and coworkers who solved the technically very challenging problem of bringing the polarized solid material into the liquid state without polarization loss⁹.

Dissolution DNP allows to increase the inherent low sensitivity of ^{13}C nuclei by a factor of $\approx 50\,000$. This technique opened up a new field of research in NMR and MRI development allowing dynamic *in vivo* and *in vitro* studies of low concentrated ^{13}C substrates in the mM range and their downstream metabolites such as e.g. $[1-^{13}\text{C}]\text{pyruvate}$, $[1-^{13}\text{C}]\text{lactate}$, $[1-^{13}\text{C}]\text{alanine}$, or $[1,4-^{13}\text{C}]\text{fumarate}$. The ability to characterize, visualize and quantify metabolic processes in real-time non-invasively leads the way to investigate several important diseases like tumors and their response to treatment, heart failure, or kidney malfunction^{39,97–105}.

A typical sample for DNP experiments conducted for the work presented in this thesis contains 14 M $[1-^{13}\text{C}]\text{pyruvic acid}$, 15 mM OX063 trityl radical and 10 mM

Dotarem relaxation contrast agent. The sample is loaded into an HyperSense DNP polarizer operating at magnetic field ~ 3.35 T, temperature ~ 1.4 K, microwave frequency ~ 94.1 GHz and microwave power ~ 100 mW. When at 1.4 K the sample is then polarized for ~ 40 min. The polarized sample is rapidly dissolved with a buffered dissolution agent in D_2O (temperature $\sim 185^\circ C$, pressure ~ 10 bar). The final solution contains ~ 10 mM hyperpolarized $[1-^{13}C]$ pyruvate at $37^\circ C$ with pH ~ 7.4 and a liquid-state polarization of $\sim 25\%$, which is monitored in a low field permanent magnet spectrometer operating at 0.94 T.

In our case, the hyperpolarized sample had to be transported from the polarizer to a different building on campus Garching, where a high-field spectrometer at 14.1 T field strength equipped with strong gradients is located (see Fig. 2.4). Therefore, magnetization losses due to T_1 had to be minimized to maintain hyperpolarization. T_1 was increased from ~ 68 s (dissolution in H_2O , $35^\circ C$) to ~ 165 s (dissolution in D_2O , $45^\circ C$) at 0.94 T field strength, due to decreased dipolar relaxation from both deuterated solvent and increased temperature⁸⁸. After dissolution, the sample was attached to a preheated ($45^\circ C$) 0.5 T permanent magnet while being transported 0.5 km distance by bicycle^A within 100 s.

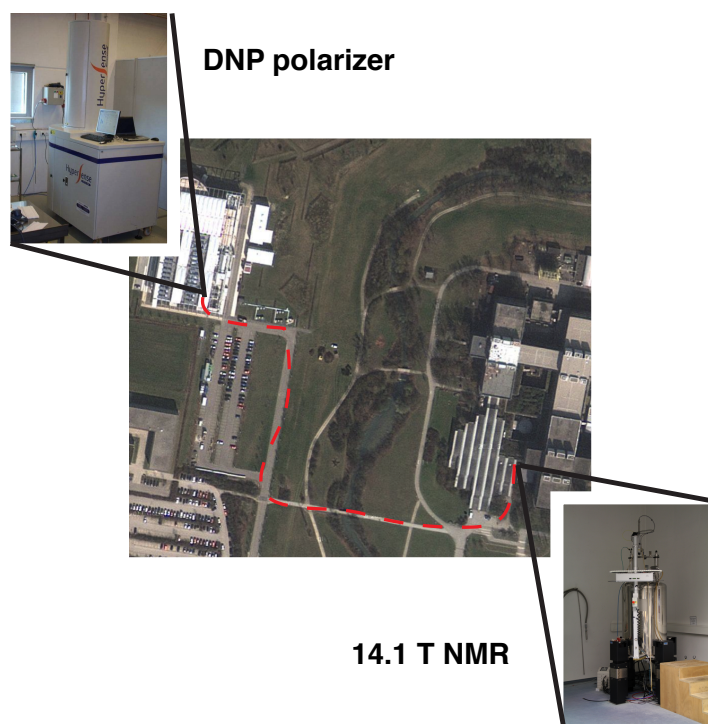


Figure 2.4: Way of transport (dashed red line) of a hyperpolarized sample from General Electrics Global Research in Garching to the Department of Chemistry at Technische Universität München nearby (Map data: Google, DigitalGlobe, GeoBasis-DE/BKG, GeoContent, GeoEye).

^AAwarded video footage can be found at <http://www.ismrm.org/12/Movies/Hyperwars/>

2.5 Measurement of diffusion properties by NMR

First observed by *Robert Brown* in 1827 for pollen grain under a microscope and later theoretically explained by *Albert Einstein*, diffusion is a random translational motion of molecules driven by internal thermal energy¹⁰⁶. The basic properties of diffusion are well described by *Fick's first and second law*. The latter describes the time evolution of a probability distribution $P(\mathbf{r}_0, \mathbf{r}, t)$ which gives the probability of a movement of a particle from position \mathbf{r}_0 to \mathbf{r} :

$$\frac{\partial P(\mathbf{r}_0, \mathbf{r}, t)}{\partial t} = D\nabla^2 P(\mathbf{r}_0, \mathbf{r}, t), \quad (2.24)$$

where D denotes the self-diffusion coefficient given in units of $\mu\text{m}^2/\text{ms}$. Given the starting condition $P(\mathbf{r}_0, \mathbf{r}, t) = \delta(\mathbf{r} - \mathbf{r}_0)$, the solution to *Fick's second law* yields a Gaussian distribution¹⁰⁷:

$$P(\mathbf{r}_0, \mathbf{r}, t) = (4\pi D)^{-3/2} e^{-\frac{(\mathbf{r}-\mathbf{r}_0)^2}{4Dt}}. \quad (2.25)$$

Equation 2.25 quantifies how particles diffuse over time through a random process. The mean displacement $\langle(\mathbf{r} - \mathbf{r}_0)\rangle$ is zero due to the random nature of diffusion. The diffusion constant D of an isotropic medium or a solute in an isotropic medium is affected by several external parameters like temperature T , viscosity η , and the size of the molecule under investigation described by its hydrodynamic radius R_H . The underlying relation is given by the *Stokes-Einstein equation*¹⁰⁸:

$$D = \frac{kT}{6\pi\eta R_H}. \quad (2.26)$$

When observing molecular diffusion under *in vivo* conditions, diffusion can be anisotropic because of diffusion barriers such as fiber structures or cell membranes. Hence, for an accurate description, the scalar diffusion coefficient is replaced by a second rank 3×3 diffusion tensor \mathbf{D} .

In addition, diffusion barriers such as a cell membrane can restrict the diffusion space to a certain compartment, thereby decreasing the mean squared displacement of the diffusing molecules. Therefore, instead of the self-diffusion coefficient D , a reduced diffusivity described by an apparent diffusion coefficient (ADC) is observed. Since its early days NMR was known to accurately measure the self-diffusion coefficient of liquids as *Erwin Hahn* discovered during his famous experiments on spin echoes and constant background gradients¹⁰⁹. With the development of the pulsed-gradient spin-echo (PGSE) method by *Stejskal* and *Tanner*, diffusion measurements by NMR became robust and reliable making it a routine technique for measurements of diffusion properties¹¹⁰.

The basic principle of diffusion measurements in NMR relies on the application of two additional bipolar gradients (alternatively two gradients of the same sign, when applied before and after a 180° pulse - Fig. 2.6). The gradients label spins depending on their spatial position and make the overall signal susceptible to incoherent motion of spins, hence diffusion. Diffusion of nuclear spins between the gradients leads to a

loss of phase coherence of the spins when forming the spin echo and therefore to a diffusion-dependent signal loss. This principle is illustrated in Fig. 2.5 which shows the behavior of non-diffusing spins undergoing a pulsed gradient spin echo sequence as compared to Fig. 2.6 which describes the experiment with diffusing spins between time points t_3 and t_5 .

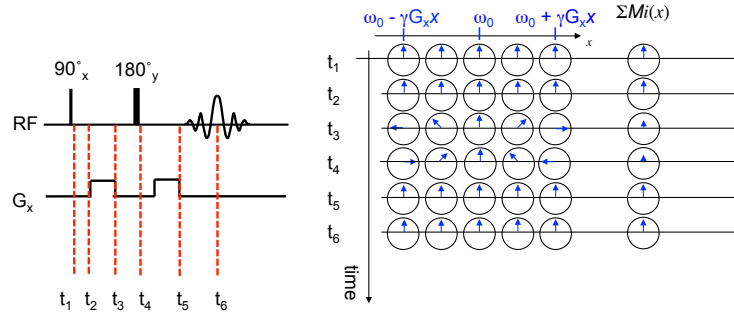


Figure 2.5: Illustration of non-diffusing spins undergoing a PGSE sequence. The spin echo sequence is illustrated for five representative spin ensembles along the x -gradient direction at six consecutive points during the sequence (t_1 - t_6). Blue arrows depict the respective magnetization and phase of the spin ensembles in the rotating reference frame. In addition, the resulting total magnetization vector is depicted in the outermost column on the right. T_2 relaxation is disregarded in this case. As one can comprehend, at the end of the sequence the signal of non-diffusing spins is completely refocused.

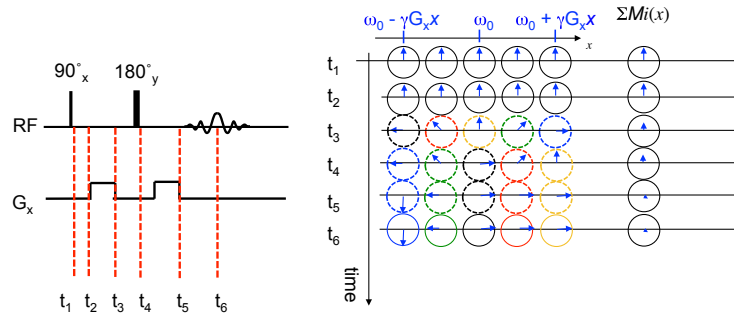


Figure 2.6: Illustration of spins diffusing between t_3 and t_5 and at the same time undergoing a PGSE sequence as in Fig. 2.5. Diffusion of the spins is indicated by dashed lines of the spin ensemble representations. At t_3 , the initial spatial positions of the spins is given and each ensemble is labeled with a certain color. Both at t_4 and t_5 , the final spatial positions of the spins are depicted. As one can comprehend, at the end of the sequence the signal of diffusing spins is not completely refocused, since the spins changed their spatial position between time points t_3 and t_5 randomly. This leads to loss of phase coherence when the spin echo forms as compared to Fig. 2.5.

2.6 Magnetic Resonance Imaging

Magnetic resonance imaging (MRI) adds spatial dimensions to a classical 1D-NMR experiment and allows for spatially resolved NMR signals. Due to its soft tissue contrast and noninvasiveness, MRI has become a standard method in medical diagnostics. The basic principle of MRI is that the *Larmor frequency* can be made a function of space by the application of linear magnetic field gradients in three orthogonal directions. This idea was published by *Sir Peter Mansfield*⁴ and *Paul C. Lauterbur*⁵ in 1973. They received the Nobel Prize in Physiology or Medicine for this concept in 2002. The relationship between the *Larmor frequency* of spins and their spatial coordinates in the presence of a magnetic gradient is the basic equation of the imaging principle:

$$\omega(\mathbf{r}) = \gamma B_0 + \gamma \mathbf{G} \cdot \mathbf{r}. \quad (2.27)$$

It is worth noting that the *Larmor frequency* ω is effectively only modified by additional gradient field components parallel to B_0 since the gradient fields are several orders of magnitude smaller than B_0 ($\gamma G \ll B_0$). Horizontal gradient fields just slightly tilt the net field direction but do not effect the Larmor frequency in standard applications.

Considering nuclear spins within an external gradient field \mathbf{G} at spatial position \mathbf{r} with a sample volume dV and local spin density $\rho(\mathbf{r})$, the NMR signal dS from the spins can be expressed by⁶³:

$$dS(\mathbf{G}, t) \sim \rho(\mathbf{r})dV \exp(i\omega(\mathbf{r})t). \quad (2.28)$$

This approximation neglects any relaxation effects. It holds for strong gradients ensuring that the phase spread $\gamma \mathbf{G} \cdot \mathbf{r}$ is much more rapid than the relaxation decay. Taking the spatial dependence of the *Larmor frequency* by external field gradients into account Eqn. 2.28 can be written as:

$$dS(\mathbf{G}, t) \sim \rho(\mathbf{r})dV \exp(i[\gamma B_0 + \gamma \mathbf{G} \cdot \mathbf{r}]t). \quad (2.29)$$

In the case of the reference frequency of the receiver being set to the *Lamor frequency* ω_0 , the integrated signal becomes:

$$S(t) = \iiint \rho(\mathbf{r}) \exp(i\gamma \mathbf{G} \cdot \mathbf{r}t) d\mathbf{r}. \quad (2.30)$$

This signal equation has the form of a Fourier transformation which becomes more clear, when the concept of the reciprocal space vector, denoted as \mathbf{k} , is introduced. \mathbf{k} is the conjugate variable of the real space vector \mathbf{r} :

$$\mathbf{k} = \frac{\gamma \mathbf{G}t}{2\pi}. \quad (2.31)$$

Therefore we get a Fourier relationship between the signal intensity $S(\mathbf{k})$ and the spin density $\rho(\mathbf{r})$:

$$S(\mathbf{k}) = \iiint \rho(\mathbf{r}) \exp(i2\pi\mathbf{k}\mathbf{r}) d\mathbf{r} \quad (2.32)$$

$$\rho(\mathbf{r}) = \iiint S(\mathbf{k}) \exp(-i2\pi\mathbf{k}\mathbf{r}) d\mathbf{k}. \quad (2.33)$$

The first step to get a spin density image in real space is the mapping of the inverse space, also denoted as k -space. Moving through k -space can happen either by varying the time t after a gradient was turned on or the gradient amplitude G . The gradient direction determines the direction of the mapping in k -space. After the mapping, a Fourier transformation obtains the image in real space. This principle is shown in fig. 2.7 for a linear gradient in x -direction, which spatially encodes the spin distribution in x -direction during the acquisition of an FID. Because the spins are encoded by different *Larmor frequencies*, this principle is also known as frequency encoding.

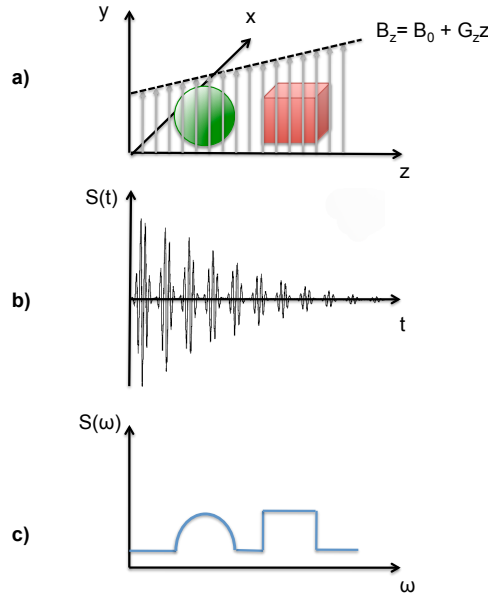


Figure 2.7: Frequency encoding. a) Spherical and cubical sample containing protons; a linear gradient G_z is applied in z -direction which locally varies the strength of the B_z field and causes the spins at different z -positions to precess at different *Larmor frequencies* during FID acquisition. b) Time domain signal $S(t)$ in the receiver coil. c) Fourier transformation of b) shows the frequency encoding of the spin distribution projected along the z -axis.

An external magnetic field B_1 from an RF coil tuned to the *Larmor frequency* can tip the magnetization vector of the spins to the transverse plane with their precession being detectable. If an additional gradient perpendicular to the frequency encoding gradient is applied, the B_1 pulse is merely exciting spins matching its frequency bandwidth. This procedure is called selective excitation in contrary to non-selective excitation without an additional gradient. Slice selection is primarily used to image

single slices within the object under investigation. For selectively exciting a slice of thickness Δx , a pulse bandwidth of $\gamma G_x \Delta x$ is required. The pulse frequency bandwidth is inversely proportional to the pulse duration. To achieve a slice selection with a nearly rectangular frequency excitation profile, the B_1 pulse form of choice is a sinc-function since the Fourier transform of a sinc-function is close to a rectangle function.

After a selective excitation of a slab of spins (e.g. in the z -direction), the x - y reconstruction of an image is achieved by a two-dimensional Fourier transform. Fourier imaging, developed by *Kumar, Welte* and *Ernst*¹¹¹, encodes phase and amplitude information which forms the basis of two-dimensional-spectroscopy methods.

Frequency encoding of the FID signal can provide one dimension in k -space, which we will now denote as the x -direction for convenience. The gradient G_x , which is present for a readout period t_{ro} during the sampling of the FID, is called readout gradient. The spacing between successively mapped k_x points is determined by a combination of the so-called dwell-time t_d , which is the time-difference between two acquired data points of the FID, and the strength of the readout gradient. The magnitude of k_x for a specific point in k -space is determined by the index number n ranging from $-N/2$ to $N/2$ and N being the maximum number of points sampled in one direction in k -space:

$$k_x = \frac{\gamma G_x (nt_d)}{2\pi}. \quad (2.34)$$

Further dimensions in k -space can be mapped by phase encoding. By applying another gradient G_y in y -direction for a fixed time before the sampling of the FID begins, a phase modulation is imposed on the spins along the y -axis. Usually the gradient is turned on for a fixed time t_{ph} so that the phase shift due to the gradient becomes:

$$\Delta\Phi = \gamma t_{ph} \Delta G_y y. \quad (2.35)$$

The mapping of k -space in k_y direction is accomplished by varying the gradient strength G_y :

$$k_y = \frac{\gamma (nG_y) t_{ph}}{2\pi}. \quad (2.36)$$

With this combination of frequency and phase encoding, each FID during a given phase encoding step provides one line in k -space. By varying the gradient strength G_y we build up a 2D Cartesian grid in k -space. Once the whole k -space is mapped, a two-dimensional Fourier transform reconstructs $\rho(\mathbf{r})$. Fig. 2.8 illustrates a standard 2D-imaging sequence and the principle of k -space sampling.

The area that is mapped in real space is called the Field of View (FOV) and is determined by the inverse of the sampling rates along k_x and k_y :

$$FOV_x = \frac{1}{\Delta_{k_x}} = \frac{2\pi}{\gamma G_x t_d} \quad (2.37)$$

$$FOV_y = \frac{1}{\Delta_{k_y}} = \frac{2\pi}{\gamma \Delta G_y t_{ph}}. \quad (2.38)$$

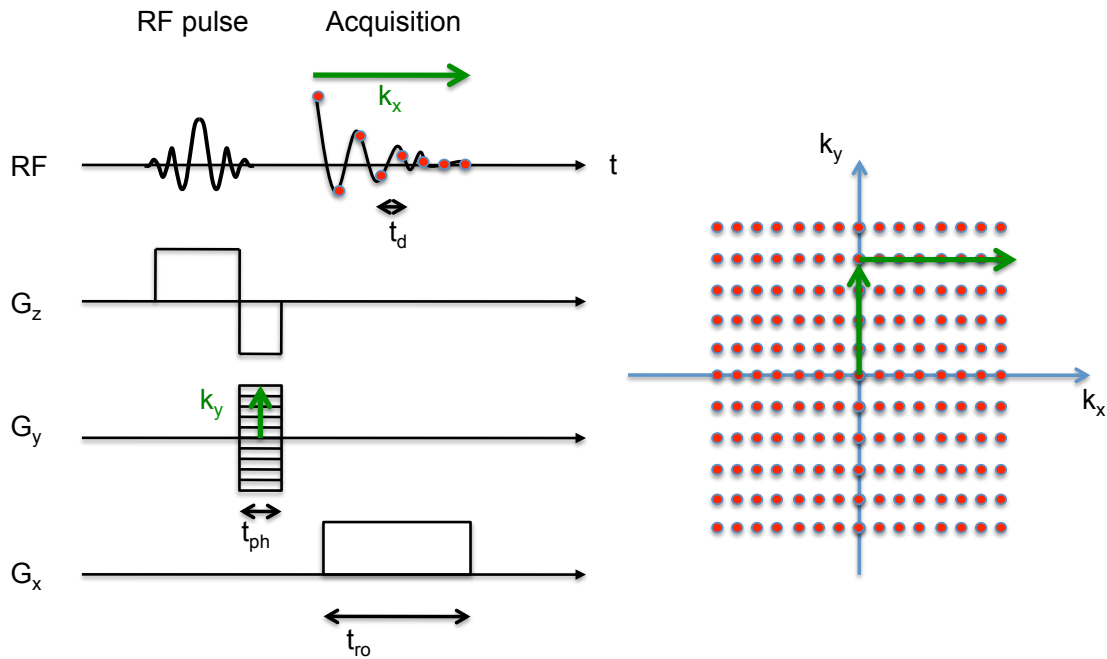


Figure 2.8: Basic 2D-imaging sequence with slice selection. The left diagram depicts the pulse sequence timing, while the right drawing shows the sampling of k -space. First a sinc-shaped RF pulse is applied while the slice select gradient G_z is turned on to selectively excite a slice in the x - y plane. After the slice selection gradient is turned off, a reversed compensation gradient is turned on to rephase the spins. At the same time a phase encoding gradient with a specific gradient strength G_y is turned on for a fixed time t_{ph} . After a short delay, the signal is acquired with a sampling rate $1/t_d$ with t_d being the dwell time. During the readout a gradient of constant strength G_x and fixed readout time t_{ro} is turned on. The sampling rate of k_x and k_y determines the FOV of the image in real space.

3 Tailored real-time scaling of heteronuclear couplings

“One has to have the imagination to think of something that has never been seen before, never been heard of before. At the same time the thoughts are restricted...the problem of creating something which is new, but which is consistent with everything which has been seen before, is one of extreme difficulty.”

— Richard Feynman (* 1918; † 1988)

Reprinted from *Journal of Magnetic Resonance*, volume 223, pp. 207-218 (2012); Franz Schilling and Steffen J. Glaser; **Tailored real-time scaling of heteronuclear couplings**. With permissions from Elsevier Inc. Modifications: replacement of Abstract by Summary, addition of Appendix B.

Summary

Heteronuclear couplings are a valuable source of molecular information, which is measured from the multiplet splittings of an NMR spectrum. Radiofrequency irradiation on one coupled nuclear spin allows to modify the effective coupling constant, scaling down the multiplet splittings in the spectrum observed at the resonance frequency of the other nuclear spin. Such decoupling sequences are often used to collapse a multiplet into a singlet and can therefore simplify NMR spectra significantly. Continuous-wave (CW) decoupling has an intrinsic non-linear offset dependence of the scaling of the effective J -coupling constant. Using optimal control pulse optimization, we show that virtually arbitrary off-resonance scaling of the J -coupling constant can be achieved. The new class of tailored decoupling pulses is named SHOT (Scaling of Heteronuclear couplings by Optimal Tracking). Complementing CW irradiation, SHOT pulses offer an alternative approach of encoding chemical shift information indirectly through off-resonance decoupling, which however makes

it possible for the first time to achieve linear J scaling as a function of offset frequency. For a simple mixture of eight aromatic compounds, it is demonstrated experimentally that a 1D-SHOT $\{^1\text{H}\}$ - ^{13}C experiment yields comparable information to a 2D-HSQC and can give full assignment of all coupled spins.

3.1 Introduction

Heteronuclear decoupling is an indispensable tool of modern NMR spectroscopy^{23,31,32,68,112–114}. Multipulse sequences can reduce a given heteronuclear coupling constant J to an effective coupling constant $J_{\text{eff}} = \lambda J$ with a scaling factor λ between zero and one^{115–118}. Here $\lambda = 0$ corresponds to complete decoupling, whereas $0 < |\lambda| < 1$ corresponds to partial decoupling, where the splitting of a doublet is reduced by a factor of λ . A uniform offset-independent scaling factor $\lambda = 0$ is desired for commonly used broadband decoupling sequences. Pulse sequences with uniform scaling factors $0 < |\lambda| < 1$ have been designed to reduce spectral overlap without losing multiplet information^{115–118}.

In this work, we are interested in non-uniform decoupling sequences with a defined offset-dependence of the scaling factors $\lambda(\nu)$. For example, band-selective decoupling sequences are designed to have a scaling factor of zero in a defined offset range and a scaling factor of one in other offset ranges^{119–123}. Another example is the well defined offset-dependent scaling factor of continuous wave (CW) irradiation^{114,124}, which has been extensively used for chemical shift monitoring in pseudo-multidimensional experiments^{125–130}. In favorable cases, this robust, efficient and fast method allows to reduce the number of dimensions in multidimensional NMR experiments by one, saving acquisition time by avoiding time-consuming coherence transfer and indirect evolution steps^{128–131}. Related experimental approaches to reduce the dimensionality of NMR experiments based on the scaling of coupling evolution include SPEED (single-point evaluation of the evolution dimension)¹³² and coupling evolution during adiabatic pulses¹³³.

For correlations based on large heteronuclear J -couplings, tailored decoupling sequences may be considered as an alternative to fast 2D experiments, such as gradient-based experiments to obtain two-dimensional spectra in a single-scan, where different evolution periods are encoded in separate subvolumes of the sample³⁶, non-linear sampling¹³⁴, simultaneous data acquisition¹³⁵, projection NMR spectroscopy¹³⁶, Hadamard spectroscopy¹³⁷, and fast pulsing methods¹³⁸. Based on these approaches and their combinations, the amount of time required for the acquisition of correlation spectra can be significantly reduced, which continues to be a major goal in NMR method development¹³⁹.

In this paper, we present an efficient approach to design pulse sequences that can create virtually arbitrary offset profiles of the scaling factor $\lambda(\nu)$. This approach is an extension of a recently introduced optimal tracking algorithm²³ that is based on principles of optimal control theory^{17,19,21,24,70,140,141}. This makes it possible to optimize entire decoupling sequences *de novo*, in contrast to conventional approaches that are based on individual composite or shaped pulses (inversion pulses for complete decoupling) that are expanded in various cycles or super cycles^{68,113}. Our

method is evaluated in simulations and corresponding experiments for cases of heteronuclear decoupling sequences with different offset-dependent scaling factors $\lambda(\nu)$. We demonstrate that decoupling sequences with linear offset-dependent scaling factors can efficiently encode chemical shift correlations from an indirect dimension. Finally, we discuss possible applications and limitations of this approach.

3.2 Theory

We consider a system consisting of two heteronuclear spins $1/2$, where spin I is observed while spin S is irradiated. For the design of decoupling sequences, the relevant Hamiltonian of the spin system is given by²³

$$\mathcal{H}(t) = 2\pi\nu S_z + 2\pi J S_z I_z + \mathcal{H}_{\text{RF}}^S(t), \quad (3.1)$$

where ν is the offset frequency of spin S , J is the heteronuclear coupling constant and $\mathcal{H}_{\text{RF}}^S(t)$ is the radio frequency (RF) term representing the decoupling sequence with

$$\mathcal{H}_{\text{RF}}^S(t) = 2\pi \epsilon \{u_x(t)S_x + u_y(t)S_y\}. \quad (3.2)$$

The controls $u_x(t)$ and $u_y(t)$ are the nominal amplitudes of the x and y components of the RF field in the doubly rotating frame and ϵ is a RF scaling factor, which takes into account RF inhomogeneity and miscalibration effects.

Note that the chemical shift term $2\pi\nu_I I_z$ of spin I commutes with $\mathcal{H}(t)$ and can be ignored in the analysis. Potential types of additional homonuclear and heteronuclear couplings are summarized in Fig. 3.1 for a system of four coupled spins consisting of spins S , S' , I and I' . Figs. 3.1 A and B correspond to the cases, where the homonuclear S - S' coupling is in the strong and weak coupling limit, respectively.

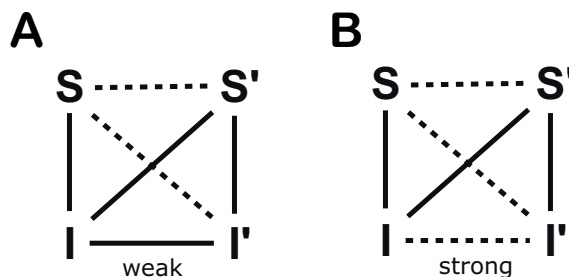


Figure 3.1: Depiction of a system of four coupled spins consisting of spins S , S' , I and I' . Panels A and B correspond to the cases, where the homonuclear S - S' coupling is in the strong and weak coupling limit, respectively. Unproblematic couplings are represented by solid lines, while couplings that do not commute with $\mathcal{H}(t)$ are shown as dashed lines.

In the figure, the unproblematic couplings are represented by solid lines, whereas the couplings that do not commute with $\mathcal{H}(t)$ are shown as dashed lines: In the weak coupling limit, homonuclear coupling terms $2\pi J_{II'} I_z I'_z$ between spins I and I' commute with $\mathcal{H}(t)$. Heteronuclear couplings $2\pi J_{IS'} I_z S'_z$ between spin I and other

S' spins as well as $2\pi J_{I'S'}I'_zS'_z$ between spins I' and S' also commute with $\mathcal{H}(t)$ and hence do not interfere with the scaling of the I - S coupling. The former case is shown in Fig. 3.11 of the Appendix B for a CH_2 group with equivalent proton spins, corresponding to the case where $J_{IS} = J_{IS'}$ is large and $J_{SS'} = 0$. Homonuclear coupling terms between I spins in the strong coupling limit and homonuclear couplings between S and S' spins (in the strong or weak coupling limit) do not commute with $\mathcal{H}(t)$ and can potentially be harmful. However, in realistic settings, where the coupling J_{IS} of interest is a large one-bond coupling that can still be resolved after substantial (but non-zero) scaling, it can be shown that these non-commuting terms have only minor effects on the decoupling performance. Corresponding simulations are shown in Appendix B for the case of a I - S - S' system with weak and strong $J_{SS'}$ couplings (Fig. 3.12), for the case of a CH_2 group with diastereomeric protons with $\nu_S \neq \nu_{S'}$, non-zero $J_{SS'}$ and large $J_{IS} \approx J_{IS'}$ couplings (Fig. 3.13), and for the case where I and S are both coupled to I' (Fig. 3.14). In the following, we will consider an isolated spin pair, consisting of a single spin I coupled to a single spin S .

Without RF irradiation ($\mathcal{H}_{\text{RF}}^S(t) = 0$), the evolution of the initial density operator $\rho(0) = I_x$ is $\rho(t) = I_x \cos(\pi Jt) + 2I_y S_z \sin(\pi Jt)$ and the modulation of the expectation value

$$\langle I_x \rangle(t) = \cos\{\pi Jt\} \quad (3.3)$$

results in a spin I doublet with splitting J in the resulting spectrum after Fourier transformation. The splitting is independent of ν , as the spin S offset term commutes both with $\rho(0)$ and the coupling term $2\pi J S_z I_z$.

In the presence of RF irradiation ($\mathcal{H}_{\text{RF}}^S(t) \neq 0$), the detected signal in general depends on the offset frequency ν of spin S (and the RF scaling factor ϵ). Our goal is to find RF sequences that create a scaled splitting of the spin I doublet with a desired offset dependence of the scaling factor $\lambda(\nu)$, corresponding to a reduced effective coupling constant

$$J_{\text{eff}}(\nu) = \lambda(\nu)J. \quad (3.4)$$

This is achieved if the detected signal

$$s(\epsilon, \nu, t) = \langle I_x \rangle(\epsilon, \nu, t) \quad (3.5)$$

matches the target modulation function

$$g(\nu, t) = \cos\{\lambda(\nu) \pi Jt\}, \quad (3.6)$$

where $\langle I_x \rangle(\epsilon, \nu, t)$ is the expectation value of I_x for a given rf scaling factor ϵ and offset ν at time t . In practice, the spin I signal $s(t)$ is not detected continuously but only at discrete time points T_0, \dots, T_N and in the following we use the short-hand notation $s_k(\epsilon, \nu) = s(\epsilon, \nu, T_k)$ to refer to the signal at these time points.

The optimization of a pulse sequence relies on the definition of a suitable *global* quality factor Φ , which reflects its overall performance for a desired range of offsets ν and RF scaling factors ϵ . For a given offset ν and RF scaling factor ϵ , the performance of the pulse sequence is measured by a *local* quality factor $\varphi(\nu, \epsilon)$, where the best achievable quality factor is $\varphi(\nu, \epsilon) = 1$ corresponds to the case where the detected signal $s_k(\epsilon, \nu)$ precisely follows the desired target modulation function $g(\nu, T_k)$.

For the case of broadband decoupling, in²³ we used the following simple definition for the local quality factor:

$$\varphi_{\text{bb}}(\nu, \epsilon) = \frac{1}{N+1} \sum_{k=0}^N s_k(\epsilon, \nu), \quad (3.7)$$

which can also be expressed in the form

$$\varphi_{\text{bb}}(\nu, \epsilon) = 1 + \frac{1}{N+1} \sum_{k=0}^N (s_k(\epsilon, \nu) - g(\nu, T_k)) \quad (3.8)$$

with $g(\nu, t) = 1$. Note that in this case $s_k(\epsilon, \nu)$ is always smaller or equal to $g(\nu, T_k) = 1$. However, this is in general not the case for heteronuclear decoupling sequences with tailored offset dependence, where the target function $g(\nu, t)$ is modulated. In this case, the quality factor can be defined as the sum of squared residuals, with a residual being the difference between the actual signal and the target function:

$$\varphi_{\text{tailored}}(\nu, \epsilon) = 1 - \frac{1}{N+1} \sum_{k=0}^N \underbrace{(s_k(\epsilon, \nu) - g(\nu, T_k))^2}_{\text{squared residuals}}. \quad (3.9)$$

The global quality factor Φ for a J scaling sequence can be defined as the local quality factors $\varphi(\nu, \epsilon)$ averaged over all offsets ν and RF scaling factors ϵ of interest. For simplicity, here we assume an equal weight for all offsets and RF scaling factors, resulting in the overall performance function

$$\Phi = \frac{1}{N_\nu N_\epsilon} \sum_{q=1}^{N_\nu} \sum_{p=1}^{N_\epsilon} \varphi_{\text{tailored}}(\nu^{(q)}, \epsilon^{(p)}), \quad (3.10)$$

with N_ν discrete offsets $\nu^{(q)}$ and N_ϵ discrete RF scaling factors $\epsilon^{(p)}$ that are evenly spaced in the desired range of offset frequencies and RF scaling factors for a given application.

We consider a pulse sequence that is characterized by $N \cdot M$ control amplitudes $u_x(j)$ and by $N \cdot M$ control amplitudes $u_y(j)$ with $1 \leq j \leq N \cdot M$, where M is the number of time slices Δt between two successive detection points T_k and T_{k+1} .

Hence, following the approach introduced in²³, heteronuclear decoupling sequences with desired offset depending scaling factors $\lambda(\nu)$ can efficiently be optimized by tracking the desired modulation function $g(\nu, T_k)$ (see Appendix A) and we refer to this class of heteronuclear decoupling sequences as SHOT pulses (**S**caling of **H**eteronuclear couplings by **O**ptimal **T**racking).

3.3 Results

3.3.1 Linear J scaling as a function of offset

The effects of a perturbing continuous-wave (CW) radiofrequency field on heteronuclear spin couplings have been discussed in the literature since the early days of NMR^{112,114,124} and an apparent scaling depends on the offset of the irradiation frequency. Using average Hamiltonian theory, the scaling factor λ_{CW} has been determined as a function of the offset frequency ν and the RF amplitude u during CW irradiation on spin S ¹⁴²

$$\lambda_{cw} = \frac{\nu}{\sqrt{\nu^2 + u^2}}. \quad (3.11)$$

As a starting point for comparison with new off-resonance decoupling pulse sequences, we have simulated and experimentally reproduced this non-linear scaling effect of off-resonance CW irradiation with RF amplitude $u = 500$ Hz for a sample of ¹³C-labelled sodium formate (HCOONa, Sigma Aldrich, St. Louis, USA) dissolved in D₂O (see Fig. 3.2).

For simulations, we assumed a relaxation rate constant $\kappa = 30/s$. All experiments were performed on a Bruker Avance III 14.1 T NMR spectrometer (Bruker BioSpin, Rheinstetten, Germany). The C-H coupling constant of the ¹H-¹³C moiety of sodium formate was determined to be $J = 195$ Hz. Irradiation was performed on the carbon spins for $t = 512$ ms, while the proton spins were observed. The irradiation frequency offset ν was shifted over a range of $[-700 \text{ Hz}, +700 \text{ Hz}]$ with 101 different offsets equally spaced around the resonance frequency of the carbon spins. Simulations and post processing of spectra were done with MATLAB (The Mathworks, Natwick, USA).

Additionally we want to point out here, that the RF amplitude of the sequence applied to spin S can be precisely calibrated based on the known offset dependence of CW decoupling (c.f. eq. 3.11). We used this approach to calibrate the RF amplitude of all pulses described in this paper, since the accuracy was found to be better compared to conventional calibrations based on incrementing pulse lengths or RF power.

In contrast to CW decoupling, we wanted to optimize a decoupling pulse, which can achieve linear scaling of J_{eff} as a function of offset. As our goal we choose a linear scaling in an offset range of $-700 \text{ Hz} \leq \nu \leq +700 \text{ Hz}$. Pulses should be robust to RF miscalibrations of $\pm 5\%$. To achieve this, we set up an optimal control program based on the GRAPE tracking approach based on the local quality factor $\varphi_{\text{tailored}}(\nu, \epsilon)$ (c.f. Eq. [3.9]), where we defined the desired offset-dependent J scaling factor as

$$\lambda_{\text{lin}}(\nu) = (1400 \text{ Hz})^{-1}\nu + 0.5 \quad \text{for} \quad -700 \text{ Hz} \leq \nu \leq +700 \text{ Hz}, \quad (3.12)$$

which grows linearly from a value of 0 for $\nu = -700$ Hz to a value of 1 for $\nu = +700$ Hz.

The pulse was optimized for 101 offsets in the chosen range and 3 different RF scaling

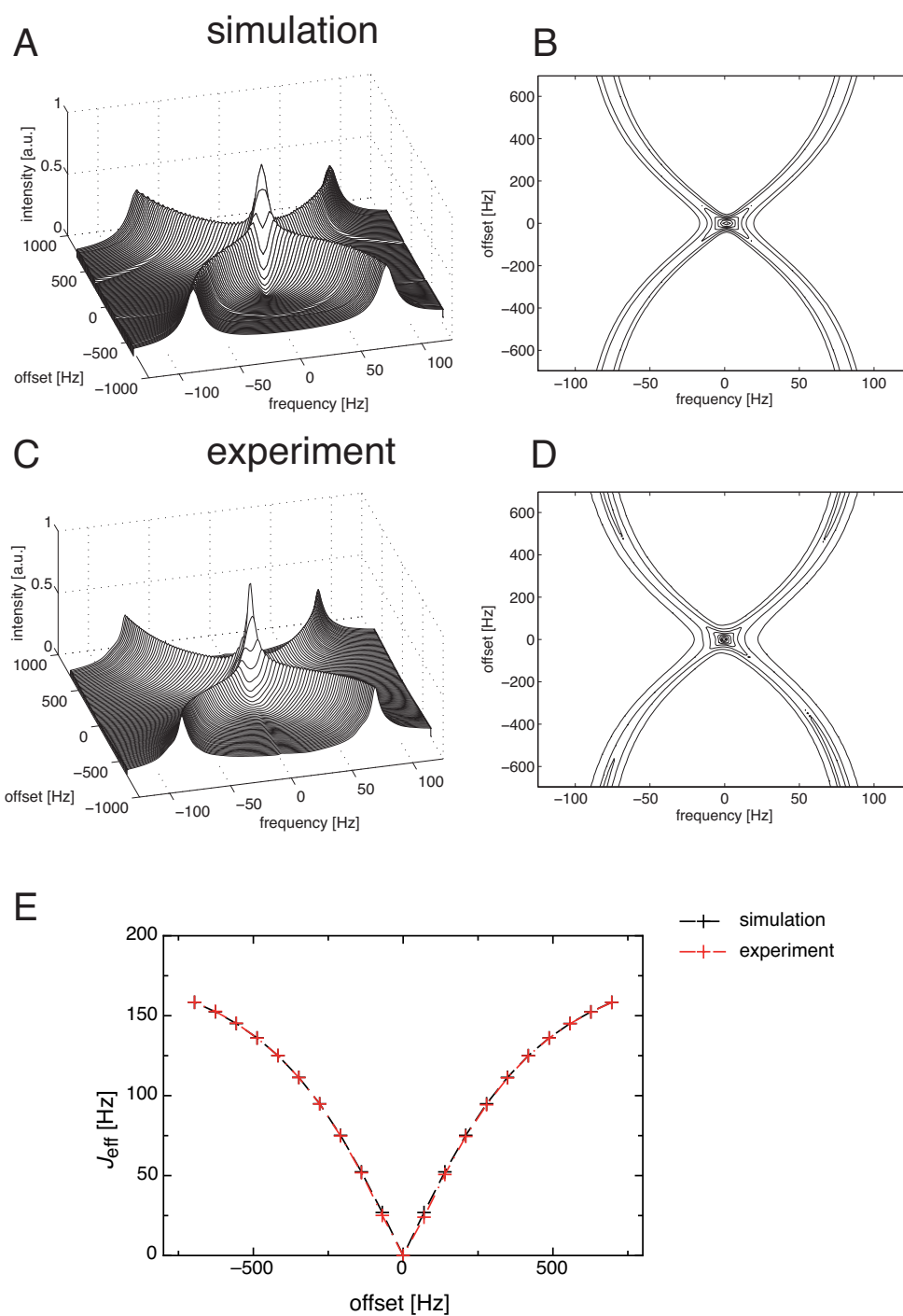


Figure 3.2: Simulated (A, B) and experimental (C, D) multiplet splitting of spin I for CW decoupling (with RF amplitude $u = 500$ Hz) of spin S as a function of frequency offset ν (A, C: stacked plots; B, D; contour plots with contour levels of 0.3, 0.4, ..., 0.9, 1.0). Panel E shows simulated and experimentally determined effective coupling constants as a function of offset. The SHOT pulse is given in Bruker file format in the supplementary material.

factors ϵ , compensating RF miscalibrations of $\pm 5\%$. The pulse is set for a total time of 512 ms and 1280 digitization points. Optimization of a pulse sequence on a standard desktop computer takes approximately 2 days. The final pulse sequence and a scheme of data acquisition is shown in Fig. 3.3 A,B,C.

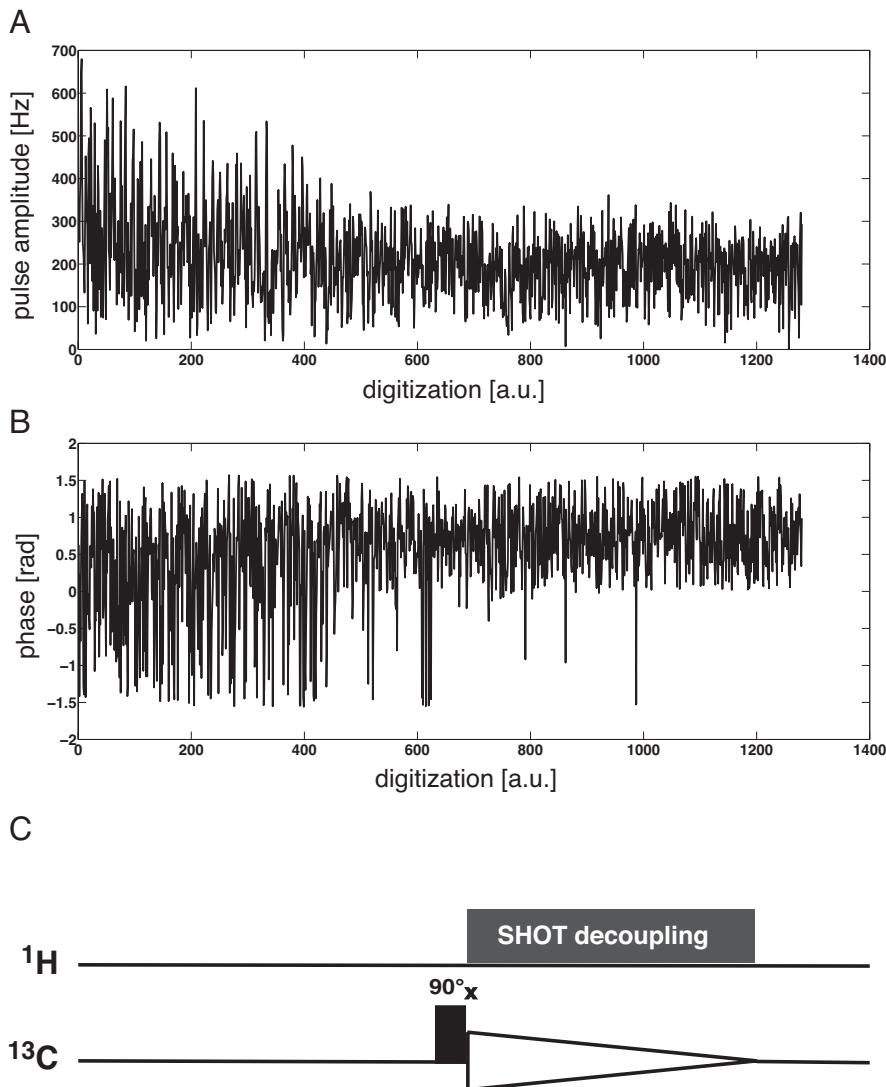


Figure 3.3: Amplitude (A) and phase (B) modulation of a SHOT decoupling sequence with a linear scaling of the effective coupling constant as a function of offset. The pulse is digitized in 1280 points and optimized for a total acquisition time of 512 ms. A SHOT decoupling experiment consists of an excitation pulse followed by acquisition of spin I (represented in the present example by ^{13}C) while spin S represented in the present example by ^1H) is irradiated by a SHOT decoupling sequence (C).

We have shown with reasonable match between experiment and simulation that linearly scaled decoupling can be achieved (see Fig. 3.4). Compared to the CW experiment, we find increased sideband amplitudes which also match the simulations (see the discussion for the elimination or the potential use of decoupling sidebands). Experimental conditions were the same as for CW decoupling. Pulse amplitudes

were calibrated by matching CW decoupling offset profiles to the theoretically predicted profiles. Experimental effective coupling constants J_{eff} were extracted from the experimental spectra using the method described in¹⁴³ to correct for the effect of finite linewidth.

3.3.2 Arbitrarily tailored J scaling as a function of offset

Applications of SHOT decoupling sequences are not limited to simple linear scaling of the effective coupling constant $\lambda(\nu)$ as a function of offset. In principle, any functional form of $\lambda(\nu)$ can be used (with $|\lambda(\nu)| \leq 1$). This is demonstrated in a first example for the optimization of a SHOT sequence for a non-continuous function $\lambda(\nu)$ defined as

$$\lambda_{\text{jump}}(\nu) = \begin{cases} (700 \text{ Hz})^{-1}\nu + 1 & \text{for } -700 \text{ Hz} \leq \nu < 0 \text{ Hz} \\ (700 \text{ Hz})^{-1}\nu & \text{for } 0 \text{ Hz} \leq \nu \leq 700 \text{ Hz}. \end{cases} \quad (3.13)$$

The simulation of the optimized pulse for such a decoupling pattern and its experimental validation is shown in Fig. 3.5.

Second, we optimized a SHOT decoupling pulse that starts with a linear scaling as a function of offset, continues with a region of unscaled coupling, and finishes with another linear scaling, corresponding to the function $\lambda(\nu)$ defined as

$$\lambda_{\text{step}}(\nu) = \begin{cases} (467 \text{ Hz})^{-1}(\nu + 700 \text{ Hz}) & \text{for } -700 \text{ Hz} \leq \nu < -233 \text{ Hz} \\ 1 & \text{for } -233 \text{ Hz} \leq \nu < 233 \text{ Hz} \\ (467 \text{ Hz})^{-1}(\nu - 233 \text{ Hz}) & \text{for } 233 \text{ Hz} \leq \nu \leq 700 \text{ Hz}. \end{cases} \quad (3.14)$$

The result of the pulse optimization for such a decoupling pattern and its experimental validation is shown in Fig. 3.6.

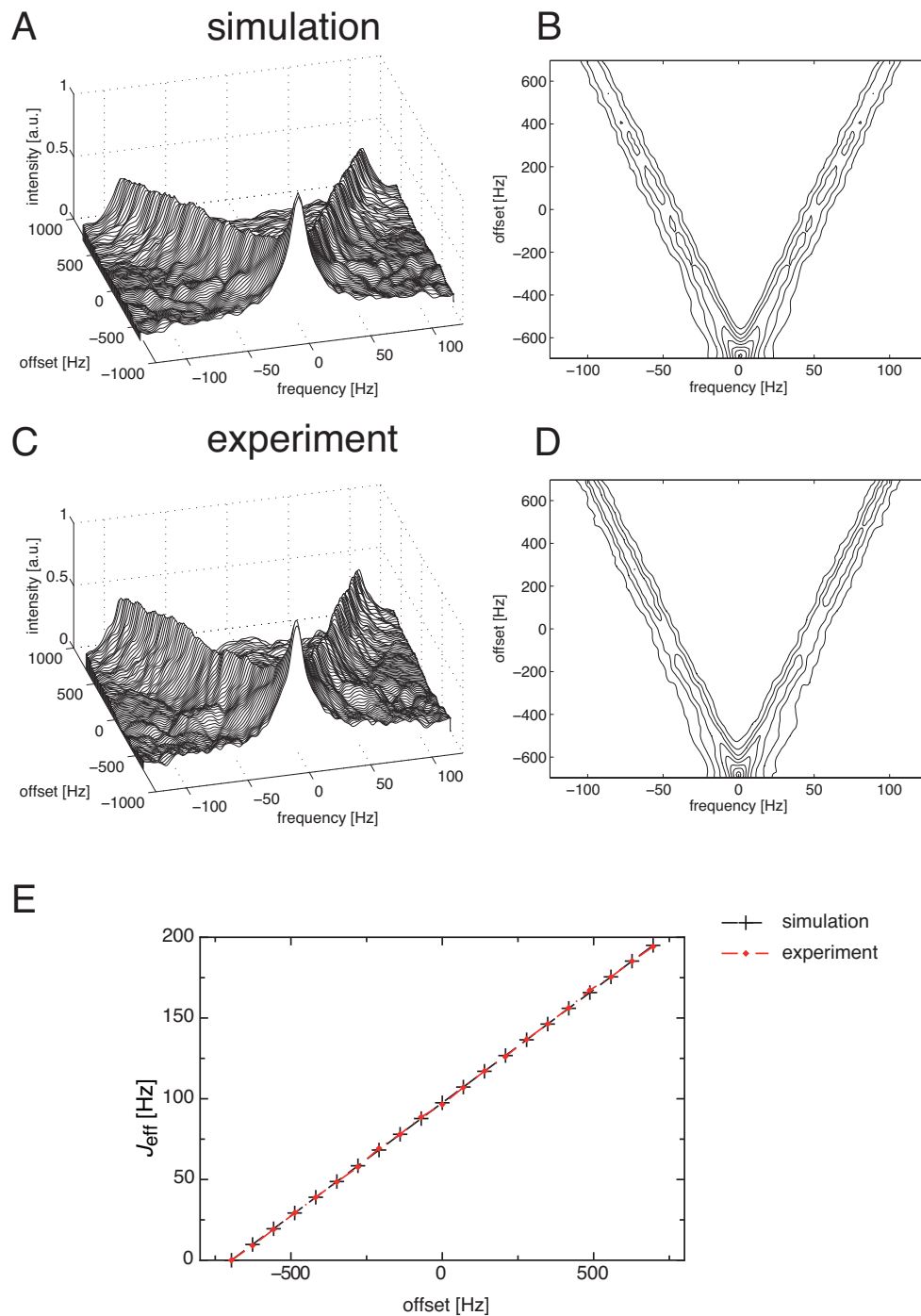


Figure 3.4: Simulated (A, B) and experimental (C, D) multiplet splitting of spin I for SHOT decoupling designed for a linear scaling (c.f. Eq. 3.12) of the effective coupling constant as a function of offset (A, C: stacked plots; B, D: contour plots with contour levels of 0.3, 0.4, ..., 0.9, 1.0). Panel E shows simulated and experimentally determined effective coupling constants as a function of offset. The SHOT pulse is given in Bruker file format in the supplementary material.

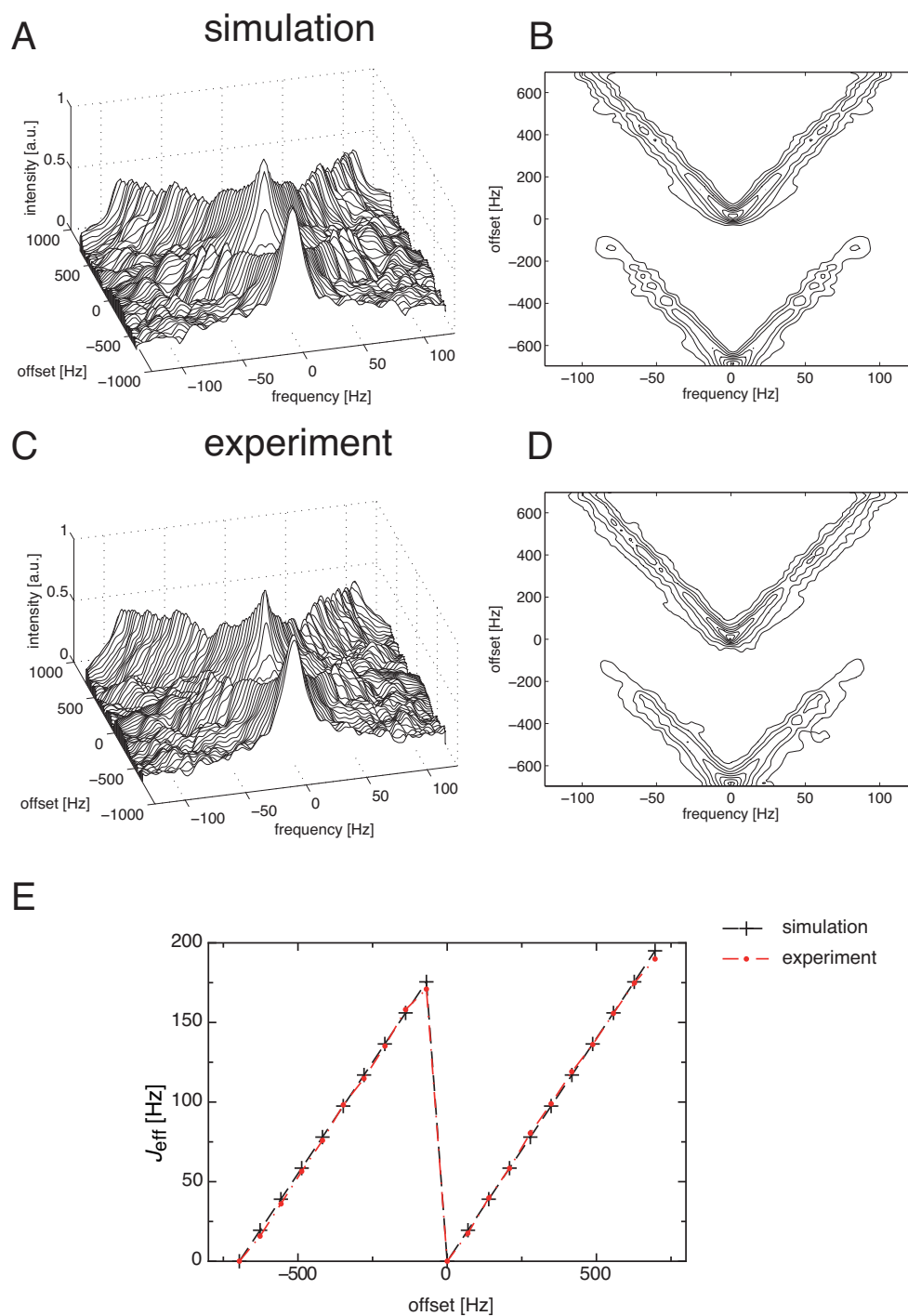


Figure 3.5: Simulated (A, B) and experimental (C, D) multiplet splitting of spin I for SHOT decoupling designed for a non-continuous jump pattern (c.f. Eq. 3.13) of the effective coupling constant as a function of offset (A, C: stacked plots; B, D: contour plots with contour levels of 0.3, 0.4, ..., 0.9, 1.0). Panel E shows simulated and experimentally determined effective coupling constants as a function of offset. The SHOT pulse is given in Bruker file format in the supplementary material.

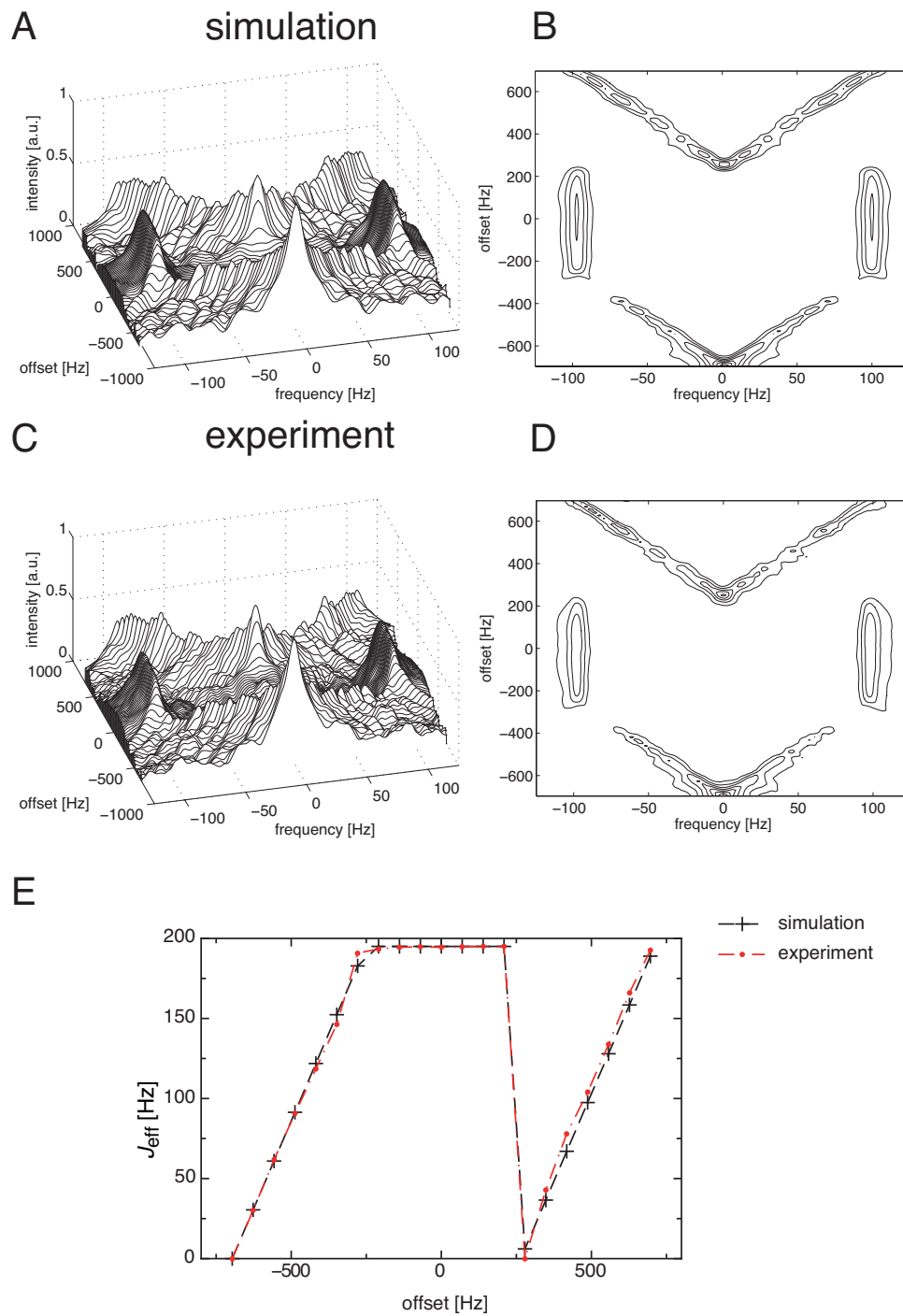


Figure 3.6: Simulated (A, B) and experimental (C, D) multiplet splitting of spin I for SHOT decoupling designed for a step pattern (c.f. Eq. 3.14) of the effective coupling constant as a function of offset (A, C: stacked plots; B, D: contour plots with contour levels of 0.3, 0.4, ..., 0.9, 1.0). Panel E shows simulated and experimentally determined effective coupling constants as a function of offset. The SHOT pulse is given in Bruker file format in the supplementary material.

3.3.3 Chemical shift correlations from linear scaling of heteronuclear couplings

The idea of using off-resonance decoupling to obtain chemical shift correlations in 1D-spectra was proposed by R. Ernst¹²⁴ and has then been used for the acquisition of pseudo-multidimensional spectra^{127–130}. However, so far this concept was limited to using CW decoupling for scaling J -couplings. As the accuracy of the obtained chemical shifts depends on the slope of the J -scaling function $J_{\text{eff}}(\nu)$, the accuracy is offset dependent for the nonlinear offset dependence of $J_{\text{eff}}(\nu)$ for CW decoupling (c.f. Eq. [3.11]).

Here, we demonstrate that it is possible to optimize SHOT decoupling sequences with a linear scaling of the effective coupling constant as a function of offset, which makes it possible to encode the frequency offsets ν of heteronuclear spins with an accuracy that is independent of ν . For the demonstration of this method, we prepared a test sample of eight different compounds with ^{13}C resonances in the same frequency region, all of them having one-bond C-H spin couplings. We prepared a solution containing approximately 100 mg of each of the following compounds dissolved in 1 ml chloroform: 1,3,5-Trimethylbenzene, 2-Bromomesitylene, 1,3,5-Tris(bromomethyl)benzene, 1,3,5-Triethylbenzene, 1,3,5-Trichlorobenzene, 2,4,6-Tribromoanisole, 1,3,5-Tribromobenzene, 1,3,5-Tris(trifluoromethyl)benzene. A proton NMR spectrum of this solution is shown in Fig. 3.7 A. Since there are only ^{13}C nuclei at natural abundance in this sample, the J -splitting of the C-H coupling can be observed in the scaled spectrum (B) showing the large ^1H - ^{12}C peaks with its ^1H - ^{13}C satellites. A SHOT sequence similar to the one shown in Fig. 3.3 optimized for linear scaling of the J -couplings is irradiated on the ^1H spins at a chemical shift of 7.13 ppm. The pulse is designed for a total bandwidth of 1.66 ppm (corresponding to 1 kHz for a ^1H frequency of 600 MHz) covering the entire proton region of interest (see Fig. 3.7).

The ^{13}C nuclei are observed while the ^1H nuclei are irradiated with the SHOT pulse. The pulse sequence is depicted in Fig. 3.3 C. Fig. 3.8 shows a fully coupled reference spectrum (2048 scans), a broadband decoupled spectrum using WALTZ-16 (1024 scans), the experimental SHOT spectrum (2048 scans), a simulated SHOT spectrum and the residual difference between the simulated and experimental SHOT spectra.

Each resonance marked by a dashed vertical line corresponds to one of the eight compounds and was labelled by capital letters from A-H (see Table 1). From the broadband WALTZ-16-decoupled and the fully coupled spectra, we determined the individual ^{13}C chemical shifts $\delta(^{13}\text{C})$ of each compound and the respective unscaled coupling constants J (c.f. Table 1). Table 1 also summarizes the experimental J scaling factors $\lambda_{\text{SHOT}} = J_{\text{SHOT}}/J$ that were determined by comparing the scaled splittings in the SHOT-decoupled spectrum with the splittings in the fully coupled spectrum. Based on the chosen ^1H transmitter frequency and the known linear offset dependence of the SHOT J scaling factor, the corresponding ^1H chemical shifts are given by

$$\delta_{\text{SHOT}}(^1\text{H}) = \lambda_{\text{SHOT}} \cdot 1.666 \text{ ppm} + 6.297 \text{ ppm}. \quad (3.15)$$

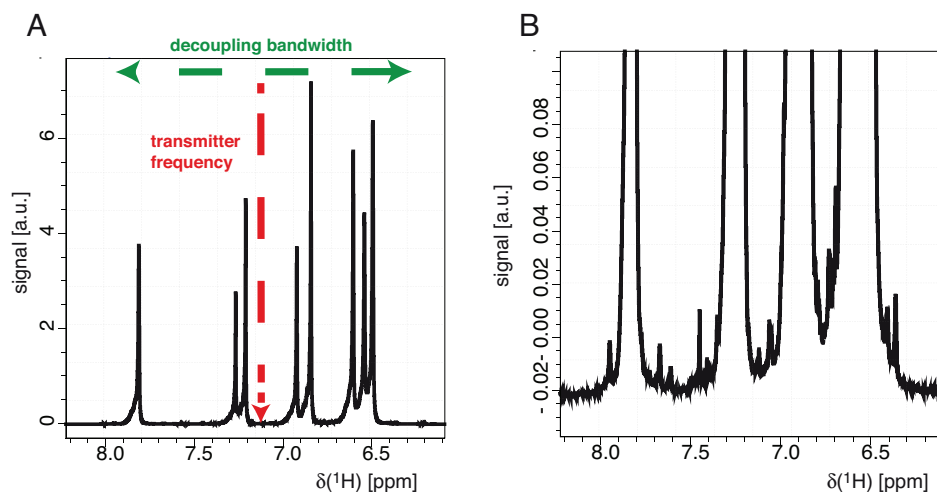


Figure 3.7: Proton spectrum of mixture of 1,3,5-Trimethylbenzene, 2-Bromomesitylene, 1,3,5-Tris(bromomethyl)benzene, 1,3,5-Triethylbenzene, 1,3,5-Trichlorobenzene, 2,4,6-Tribromoanisole, 1,3,5-Tribromobenzene, 1,3,5-Tris(trifluoromethyl)benzene (with ^{13}C in natural abundance) dissolved in 1 ml chloroform. The decoupling bandwidth of 1 kHz (corresponding to 1.66 ppm at 600 MHz ^1H frequency) and the irradiation frequency of the SHOT decoupling sequence is indicated in the region of interest (A). The signals of protons coupled to ^{13}C form the weak ^{13}C satellites shown in the scaled spectrum (B).

The resulting ^1H chemical shifts determined using SHOT decoupling and the chemical shifts determined from a 2D-HSQC reference spectrum are summarized in Table 3.1.

Conversely, the offsets ν determined from the SHOT decoupling experiment were used together with the measured unscaled couplings J and the integrated peak areas can be used to simulate the SHOT spectrum including the effects of decoupling sidebands (compare Fig. 3.8) and a reasonable match is found between experimental and simulated SHOT-decoupled spectra.

In order to assess the accuracy of the ^1H chemical shift determined by the 1D-SHOT approach, a conventional two-dimensional ^1H - ^{13}C HSQC experiment with ^1H decoupling was performed to obtain unequivocal correlations between the coupled ^1H and ^{13}C resonances (see Fig. 3.9 A and Table 1). The ^1H - ^{13}C correlations found by the 1D-SHOT approach are indicated by circles in Fig. 3.9 A. Fig. 3.9 B) shows the correlation between the determined ^1H chemical shift using the 2D ^1H - ^{13}C HSQC experiment and the SHOT decoupling approach. The largest difference of 0.08 ppm is found for compound B, whereas most errors are smaller than 0.03 ppm and the assignment of the signals in the 1D proton spectrum (c.f. Fig. 3.7) to the signals in the ^{13}C spectrum was unambiguous. Using chemical shift simulation software (ChemDraw, PerkinElmer, Cambridge, USA), we assigned all resonances to the corresponding compounds: A (1,3,5-Tris(bromomethyl)benzene), B (1,3,5-Tris(trifluoromethyl)benzene), C (1,3,5-Trimethylbenzene), D (1,3,5-Triethylbenzene), E (2-Bromomesitylene), F (1,3,5-Trichlorobenzene), G (2,4,6-Tribromoanisole), H (1,3,5-Tribromobenzene).

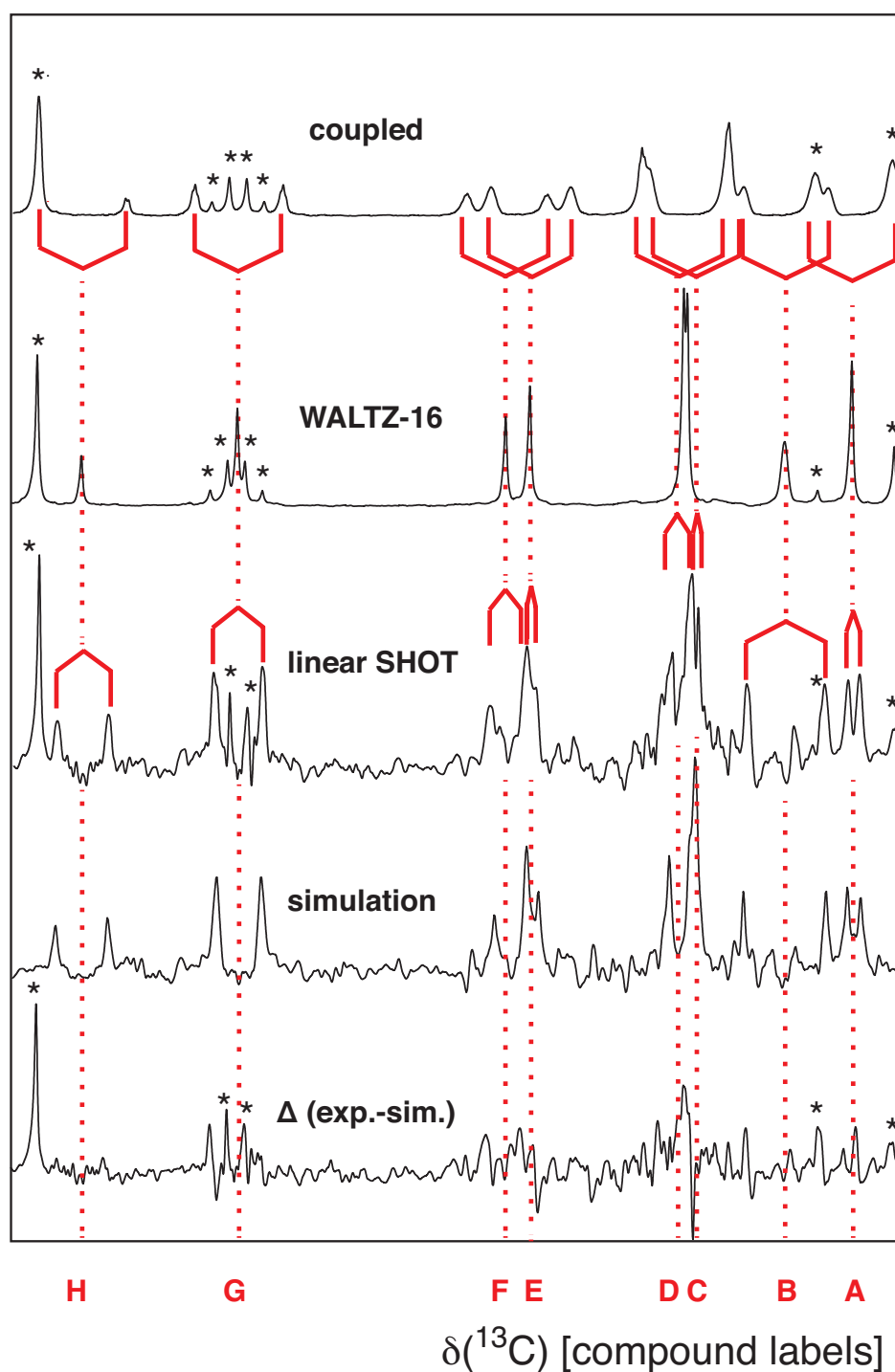


Figure 3.8: ^{13}C spectra of the mixture of eight compounds: (1) a fully coupled reference spectrum (2048 scans), (2) broadband decoupled spectrum using WALTZ-16 (1024 scans), (3) experimental SHOT spectrum (2048 scans) vertically scaled by a factor of 1.25, (4) simulated SHOT spectrum, (5) difference between the experimental (3) and simulated (4) SHOT spectra. Each resonance marked by a dashed vertical line corresponds to one of the eight compounds and was labeled by capital letters from A-H and the corresponding chemical shifts are summarized in Table 1. Additional peaks arising from other resonances are marked by an asterisk. The SHOT pulse is given in Bruker file format in the supplementary material.

compound label	$\delta(^{13}\text{C})$ [ppm]	J [Hz]	$\lambda_{\text{SHOT}} (J_{\text{SHOT}}/J)$	$\delta_{\text{SHOT}}(^1\text{H})$ [ppm]	$\delta(^1\text{H})$ [ppm]
A	124.5	153.4	0.15	6.58	6.60
B	125.4	164.8	0.93	7.89	7.81
C	126.6	186.4	0.08	6.46	6.49
D	126.7	172.5	0.29	6.82	6.84
E	128.7	157.1	0.12	6.54	6.54
F	129.0	160.0	0.34	6.91	6.92
G	132.5	173.5	0.50	7.16	7.20
H	134.6	173.5	0.59	7.32	7.26

Table 3.1: Observed chemical shifts and coupling constants J from a ^{13}C reference spectrum and their scaling factor λ from a SHOT $^{13}\text{C}\{-^1\text{H}\}$ spectrum. Each C-H doublet is assigned to one compound specified by a label from A-H. The ^1H shifts derived from the $^{13}\text{C}\{-^1\text{H}\}$ SHOT experiment are compared to the measured ^1H shifts from a 2D-HSQC experiment.

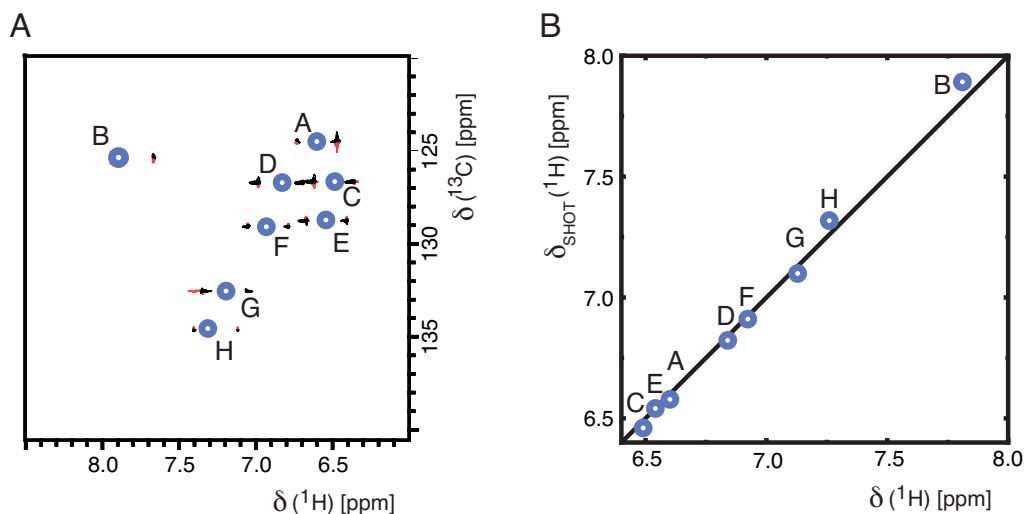


Figure 3.9: Pseudo-2D representation of the correlated resonances based on a 1D-SHOT experiment (circles) superimposed on a standard 2D ^{13}C -decoupled HSQC spectrum (A). In the right panel, the ^{13}C chemical shifts $\delta_{\text{SHOT}}(^1\text{H})$ derived from the 1D-SHOT experiment are plotted against the measured ^{13}C chemical shifts $\delta(^1\text{H})$ from the 2D-HSQC experiment (B).

3.4 Discussion and conclusion

In this work we have presented a new class of so-called SHOT decoupling sequences that can achieve virtually arbitrary J -scaling as a function of offset. SHOT pulses are designed with an optimal control algorithm, which allows us to tailor the effective coupling constant $J_{\text{eff}}(\nu)$ by tracking the desired time evolution of the coupled spin system as a function of offset, also taking RF inhomogeneities into account.

One application of SHOT pulses is to use their full control over the J -scaling function $\lambda(\nu)$ to encode chemical shift of an irradiated nucleus indirectly and efficiently in a 1D experiment. We have demonstrated in an experiment, that a 1D-SHOT $\{^1\text{H}\}$ - ^{13}C experiment yields equivalent chemical shift correlations as a 2D-HSQC for a simple mixture of aromatic compounds and can give full assignment of all corresponding coupled spins. The idea of indirect chemical shift encoding has previously been realized only by CW decoupling and has been shown to be a robust method to establish heteronuclear correlations without actually performing a 2D experiment involving time consuming additional coherence transfer and evolution steps. Especially for large proteins, where 4-dimensional correlations are advantageous but very time consuming, off-resonance decoupling was used successfully to save measurement time and increase the resolution^{128,129}. However, encoding chemical shift via CW decoupling has the drawback that the J -coupling is scaled in a non-linear offset-dependence. As the accuracy of the chemical shift encoding depends on the slope of $\lambda(\nu)$ (c.f. eq. 3.11), the chemical shift resolution across pseudo-multidimensional spectra varies for different offsets.

Here we demonstrated that SHOT pulses can create decoupling patterns that are linear over a defined range of offsets or stepwise-defined and that $\lambda(\nu)$ can even be non-continuous with a large jump of $\lambda(\nu)$ within a relatively small range of offsets. As the achievable decoupling patterns are very flexible, SHOT pulses can be tailored to a specific experimental task and the J -scaling function can be adjusted to the needs, e.g. increased chemical shift resolution in just one part of the spectrum. Furthermore, a limit of the maximum allowed average RF power can be taken into account in the optimal control algorithm²² and the pulse can be optimized to be robust against B_1 inhomogeneities. Our linear SHOT pulse shows very good robustness against B_1 homogeneity in the $\pm 5\%$ region it was optimized for. Compared to CW it shows comparable line-broadening up to $\pm 10\%$ (see Appendix B Fig. 3.10). SHOT encoding can be also combined with spin-state selective off-resonance decoupling¹²⁸, making interpretation of spectra easier and reducing spectral overlap.

Our new approach to encode chemical shift was presented for a simple mixture of 8 molecules, which contain isolated pairs of heteronuclear coupled spins. In general our approach is not limited to such simple spin systems, as we have shown in simulations: the linear SHOT pulse can e.g. also be applied for CH_2 groups (Fig. 3.11), for spins in the weak-coupling limit ($\Delta\nu = 200$ Hz, $J_{HH'} = 0$ Hz, 8 Hz, -16 Hz) as well as in the strong-coupling limit ($\Delta\nu = 4$ Hz, $J_{HH'} = 0$ Hz, 8 Hz, -16 Hz) (Fig. 3.12), or diastereomers (Fig. 3.13) without significant loss of sensitivity. However, spectral overlap in the direct detected dimension, e.g. when many long-range couplings or many homonuclear couplings are present (Fig. 3.14), may limit the application of SHOT pulses as described previously for off-resonance CW decoupling.

Compared to CW irradiation, the presented SHOT pulses show significant decoupling sidebands (c.f. Fig. 3.2 and Fig. 3.4), which in the current study limited the accuracy with which the encoded chemical shift information could be manually extracted from the 1D-SHOT spectra. Future work will focus on reducing these sidebands, e.g. by cooperative decoupling pulses that are designed to compensate each others imperfections in repeated scans²⁵. However, it is important to note that decoupling sidebands are not random noise but systematic and reproducible. The excellent match between experimental and simulated decoupling sidebands (c.f. Figs. 3.4, 3.5, 3.6, 3.8) suggests that the offset information that is also contained in the decoupling sidebands could be exploited by automated fitting procedures¹⁴⁴, to make it possible to extract chemical shift information even in the presence of overlapping resonances and to increase the accuracy of the extracted chemical shift information. Another approach to multi-dimensional correlation experiments without coherence transfer steps was recently introduced by Prestegard et al.¹⁴⁵. Their technique called MD-DIRECT encodes an additional chemical shift dimension by multi-band frequency-selective decoupling during acquisition. This Hadamard type of experiment obtains direct chemical shift resolution, since it is a true multidimensional method. With SHOT pulses, an additional dimension is encoded indirectly in a one-dimensional spectrum. In addition to a reference spectrum, in principle only a single 1D-SHOT experiment is necessary, which in fact can be acquired in a single shot if the signal-to-noise ratio is large enough, e.g. if isotopically enriched samples or hyperpolarization techniques are used. As recently shown in the Hilty group for the case of off-resonance CW decoupling, the offset-dependent scaling of heteronuclear couplings is a very efficient way to acquire chemical shift correlations with hyperpolarized spins¹³¹.

In the present study, chemical shift information was encoded using only a single offset-dependent J scaling function $\lambda(\nu)$. The offset bandwidth and the accuracy of the offsets obtained using this approach can be increased using a set of SHOT decoupling sequences with different scaling patterns and slopes $d\lambda(\nu)/d\nu$. The exploration of this route to obtain high-resolution chemical shift information for a large frequency range is beyond the scope of this paper and will be the subject of future research.

Further potential applications of SHOT decoupling sequences include the scaling of (residual) dipolar couplings in liquid and solid samples, and the tailored scaling of coupling networks in NMR quantum computing experiments. Logic gates such as the CNOT depend on J -coupling constants and could be virtually arbitrarily scaled by SHOT pulses giving full control over the timing of the gate¹⁴⁶. In conclusion we believe that SHOT decoupling sequences are an important addition to the methods available for NMR spectroscopy and that they may find interesting applications in pseudo-multidimensional NMR experiments that are based on the specific manipulation of coupling constants in networks of coupled spins.

3.5 Acknowledgements

We thank Dr. Jorge Neves for his support with decoupling experiments and Dr. Raimund Marx for assistance in the design and preparation of the test samples. F. S. thanks Fonds der Chemischen Industrie, the Faculty Graduate Center Chemistry, TUM Graduate School and the Institute for Advanced Study (IAS) at TUM for financial support. S.J.G. acknowledges support from the DFG (GI 203/6-1) and from Fonds der Chemischen Industrie.

3.6 Appendix A: Gradient for the optimization of amplitude-modulated J scaling sequences

In complete analogy to the derivation outlined in²³, the gradient for a quality factor $\varphi_{\text{bb}}(\nu, \epsilon)$ (c.f. Eq. [3.8]) with respect to the control amplitudes $u_\alpha(j)$ (with $\alpha \in \{x, y\}$) of all time slices ($1 < j \leq MN$) can be expressed to first order in Δt as

$$\begin{aligned} \frac{\delta\varphi_{\text{bb}}(\nu, \epsilon)}{\delta u_\alpha(j)} &= i 2\pi\epsilon\Delta t \frac{1}{N+1} \sum_{k>l} \exp\{-\kappa T_k\} \langle S_\alpha | [\rho'(t_j), \lambda'_k(t_j)] \rangle \\ &= i 2\pi\epsilon\Delta t \frac{1}{N+1} \langle S_\alpha | [\rho'(t_j), \Lambda(t_j)] \rangle. \end{aligned} \quad (3.16)$$

The gradient for the quality factor $\varphi_{\text{tailored}}(\nu, \epsilon)$ for tailored J -scaling (c.f. Eq. [3.9]) can be calculated in analogy

$$\begin{aligned} \frac{\delta\varphi_{\text{tailored}}(\nu, \epsilon)}{\delta u_\alpha(j)} &= -2(\langle I_x | \rho(\epsilon, \nu, T_k) \rangle - g(\nu, T_k)) \\ &\quad \cdot i 2\pi\epsilon\Delta t \frac{1}{N+1} \sum_{k>l} \exp\{-\kappa T_k\} \langle S_\alpha | [\rho'(t_j), \lambda'_k(t_j)] \rangle \\ &= i 2\pi\epsilon\Delta t \frac{1}{N+1} \sum_{k>l} \exp\{-\kappa T_k\} \langle S_\alpha | [\rho'(t_j), \lambda_k^+(t_j)] \rangle \\ &= i 2\pi\epsilon\Delta t \frac{1}{N+1} \langle S_\alpha | [\rho'(t_j), \Lambda^+(t_j)] \rangle. \end{aligned} \quad (3.17)$$

We define $\lambda_k^+(t_j)$ as the product of the exterior derivative and $\lambda'_k(t_j)$

$$\lambda_k^+(t_j) = -2(\langle I_x | \rho(\epsilon, \nu, T_k) \rangle - g(\nu, T_k)) \cdot \lambda'_k(t_j). \quad (3.18)$$

It is assumed for simplicity that the relevant terms of the density operator relax with the same rate κ (see²³ for the general case of an arbitrary relaxation super operator).

Here

$$\rho'(t_j) = U_j \dots U_1 \rho(t_0) U_1^\dagger \dots U_j^\dagger \quad (3.19)$$

is the density operator at time point t_j that is obtained by unitarily evolving the initial density operator $\rho(0) = I_x$ forward in time. We call

$$\lambda_k^+(t_j) = U_{j+1}^\dagger \dots U_{kM}^\dagger C^+(T_k) U_{kM} \dots U_{j+1} \quad (3.20)$$

the k^{th} costate at time point t_j that is obtained by unitarily evolving the operator $C^+(T_k) = -2(\langle I_x | \rho(\epsilon, \nu, T_k) \rangle - g(\nu, T_k)) I_x$ backward in time.

The operator $C^+(T_k)$ is a vector Lagrange multiplier and is given by¹⁴⁷

$$C^+(T_k) = \frac{\delta\varphi}{\delta\rho(T_k)}. \quad (3.21)$$

In this simplified model, all relaxation effects are contained in the term $\exp\{-\kappa T_k\}$. The integer $l = \lfloor j/M \rfloor$ is the truncated value (also called floor function or integral value) of the ratio j/M , i.e. the number of complete intervals ΔT before the j^{th} time slice. The condition $k > l$ for the summation in Eq. [3.17] reflects the fact that the control amplitudes $u_x(j)$ and $u_y(j)$ in the j^{th} time slice cannot affect the detected signal at earlier detection points. The operator $\Lambda^+(t_j)$ in (Eq. [3.17]) is defined as

$$\Lambda^+(t_j) = \sum_{k>l} \exp\{-\kappa T_k\} \lambda_k^+(t_j) \quad (3.22)$$

and can efficiently be calculated for all time points $t_0 \leq t_j \leq T_N$ as discussed in²³. Finally, the gradient for the overall quality function Φ (c.f. Eq. [3.10]) is given by the averaged gradients $\delta\varphi_{\text{tailored}}(\epsilon, \nu_S)/\delta u_\alpha(j)$:

$$\frac{\delta\Phi_{\text{tailored}}}{\delta u_\alpha(j)} = \frac{1}{N_\epsilon N_\nu} \sum_{p=1}^{N_\epsilon} \sum_{q=1}^{N_\nu} \frac{\delta\varphi(\epsilon^{(p)}, \nu_S^{(q)})}{\delta u_\alpha(j)}. \quad (3.23)$$

For the optimization of purely phase-modulated RF sequences with constant RF amplitude²⁰ $u_0 = \sqrt{u_x^2 + u_y^2}$, the gradient $\delta\Phi_{\text{tailored}}/\delta\varphi(j)$ is given (to first order in $\Delta t = t_j - t_{j-1}$) by²³

$$\frac{\delta\Phi_{\text{tailored}}}{\delta\varphi(j)} = u_0 \left\{ -\frac{\delta\Phi_{\text{tailored}}}{\delta u_x(j)} \sin \varphi(j) + \frac{\delta\Phi_{\text{tailored}}}{\delta u_y(j)} \cos \varphi(j) \right\}. \quad (3.24)$$

Starting from an initial pulse with rf amplitudes $u_x(t)$ and $u_y(t)$, the pulse performance can be optimized by following the gradient for the overall quality function Φ_{tailored} . In the most simple approach, the gradient information can be used in steepest descent algorithms, but faster convergence can often be found using conjugate gradient or efficient gradient-based quasi-Newton methods²⁷.

3.7 Appendix B: Robustness of SHOT decoupling to different coupling topologies

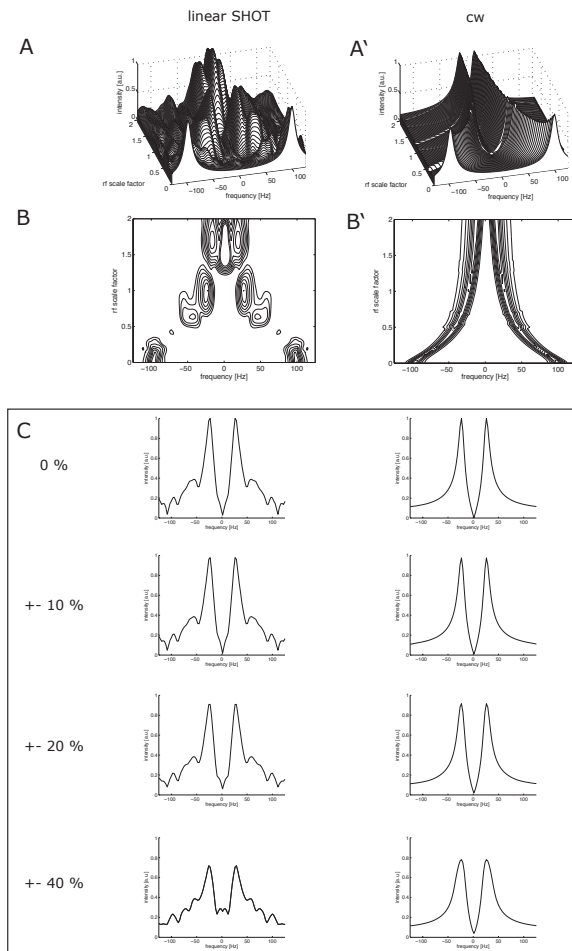


Figure 3.10: Simulated comparison of B_1 inhomogeneity effects on off-resonance decoupling between a linear SHOT pulse (A,B) and CW irradiation (A',B'). All plots are shown for one specific decoupler offset with a scaling factor of $\lambda = 0.25$ for different B_1 field strengths ranging from 0 to 200 percent B_1 ; contour plots with contour levels of 0.3, 0.4, ..., 0.9, 1.0. The SHOT pulse was optimized for $\pm 5\%$ B_1 amplitude and is robust within a range from $\pm 25\%$ as can be seen in Panel B. Panel C shows the effects of B_1 inhomogeneity on the acquired spectra, which were simulated by averaging over the indicated range of B_1 strengths. Both CW and SHOT off-resonance decoupling are robust to B_1 inhomogeneities within a range up to 10%, but in both cases significant line-broadening can be observed the larger the inhomogeneities become.

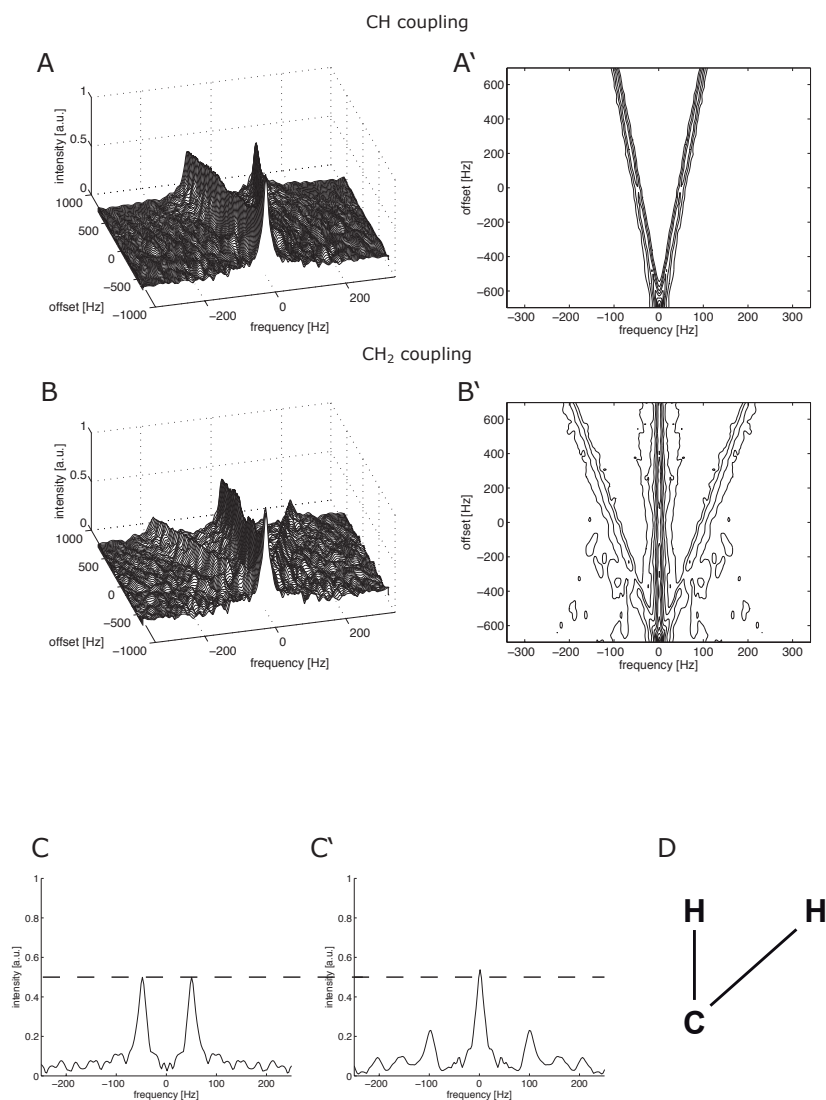


Figure 3.11: Simulated multiplet splitting for linear SHOT decoupling in a CH coupled spin system (A, A') and in a CH₂ coupled spin system (D), with $J_{CH} = 195$ Hz for proton decoupler offsets in the range $\nu[-700$ Hz, $+700$ Hz]. (A, B: stacked plots; A',B': contour plots with contour levels of 0.3, 0.4, ..., 0.9, 1.0). Panel C and C' show spectra for $\lambda = 0.5$, for the CH system (C) and the CH₂ system (C'); both spectra are referenced to the fully decoupled signal intensity.

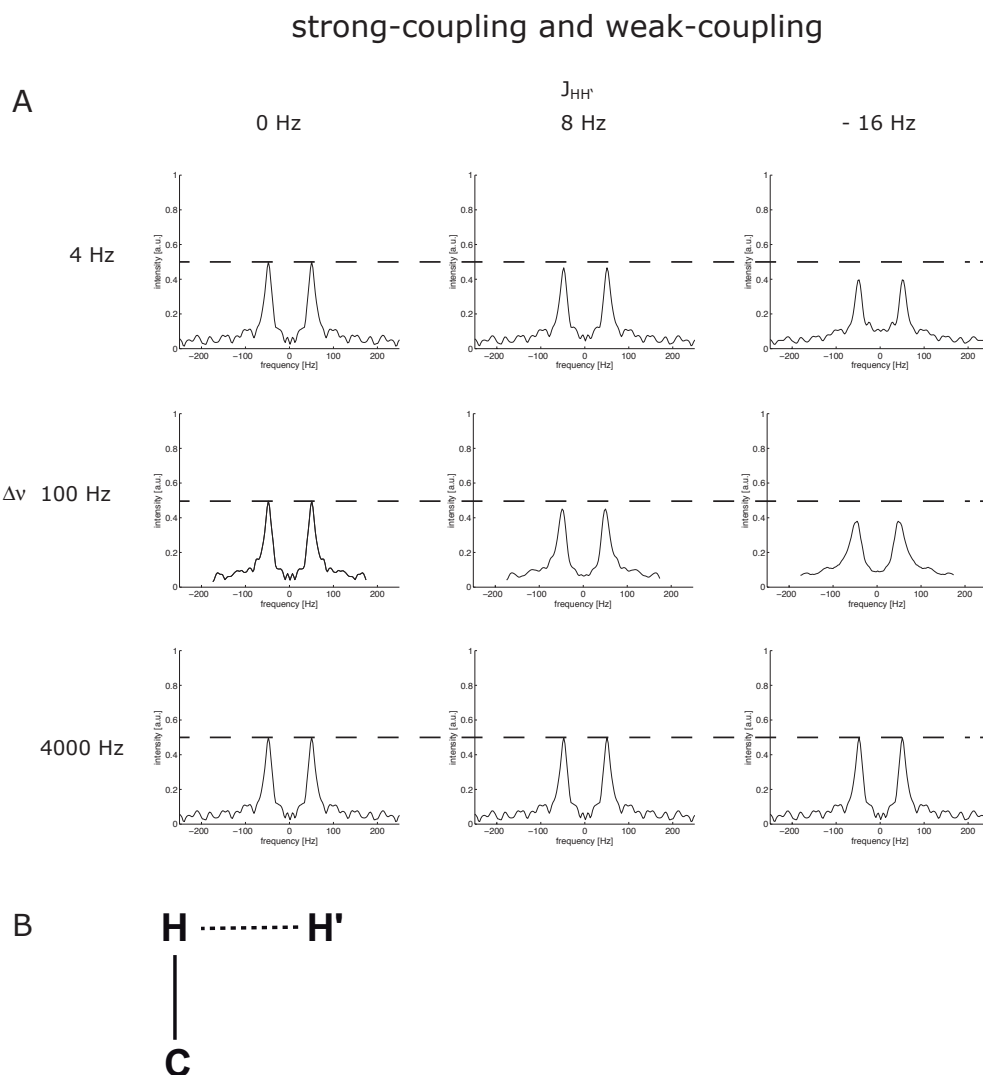


Figure 3.12: Simulated multiplet splitting (A) for linear SHOT decoupling on protons in a CHH' strongly coupled spin system (B) with $J_{CH} = 195$ Hz and $J_{CH'} = 0$ Hz. Spectra are shown for different homonuclear coupling constants $J_{HH'}$ (0 Hz, 8 Hz, -16 Hz) and different chemical shift differences between the two protons $\Delta\nu$ (4 Hz, 4000 Hz), covering both the strong coupling and weak coupling regime; all spectra are referenced to the fully decoupled signal intensity and are shown for one specific decoupler offset giving a scaling factor $\lambda = 0.5$.

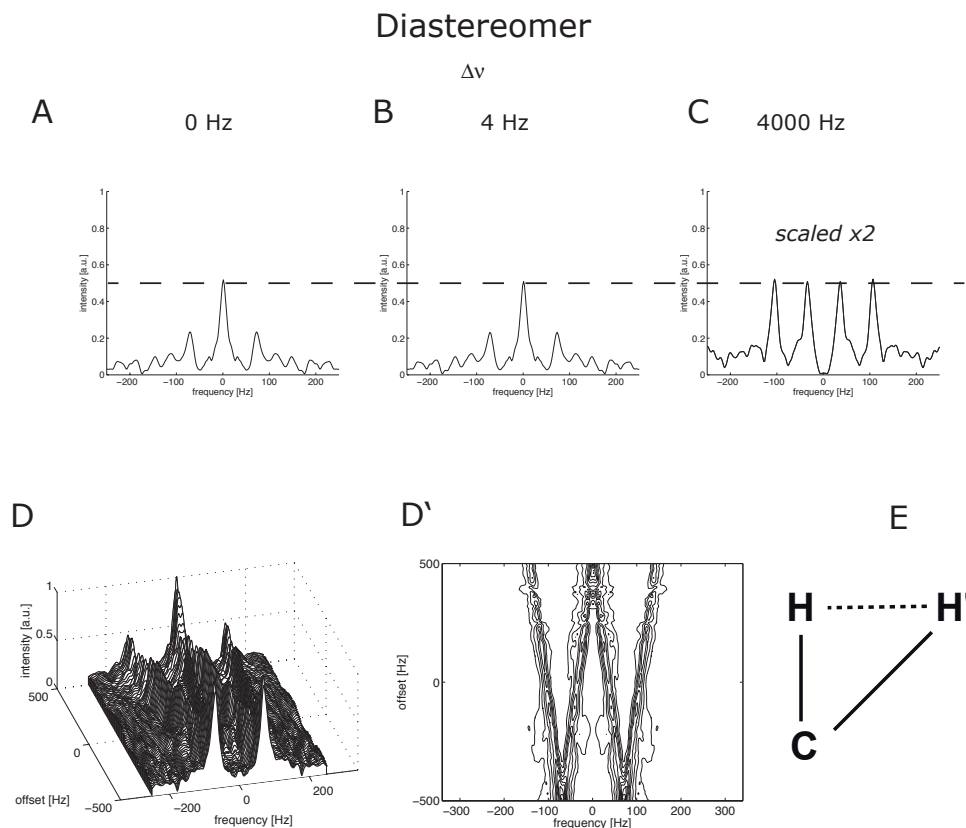


Figure 3.13: Simulated multiplet splitting for linear SHOT decoupling on protons in a diastereomeric spin system (E) with $J_{CH} = J_{CH'} = 140$ Hz. Spectra (A,B,C) are shown for a homonuclear coupling constant $J_{HH'} = -16$ Hz and different chemical shift differences between the two protons $\Delta\nu$ (0 Hz, 4 Hz, 4000 Hz), covering both the strong coupling and weak coupling regime; spectra A,B,C are referenced to the fully decoupled signal intensity and spectrum C is additionally scaled by a factor of 2. All spectra are shown for one specific decoupler offset giving a scaling factor $\lambda = 0.5$. In panels A and B, both protons H and H' have similar offsets (relative to the range of ± 500 Hz for SHOT J scaling between 0 and 1) and have approximately the same J scaling of 0.5, resulting in a triplet with intensities 0.25:0.5:0.25. In case C, the offset of H' is well outside the decoupling bandwidth of the SHOT sequence (with a J scaling of approximately 1), resulting in a doublet of doublets (with intensities 0.25:0.25:0.25:0.25) with $J_{CH}^{eff} \approx J_{CH}/2 = 70$ Hz and $J_{CH'}^{eff} \approx J_{CH'} = 140$ Hz. Panel D and D' show simulated multiplet splitting for the case of $\Delta\nu = 4000$ Hz with decoupler offsets in the range $\nu[-700$ Hz, $+700$ Hz] (D: stacked plot; D': contour plot with contour levels of 0.3, 0.4, ..., 0.9, 1.0).

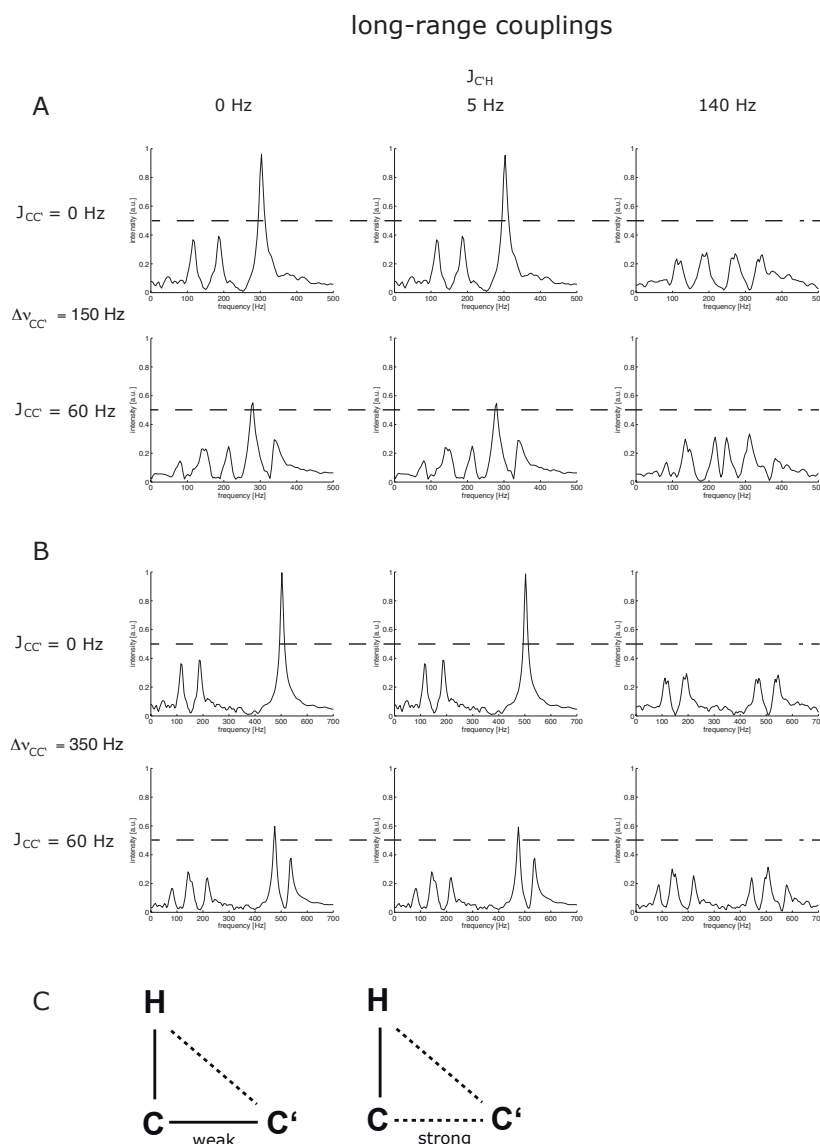


Figure 3.14: Simulated multiplet splitting for linear SHOT decoupling in a HCC' spin system (C) with $J_{CH} = 140$ Hz. Spectra are shown for heteronuclear long-range coupling constants $J_{CH} = 0$ Hz, 5 Hz and 140 Hz and for chemical shift differences between the two carbons $\Delta\nu = 150$ Hz (A) and $\Delta\nu = 350$ Hz (B); spectra are referenced to the ^1H -decoupled maximum signal intensity. All spectra are shown for one specific decoupler offset giving a scaling factor $\lambda = 0.5$. In the top row of Panel A, the scaled J -splittings can be clearly identified as long as no homonuclear coupling is present. In the bottom row of Panel A, identification of peaks is more difficult due to the presence of a 60 Hz homonuclear coupling between the two carbons, which results in a quartett with additional heteronuclear doublet splittings. Still it can be seen in all these cases, that the J -scaling of $\lambda = 0.5$ is conserved. The same situation holds for Panel B, in which the chemical shift between the two carbons is increased to $\Delta\nu = 350$ Hz. Here, identification of peak splittings is becoming easier compared to Panel A, since there is less spectral overlap.

4 Chemical Shift Correlations from Hyperpolarized NMR using a single SHOT

“The real beauty of NMR is that unlike other spectroscopy techniques, with NMR you can see inside bits of matter, including living organisms, without interfering with their chemistry. And with NMR, the information comes directly from the molecules themselves. The disadvantage of NMR is its low sensitivity. NMR interrogates molecules with relatively low-energy radio waves, and raising the signal intensity requires huge, powerful magnets.”

— Alexander Pines (* 1945)

Reprinted from *Analytical Chemistry*, volume 85, pp. 2875-2881 (2013); Guannan Zhang*, Franz Schilling*, Steffen J. Glaser, and Christian Hilty. **Chemical Shift Correlations from Hyperpolarized NMR using a single SHOT**. With permissions from ACS Publications Ltd. Modifications: replacement of Abstract by Summary, addition of Appendices A and B. *contributed equally.

Summary

A significant challenge in realizing the promise of the dissolution dynamic nuclear polarization (DNP) technique for signal enhancement in high-resolution NMR lies in the non-renewability of the hyperpolarized spin state. This property prevents the application of traditional two-dimensional correlation spectroscopy, which relies on regeneration of spin polarization before each successive increment of the indirect dimension. Since correlation spectroscopy is one of the most important approaches

for the identification and structural characterization of molecules by NMR, it is important to find easily applicable methods that circumvent this problem. Here, we introduce the application of scaling of heteronuclear couplings by optimal tracking (SHOT) to achieve this goal. SHOT decoupling pulses have been numerically optimized based on optimal control algorithms to obtain chemical shift correlations in C–H groups, either by acquiring a single one-dimensional ^{13}C spectrum with ^1H off-resonance decoupling, or vice versa. Vanillin, which contains a number of functional groups was used as a test molecule allowing the demonstration of SHOT decoupling tailored towards simplified and accurate data analysis. This strategy was demonstrated for two cases: First, a linear response to chemical shift offset in the correlated dimension was optimized. Second, a pulse with alternating linear responses in the correlated dimension was chosen as a goal, to increase the sensitivity of the decoupling response on the chemical shift offset. In these measurements, error ranges of ± 0.03 ppm for the indirectly determined ^1H chemical shifts, and of ± 0.4 ppm for the indirectly determined ^{13}C chemical shifts were found. In all cases, we show that chemical shift correlations can be obtained from information contained in a single scan, which maximizes the ratio of signal to stochastic noise. Further, a comprehensive discussion of the robustness of the method towards non-ideal conditions is included based on experimental and simulated data. Unique features of this technique include the ability to control the accuracy of chemical shift determination in spectral regions of interest, as well as to acquire such chemical shift correlations rapidly – the latter being of interest for potential application in real-time spectroscopy.

4.1 Introduction

Dissolution Dynamic Nuclear Polarization (DNP) has in recent years gained considerable popularity for enhancing the signal in magnetic resonance experiments by orders of magnitude⁹. Using this technique, nuclear spins of a sample aliquot are hyperpolarized by transfer of polarization from electron spins, at cryogenic temperature. Subsequent dissolution yields liquids containing analytes with a large, non-equilibrium nuclear spin polarization. The gain in signal from this non-equilibrium polarization has the potential to impart significant benefits for the analysis of mass-limited samples of natural or synthetic origin³⁴. Furthermore, the absence of signal averaging reduces the time requirement for obtaining high-quality NMR spectra to the Nyquist limit, pushing the boundary of NMR for the determination of kinetics and intermediate species in chemical reactions¹⁴⁸.

A challenge in the application of dissolution DNP to problems in chemistry lies in the fact that modern NMR techniques for the structural analysis or simply the identification of compounds heavily rely on correlation spectroscopy. In all but the simplest cases, chemical shift correlations between neighboring spins are essential to establish the connectivity of atoms in a molecule. Conventionally, homonuclear or heteronuclear correlations are obtained from two-dimensional (2D) experiments, using chemical shift evolution in an indirect dimension followed by coherence transfer between the two atoms³. The acquisition of a 2D spectrum requires the repetition of the experiment for various evolution times. It is therefore not directly applicable

to a single hyperpolarized sample from dissolution DNP, since in this case the hyperpolarization is lost after application of a single excitation pulse with flip angle $\frac{\pi}{2}$. Several strategies exist to recover information from spin correlations that are applicable to dissolution DNP. True 2D spectroscopy can be carried out using ultrafast, single-scan techniques^{35,37}, or using sequential scanning of the second dimension with small-flip angle excitation¹⁴⁹. A different way of obtaining heteronuclear chemical shift correlations without the need for acquiring a full indirect spectral dimension is through off-resonance decoupling. In off-resonance decoupling, a radio-frequency field is applied at the frequency of one type of nucleus (for example ^1H) during the acquisition of a one-dimensional spectrum of a second type of nucleus (for example ^{13}C). If the decoupling field is of sufficiently low amplitude, an effective residual scalar coupling remains observable for spins that are off-resonance from the decoupling field. From the magnitude of this residual coupling, it is possible to back-calculate the difference in chemical shift between the irradiation frequency and the actual frequency of the coupled spin.

Off-resonance continuous wave (CW) decoupling has been studied since the early days of NMR^{112,114} and has been introduced as a means of obtaining correlation information prior to the advent of 2D-NMR¹²⁴. More recently, it has been used extensively for chemical shift monitoring in pseudo-multidimensional biomolecular NMR experiments, where dimensionality can be increased without the need for the time-consuming process of acquiring an additional dimension^{125,127–130}. Previously, our group proposed the use of off-resonance CW decoupling in conjunction with dissolution DNP.¹³¹ An advantage of the technique in this context is that correlation information can be reconstructed from a small set of spectra. Even though off-resonance CW decoupling does not resolve signal overlap, for small molecules that are often the target of dissolution DNP experiments, this is often not an issue. In CW off-resonance decoupling, the effective scaling of the scalar coupling constant is a non-linear function of frequency offset¹⁴². As a result, the accuracy of the back-calculated chemical shift for any given spin is strongly dependent on the chosen decoupling frequency. In a typical case, acquisition of at least three or four spectra with different decoupling frequencies is required for reliable reconstruction of all chemical shifts in a molecule. Unfortunately, splitting the polarization from a single hyperpolarized sample into multiple spectra results in the acquisition of independent noise in each scan. Additionally, the time required for the acquisition of multiple scans reduces the utility of the method for use in real-time spectroscopy. In remedy of these shortfalls, recently, a method allowing for an arbitrarily chosen offset dependence of the effective coupling constant has been developed¹⁵⁰. Scaling of heteronuclear couplings by optimal tracking (SHOT) refers to the numerical optimization of a decoupling pulse based on optimal control algorithms^{17,23,150}, which is then applied synchronously during the data acquisition to provide a pre-defined offset dependence in the effective coupling constant. This robust approach can take B_1 inhomogeneities into account and can create virtually arbitrary offset profiles of the effective coupling constant. SHOT pulses can thereby overcome limitations that have been imposed to chemical shift encoding via off-resonance CW decoupling, most importantly solving the problems of non-linear chemical-shift dependence of the residual coupling, and the sensitivity towards B_1 miscalibrations. In contrast to band-selective decoupling pulses with a scaling factor of either zero or one in defined

offset ranges^{119–123}, SHOT pulses are entirely optimized *de novo* and give the experimentalist the opportunity to tailor the decoupling offset-profiles to the specific needs of the molecule under investigation. Here, we demonstrate that off-resonance decoupling with such tailored pulses provides significant advantages for the rapid, accurate and sensitive detection of chemical shift correlations by dissolution DNP.

4.2 Experimental Section

SHOT pulses were optimized to cover the chemical shift range and J-coupling values of the vanillin molecule. For covering all coupled spins, a decoupling bandwidth $BW = 2500$ Hz is needed for protons, and $BW = 15000$ Hz for carbons. Optimizations of the pulses were performed with a MATLAB script (The Mathworks, Natick, MA), which is available from the authors upon request. The goal of each optimization is to trace the scaling of the J-coupling constant chosen for the optimization J_{opt} over a range of offset frequencies, and match it to a well-defined target profile $J_{SHOT}(\nu)$ ¹⁵⁰. The desired profile functions were discretized by a number of Z offset frequencies separated by BW/Z between two offset points for the optimization algorithm. In all cases, optimization was carried out using an assumed value of the heteronuclear coupling constant $J_{opt} = 160$ Hz in the absence of off-resonance decoupling. This value corresponds to an approximate average of coupling constants observed in vanillin, which range from 145 Hz (methoxy group) to 174 Hz (aldehyde group). Pulses were designed to be robust to miscalibrations in RF amplitude ($\gamma B_1/(2\pi)$) of ± 2 %. Further, we assumed an effective relaxation rate constant $\kappa = 18.8$ s⁻¹, corresponding to an experimental linewidth of 6 Hz. The resulting SHOT pulses, which were synchronized with receiver sampling, were digitized by $N \cdot M$ pairs of values for amplitude and phase. Here, N corresponds to the number of acquisition points in the pulse optimization, and M corresponds to the number of amplitude and phase modulations between two successive acquisition points. A library of the SHOT pulses used in this work has been made available for download¹⁵¹. Details about implementation of SHOT pulses on the spectrometer can be found in Appendix A.

For proton decoupling, pulses with a linear offset dependence of residual coupling constant,

$$J_{SHOT}(\nu) = J_{opt} \cdot \frac{\nu + \nu_{max}}{2\nu_{max}}, \quad (4.1)$$

and a profile consisting of three linear segments of successively reversed direction (“zigzag profile“),

$$J_{SHOT}(\nu) = \begin{cases} J_{opt} \cdot \frac{\nu + \nu_{max}}{800 \text{ Hz}} & -\nu_{max} < \nu \leq -450 \text{ Hz} \\ J_{opt} \cdot \left(1 - \frac{\nu + 425 \text{ Hz}}{800 \text{ Hz}}\right) & -425 \text{ Hz} < \nu \leq 375 \text{ Hz} \\ J_{opt} \cdot \frac{\nu - 400 \text{ Hz}}{800 \text{ Hz}} & 400 \text{ Hz} < \nu \leq \nu_{max} \end{cases}, \quad (4.2)$$

were calculated. The maximum positive or negative frequency offset from the transmitter frequency ν , for which both of the pulses are valid, is $\nu_{max} = BW/2 = 1250$ Hz. For the zigzag profile, there is a 25 Hz break between two piecewise defined regions

originating from the finite offset-discretization, which was set to $Z = 101$ for both pulses. Additional parameters were $N = 128$ and $M = 10$. The maximum RF amplitude for the linear pulse and zigzag pulse are $(\gamma/(2\pi))B_{1,max} = 1.64$ kHz and $(\gamma/(2\pi))B_{1,max} = 1.96$ kHz. For carbon SHOT decoupling, a linear offset profile according to Equation 4.1 was chosen with $\nu_{max} = BW/2 = 7500$ Hz. Additional parameters were $Z = 301$, $N = 1024$ and $M = 10$. The pulse amplitude is $(\gamma/(2\pi))B_{1,max} = 3.51$ kHz. The amplitude and phase pattern for both of the proton and carbon decoupling pulses are shown in Figure 4.1. In all cases, a total acquisition time $T = 256$ ms is used.

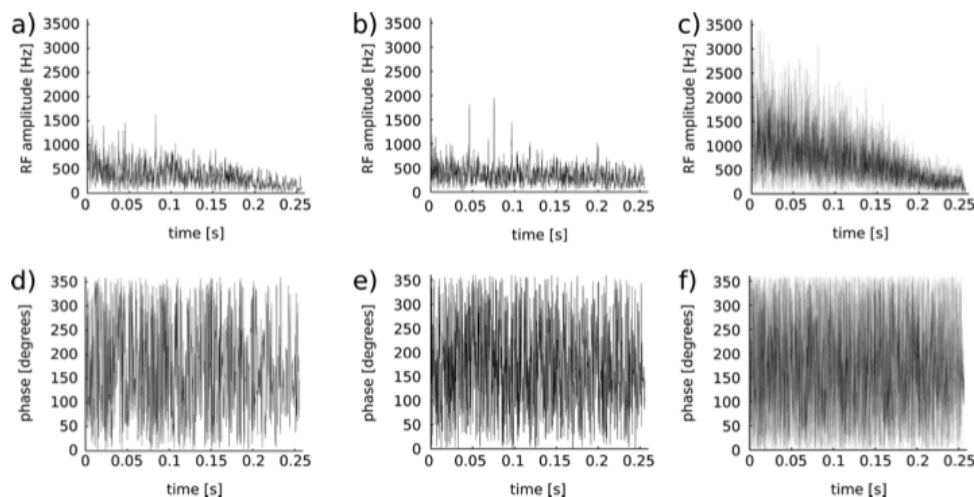


Figure 4.1: Pulse amplitudes for a) linear proton decoupling pulse, b) zigzag proton decoupling pulse, c) linear carbon decoupling pulse. d), e), f) are the pulse phases for the pulses in a), b) and c), respectively.

The SHOT pulses yielded simulated frequency profiles that closely match the pre-defined functions in Equations 4.1 and 4.2 (Figure 4.2). Based on these profiles, the effective coupling constant under SHOT decoupling, J_{SHOT} , varies linearly (or in the case of the zigzag pulse, segmentally linearly) with offset. Further, experimental decoupling profiles were measured by conventional (*i.e.* not hyperpolarized) NMR, using a concentrated sample of vanillin and stepping through different transmitter frequency offset settings. Figures 4.2 b and d compares these experimental data points with curves drawn from the original equations. Both for the linear and zigzag pattern, the experimentally determined points are in good agreement with the theoretical curve despite the fact that the actual coupling constant for the C–H group, which is 174 Hz, is 14 Hz larger than the assumed coupling constant $J_{opt} = 160$ Hz.

Even though these pulses have been optimized for the vanillin molecule, the only specific information used was 1) the J -coupling constant J_{opt} , which should be chosen in the range of the actual J -couplings for reduction of sidebands, 2) the transmitter frequency range which was matched to the proton/carbon chemical shifts, and 3) the off-resonance dependent decoupling pattern, which can be chosen arbitrarily.

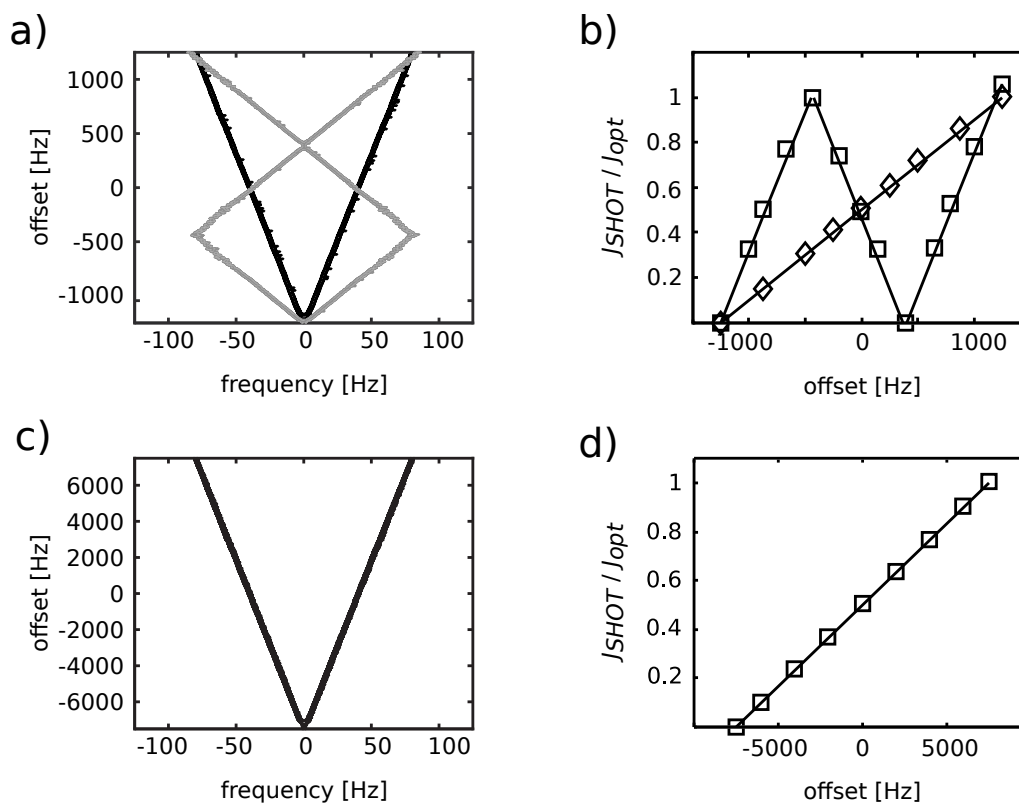


Figure 4.2: a) Contour plot showing the simulated off-resonance coupling pattern of the zigzag (grey lines) and linear (black lines) SHOT pulse for ^1H decoupling as a function of the transmitter offset frequency, calculated for 501 offsets within the bandwidth and applying a zero-filling factor of 10. Contour levels are shown for 95 % of the maximum peak amplitude in the 1D spectrum for each offset. b) ^1H off-resonance pattern functions determined from Equations 4.1 and 4.2 (solid lines), and measured using non-hyperpolarized NMR from the aldehyde group, which shows an actual coupling constant of 174 Hz. c) Simulation of the ^{13}C off-resonance decoupling profile, as in (a) but calculated for 1001 offsets. d) linear off-resonance pattern function as in (b), but for ^{13}C decoupling.

4.2.1 Dynamic Nuclear Polarization and NMR Spectroscopy

The DNP experiment requires selection of two solvents; the glass forming solvent for DNP in the solid state, and the dissolution solvent for transferring the frozen sample into the preinstalled NMR tube. A DMSO/water mixture was chosen for the glass forming solvent in order to avoid peak overlap with the ^{13}C spectrum of vanillin. For the dissolution, the low-viscosity solvent acetonitrile was used to facilitate sample injection. Samples for hyperpolarization consisted of 10 mL of 2 M vanillin dissolved in 72 % DMSO and 28 % H_2O for ^{13}C experiments, or 72 % DMSO- d_6 and 28 % D_2O for ^1H experiments. All samples contained 15 mM tris[8-carboxy-2,2,6,6-tetra[2-(1-hydroxymethyl)]-benzo(1,2-d:4,5-d')bis(1,3)dithiole-4-yl]methyl free radical sodium salt (OX63; Oxford Instruments, Tubney Woods, U.K.) for ^{13}C experiments, or 4-hydroxy-2,2,6,6-tetramethyl-piperidine-1-oxyl (TEMPO) free radical (Sigma-Aldrich, St. Louis, MO) for ^1H experiments. Samples were hyperpolarized on ^{13}C in a HyperSense DNP polarizer (Oxford Instruments) by irradiating with 60 mW power at a frequency of 93.974 GHz ($\omega_e - \omega_N$) for 3 hours at a temperature of 1.4 K. Hyperpolarization on ^1H was carried out using a frequency of 94.005 GHz ($\omega_e - \omega_N$), power of 100 mW, and irradiation time of 30 min. The hyperpolarized samples were dissolved in preheated acetonitrile and transferred to a 5 mm NMR tube installed in a 400 MHz NMR spectrometer with modified broadband observe (BBO) probe (Bruker Biospin, Billerica, MA), using a rapid sample injection device described elsewhere¹⁵². Pressurized nitrogen gas of 17.2 and 10.3 bar for forward and backward pressure, respectively, was applied during sample injection. The total time elapsed from the beginning of the injection to the start of the NMR measurement (excluding time for loading sample loop) was 770 ms for the ^{13}C detected experiments, and 1.85 s for the ^1H detected experiments.

The pulse sequences used for acquisition of off-resonance decoupled spectra have been described previously (see also Appendix A)¹³¹. A reference scan and a SHOT decoupled spectrum were acquired from each hyperpolarized sample, using variable small flip-angle excitation¹⁴⁹. During acquisition of the second scan, a SHOT decoupling pulse (parameters see above) was applied. For the ^{13}C detected experiment, the free induction decay was digitized with 12800 complex points ($10\times$ the number of digitization points in the SHOT pulse). The transmitter frequency offset from 0 ppm was 2670.23 Hz for ^1H decoupling channel. A conventional ^1H spectrum was obtained immediately after each hyperpolarized ^{13}C experiment in order to verify the actual proton chemical shifts under the same experimental conditions. For the ^1H detected experiment, a filter element was applied to remove unwanted signal from spins not coupled to ^{13}C . The number of complex points in the free induction decay was 10240, and the transmitter frequency offset from 0 ppm was 13134.02 Hz for the ^{13}C decoupling channel. Chemical shifts of ^1H of both the hyperpolarized and conventional experiments were referenced to the solvent resonance of acetonitrile. The chemical shift of acetonitrile was calibrated to tetramethyl silane (TMS) at 0 ppm using the substitution method. Chemical shifts of ^{13}C were indirectly calibrated *via* the known ^1H calibration, using¹⁵³ $\gamma_{\text{C}}/\gamma_{\text{H}} = 0.25145020$. Since this frequency ratio is based on a different solvent, we expect a small offset from the actual carbon chemical shift. This offset is however identical for decoupled and undecoupled

experiments, so does not introduce an error for the comparisons.

4.3 Results and Discussion

The performance of SHOT pulses for obtaining chemical shift correlations from hyperpolarized samples both by proton and carbon off-resonance decoupling was evaluated using model samples of approximately 0.3 mM vanillin, with natural (1.1 %) abundance of ^{13}C . Vanillin contains a number of diverse functional groups with different chemical shifts and coupling constants. Additionally, the choice of vanillin for these experiments permits the direct comparison of results with CW off-resonance decoupling¹³¹.

Spectra obtained with each of the three decoupling pulses are shown in Figure 4.3. Comparing the SHOT decoupled upper trace with the undecoupled lower trace in each panel confirms that the coupling constant is reduced by different amounts for each peak. Despite acquisition of the decoupled spectra as the second scan, the height of some peaks is larger in the ^1H SHOT decoupled spectra than in undecoupled spectra due to serendipitous removal of long-range ^1H - ^{13}C couplings. This feature further enhances the ratio of signal to stochastic noise in the SHOT decoupled experiment.

Since the linear SHOT pulses for proton or carbon decoupling cover the full frequency range of coupled proton or carbon spins, all heteronuclear chemical shift correlations can be unambiguously backcalculated from a single one-dimensional spectrum with SHOT decoupling (Equation 4.1). In the case of the zigzag pulse for proton decoupling, chemical shifts can also be calculated from a single spectrum, as long as it is known which of the three intervals a chemical shift falls into. This knowledge may for example be inferred from the known carbon chemical shift, or it may be given if observing chemical shift changes in known compounds. The zigzag SHOT pulse provides the advantage that the slope $\frac{\Delta J_{SHOT}}{\Delta\nu}$ is larger than in the case of the linear pulse, hence theoretically resulting a higher sensitivity of the determined chemical shift with respect to the measured coupling constant.

In an expanded view of the obtained peaks (Figures 4.3 and 4.6 in Appendix B), the residual coupling constants J_{SHOT} can readily be measured. Chemical shift correlations can thus be obtained from either a ^{13}C or from a ^1H detected experiment. Which one of those options is more favorable will be dependent on the individual problem. ^{13}C hyperpolarization and detection offers the advantage of a large chemical shift dispersion, which helps reduce signal overlap. In fact, in the proton detected spectrum, peaks 5 and 7 partially overlap, and in addition peak 5 is split into a doublet due to long-range proton-proton coupling. This overlap introduces more error in the calculation of the carbon chemical shift for atom 7. Carbon detection can also be favorable because ^{13}C nuclei often show relatively long spin-lattice relaxation times, which aids in the preservation of hyperpolarization. On the other hand, largest absolute signal may be obtained from ^1H due to its near 100 % natural abundance and large gyromagnetic ratio.

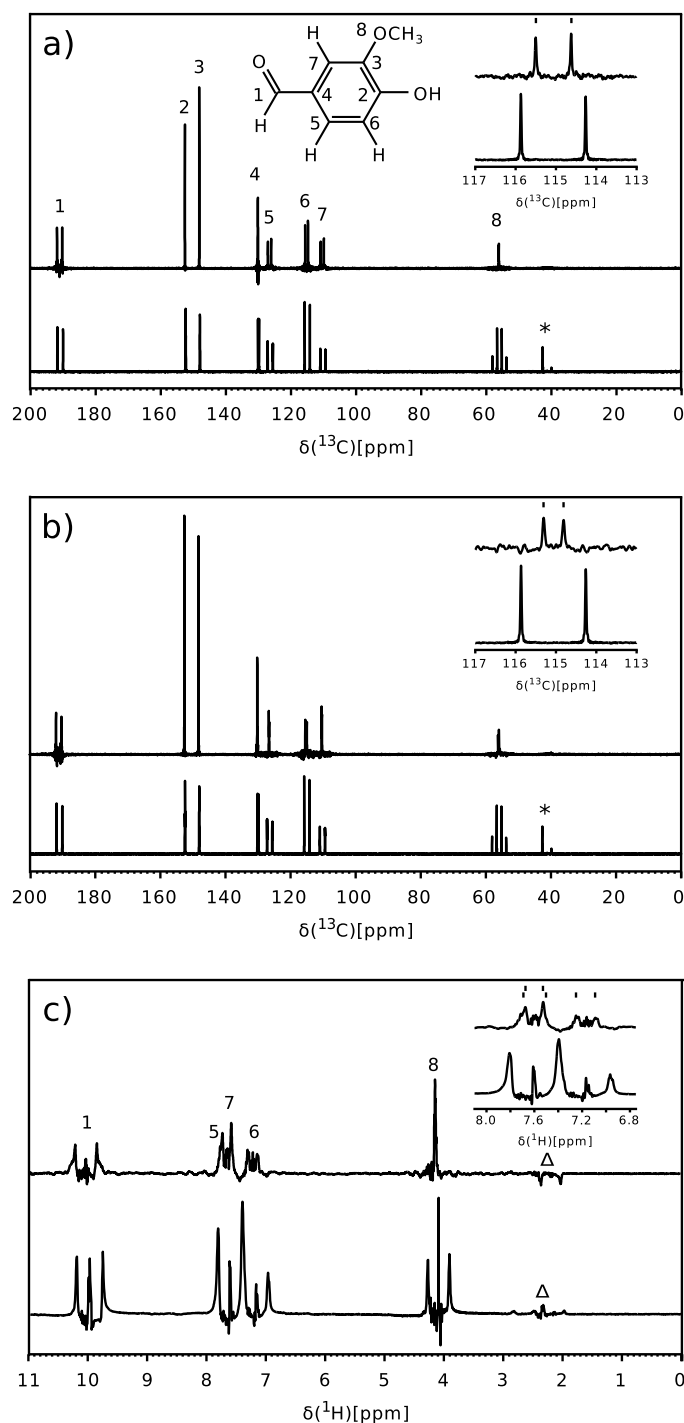


Figure 4.3: a) Spectrum of ^{13}C hyperpolarized vanillin with ^1H SHOT decoupling using the pulse with linear profile (top), and reference spectrum without decoupling (bottom). Decoupled and reference spectrum were acquired from a single hyperpolarized sample. b) Spectra as in (a), but acquired with zigzag SHOT pulse. c) Spectrum of ^1H hyperpolarized vanillin with ^{13}C SHOT decoupling. In all data sets, bottom spectra were acquired first using $\frac{\pi}{4}$ excitation pulse, followed by top spectra with $\frac{\pi}{2}$ pulse. * designates resonances from partially suppressed solvent peak DMSO in (a) and (b), Δ designates resonances from unsuppressed dissolution solvent peak acetonitrile. Three panels of the expanded views for peak 6 corresponding to (a), (b) and peaks 5,7,6 corresponding to (c) are shown.

Chemical shifts were calculated from the spectra in Figure 4.3 for all peaks as $10^6 \cdot (\nu_{trans} + \nu) / \nu_0$, where ν_0 the frequency corresponding to 0 ppm on the decoupling channel, ν_{trans} is the decoupler offset from ν_0 , and ν is derived from Equations 4.1 and 4.2 (see Tables 4.1 and 4.2 in Appendix B). For the calculation, it was assumed that the actual coupling constant for each spin pair is $J_{opt} = 160$ Hz. In order to evaluate the accuracy of this method, it may be most useful to compare the backcalculated chemical shifts to the actual chemical shifts obtained from a ^1H (^{13}C) or ^{13}C (^1H) spectrum of a vanillin sample under similar conditions. Figure 4.4 contains plots that show this error both as a function of frequency offset from the SHOT irradiation frequency, and deviation in the coupling constant from the average coupling of 160 Hz. It is apparent that the error of the calculated chemical shift is within ± 0.03 ppm for indirectly determined ^1H chemical shifts, and within ± 0.4 ppm for indirectly determined ^{13}C chemical shifts. Since the accuracy of the backcalculated chemical shift depends on the slope of the offset function pattern, use of the zigzag pulse is potentially advantageous. When comparing the spread of chemical shift errors $\Delta\delta$ of the two pulses, the zigzag SHOT does appear to give overall smaller error than the linear SHOT. From the data in Figure 4.4, no conclusive correlation between the chemical shift error and absolute chemical shift or deviation of actual from assumed coupling constant can be identified; SHOT pulses appear to perform relatively uniformly over these parameter ranges.

In contrast, CW off-resonance decoupling suffers increased inaccuracy for large offsets, where the effective coupling constant asymptotically approaches the true coupling constant. Using CW decoupling, the acquisition of spectra with decoupling at up to four different chemical shift offsets plus one reference spectrum are required¹³¹. The ratio of the signal to the stochastic noise floor is reduced by 5-fold (not considering relaxation losses). In the SHOT experiment, the linear dependence of $J_{SHOT}(\nu)$ on offset allows for simplified backcalculation of chemical shifts, while requiring the distribution of hyperpolarized magnetization into fewer scans. If coupling constants in a certain range of the molecule under investigation are scaled to an off-resonance pattern by an optimized SHOT pulse and the range of coupling constants is known, the reference spectra shown in Figure 4.3 are not needed for calculation of chemical shift correlations. A single spectrum with SHOT decoupling is then sufficient for calculation of chemical shift.

In the SHOT decoupled experiments (Figures 4.3 and 4.6 in Appendix B), decoupling sidebands are visible in all cases near the partially decoupled peaks. Such sidebands produced by SHOT decoupling pulses are a systematic noise source and have been previously reported. However, sidebands can be simulated with good accuracy for a given SHOT pulse¹⁵⁰. Since here, the decoupled signal amplitudes are well above the sideband amplitudes, they do not limit the determination of chemical shift correlations. In the ^1H spectra, a further peak is visible in the center of each multiplet due to incomplete suppression of the large signal from protons not coupled to ^{13}C .

The reduction in the signal to systematic noise ratio due to such artifacts is balanced by the reduced amount of loss due to relaxation of later scans in CW off-resonance decoupling or other experiments involving the sequential acquisition of multiple scans. Compared to sequentially acquired 2D spectra obtained from hyperpolarized samples¹⁴⁹, this effect is even more substantial due to the need for a large number of

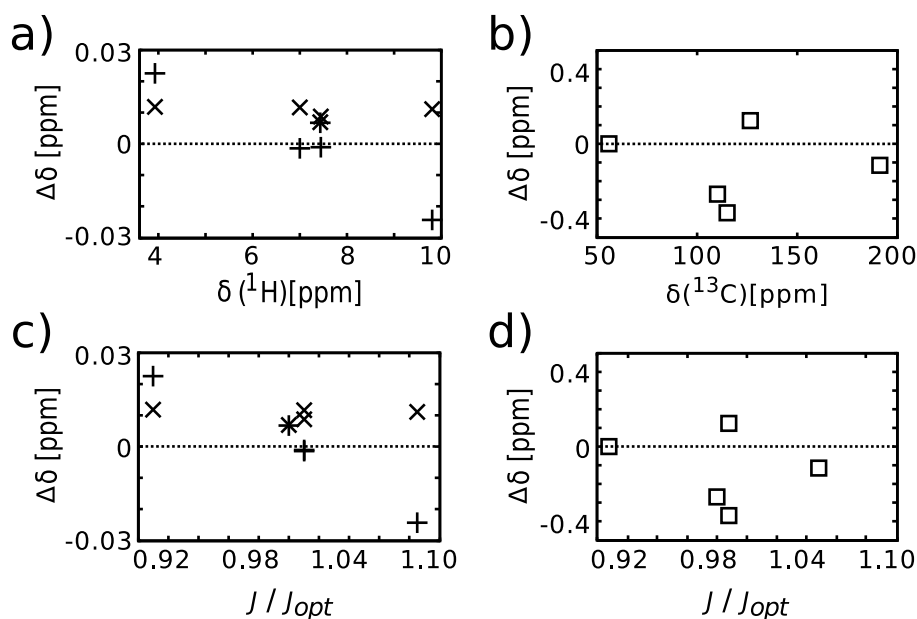


Figure 4.4: a) Chemical shift error $\Delta\delta$ of back calculation from ^{13}C detected experiment with ^1H decoupling using the linear SHOT pulse and the zigzag SHOT pulse, designated by + and \times , and shown as a function of actual chemical shift. b) Chemical shift error of a ^1H detected experiment with ^{13}C decoupling using the linear SHOT pulse. c–d) Data from a–b), but shown as a function of actual coupling constant J over J_{opt} .

points in the indirect dimension (*e.g.* 32) in the 2D spectra. Single-scan ultrafast 2D spectroscopy, where the hyperpolarized magnetization is distributed and read out in separate subvolumes of the sample, does not suffer from this problem, but a noise penalty still has to be paid because of the required increase in receiver bandwidth³⁵. In contrast, SHOT decoupling uses all magnetization in the sample by encoding chemical shift correlations only through the chemical shift dependent scaled splitting of the J -couplings. Off-resonance decoupling in its simplest form (for example, using ^{13}C acquisition) further does not require the application of pulsed field gradients, avoiding the potential for signal loss due to incomplete refocusing³⁸. Even in the case of a carbon filter, only sparing use of pulsed field gradients is made.

In addition to the experimental demonstration of the SHOT decoupling pulses with hyperpolarization, we performed simulations to assess the robustness of the method with respect to various deviations from ideal behavior. Foremost, the SHOT pulses used here have been calculated for an average coupling constant $J_{opt} = 160\text{Hz}$. However, actual ^1H – ^{13}C coupling constants in our test molecule vanillin, and in typical other molecules may range from approximately 145 Hz to 174 Hz. Figure 4.5 compares simulations of offset-dependent decoupling profiles under the assumption of different coupling constants. Figure 4.5 shows an artifact that limits the chemical shift resolution due to truncation of the FID at an acquisition time of 256 ms, yielding a frequency resolution of 3.9 Hz. The resulting step pattern is clearly visible, but the effect can be alleviated by zero-filling with a factor of 10, as applied for the other panels.

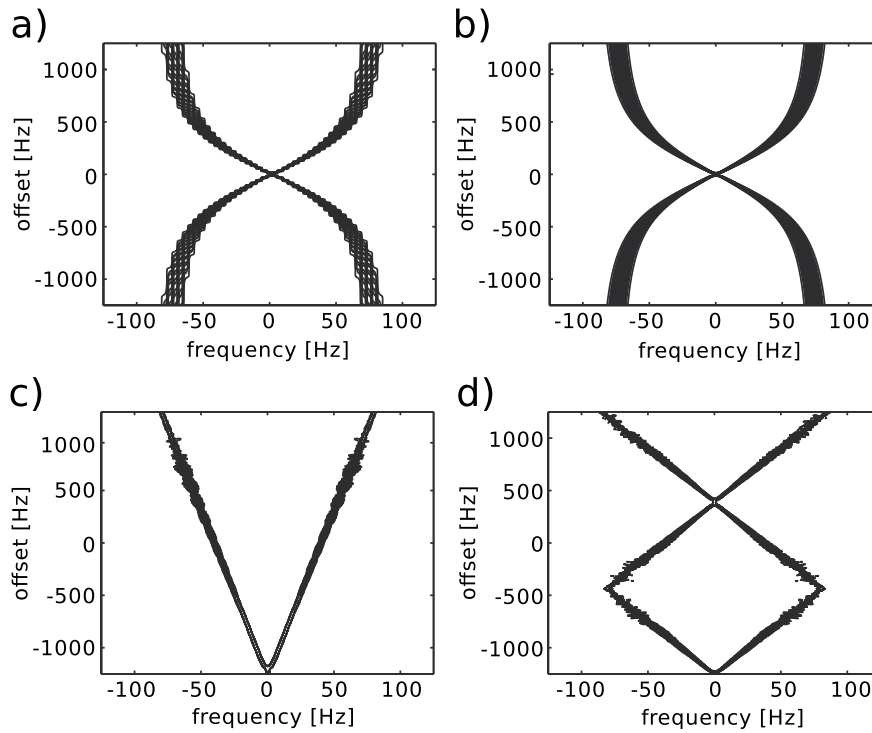


Figure 4.5: Simulation of off-resonance decoupling profiles for a range of actual coupling constants, $J = 145 - 174$ Hz. a) A CW pulse with RF amplitude $(\gamma/(2\pi))B_{1,max} = 0.50$ kHz and a dwell-time of 256 ms/1280. b) A CW pulse as in a, but using a zero-filling factor of 10 for data processing. c) The linear SHOT pulse for protons, with $(\gamma/(2\pi))B_{1,RMS} = 0.43$ kHz and a zero-filling factor of 10. d) The zigzag SHOT pulse for protons, with $(\gamma/(2\pi))B_{1,RMS} = 0.42$ kHz and a zero-filling factor of 10. All contour plots show contour levels at 95% of the maximum peak amplitude in each 1D spectrum and its corresponding offset. Spectra were simulated for 501 offsets in a frequency offset range of 2500 Hz.

In Figures 4.5 a–d, the spread of observed residual coupling constants for spin systems with J in the range between 145 Hz – 174 Hz is compared. It can be seen that CW decoupling (panels a and b) is subject to a larger variation of the residual coupling constant than SHOT decoupling (panels c and d). Comparing Figures 4.5 c and d, the linear SHOT pulse shows the smallest deviations with regard to variations in the actual coupling constant compared to the off-resonance profiles in Figures 4.2 a and b, which were calculated without variations in J . This property of robustness of SHOT decoupling pulses to J -variations implies that the actual coupling constant J does not need to be known for the backcalculation of the chemical shift, as long as it falls within a permissible range. Therefore, the reference scans in Figure 4.3 are in principle not needed, and the experiment can be carried out by recording a single spectrum with SHOT decoupling. The simulations in Figure 4.5 point out and experiments confirm that J -couplings can be either scaled up or down by a SHOT pulse, which is from a theoretical point of view very interesting and currently under further investigation, since so far scaling of J -couplings in the literature was limited to reducing the couplings.

However, a deviation of J from J_{opt} comes at the cost of increased sideband amplitudes. Nevertheless, under the conditions used in Figure 4.5, sidebands do not become larger than the main peaks of the coupled spin. It should further be pointed out that the shown SHOT pulses were so far not specifically optimized for robustness with regards to J -variation, which would slow down the optimization process significantly. Future improvements of SHOT pulses may be facilitated by more efficient implementation of the optimal control algorithm and parallel computing techniques as well as faster processors. Sidebands might be further decreased by the use of cooperative pulses (COOP) in combination with SHOT decoupling²⁵. COOP pulses are designed to compensate each other’s imperfections in repeated scans.

While off-resonance profiles for CW decoupling are intrinsically not robust with respect to B_1 variations of the decoupling coil, SHOT pulses can be optimized by including an additional cost function, which takes B_1 inhomogeneities into account. All SHOT pulses used here were optimized for B_1 variations of $\pm 2\%$. To show the robustness of SHOT with regard to B_1 imperfections, a representative decoupled spectrum with a residual peak splitting of $J_{SHOT} = J_{opt}/4 = 40$ Hz was simulated for a range of B_1 variations of $\pm 15\%$ (Figure 4.7 in Appendix B). It can be seen that the SHOT pulse does not show a significant change of the peak splitting in the optimized region, and even in the $\pm 15\%$ region shows only slight changes compared to the CW pulse. Based on these simulations, chemical shifts obtained from SHOT decoupled experiments are more robust than CW decoupling towards B_1 inhomogeneities. However, increased robustness comes again at the cost of increased sidebands and lowered peak amplitudes.

Since SHOT pulses are only optimized for a certain offset region, a final question arises as to what happens to the spins outside of the optimized bandwidth. (Figure 4.8 in Appendix B) compares the behavior of the linear SHOT pulse for ^1H decoupling, optimized for 2500 Hz bandwidth, to a CW pulse with $(\gamma/(2\pi))B_1 = 0.5$ kHz over a large bandwidth. Outside of the optimized region, SHOT pulses have a non-defined off-resonance decoupling pattern, while CW decoupling has the known off-resonance pattern. This indicates that when using SHOT decoupling, it is of particular importance to correctly adjust the center frequency and bandwidth of the

pulse.

It is interesting to point out that SHOT pulses achieve the desired offset profile using relatively low RF power. For example, a SHOT pulse that achieves a linear scaling in an offset range of 15 kHz only needs a mean RF amplitude of $(\gamma/(2\pi))B_{1,RMS} = 0.89$ kHz. In order to achieve a similar off-resonance profile using CW decoupling, a RF amplitude in excess of 10 kHz would be required, which is above the CW power limit of most high resolution probeheads. SHOT bandwidths higher than 15 kHz have not been optimized yet and the bandwidth limits are currently under investigation. Low-power SHOT decoupling pulses may further be of interest for hyperpolarized MRI, which is subject to more stringent power limitations than high-resolution NMR.

4.4 Conclusions

In summary, we have presented a method for rapid determination of chemical shift correlations applicable to samples hyperpolarized by dissolution DNP. Chemical shifts are reconstructed from an off-resonance decoupling experiment with optimized SHOT pulses, requiring the acquisition of only a one-dimensional spectrum in a single scan. Correlation spectroscopy based on SHOT off-resonance decoupling therefore makes most efficient use of non-renewable polarization. It circumvents an inherent limitation of the dissolution DNP technique, where noise is introduced with each additional scan into which the originally generated polarization is distributed. SHOT pulses clearly are more complex than most other pulses encountered in traditional NMR experiments. A program has been designed for facile optimization of SHOT pulses yielding specific decoupling profiles and taking B_1 inhomogeneity and power limitations into account. Additionally, due to processor time required for an optimization, pulses are being collected in a library for download and immediate application. Practically, the intricacy in the pulse design translates to a relative simplicity in data analysis. Using a SHOT pulse with a linear decoupling profile, for example, yields residual coupling constants that are proportional to offset from one end of its frequency range. Perhaps more importantly, the decoupling profile of SHOT pulses can be tailored to the specific molecule of interest. This option brings several new applications within reach of this technique. For example, a pulse could be designed to enhance resolution specifically in spectral regions of high signal overlap, such as near the aliphatic and carbonyl resonances in hyperpolarized ^{13}C spectra of peptides. Further, the ability to obtain chemical shift correlations in a single scan may prove beneficial for real-time monitoring of chemical reactions, which requires rapid acquisition of multiple time points.

4.5 Acknowledgements

Financial support from the National Science Foundation (Grant CHE-0846402), and from the Welch Foundation (Grant A-1658) is gratefully acknowledged. F.S. thanks Fonds der Chemischen Industrie, the Faculty Graduate Center Chemistry, TUM Graduate School and the Institute for Advanced Study (IAS) at TUM for financial support. S.J.G. acknowledges support from the DFG (GI 203/6-1) and from Fonds der Chemischen Industrie.

4.6 Appendix A: Pulse sequences and calibration

4.6.1 SHOT Pulse Parameters

The maximum RF amplitude $(\gamma/(2\pi))B_{1,max}$ must be calibrated to the value specified with the pulse. This calibration can be achieved by various means, including measurement of the known off-resonance profile for CW decoupling, measurement of the Bloch-Siegert shift, or determination of the duration for a π -pulse, the latter being the least accurate method. The duration of data acquisition and SHOT pulse must be equal, and acquisition points $N_{acq} = i \cdot M \cdot N$ are integer multiples i of the number of digitization points of the pulse. Even though a SHOT pulse is initially calculated for a specific set of parameters, the maximum RF field $B_{1,max}$, the bandwidth BW , the acquisition time T , and the optimized scalar coupling constant J_{opt} can be rescaled according to the relation $\gamma B_{1,max} \propto BW \propto J_{opt} \propto T^{-1}$.

The average power for SHOT pulses is useful to calculate for comparison to other decoupling sequences or RF power limits. Using the definition for root mean square (RMS) amplitude

$$B_{1,RMS} = \sqrt{\frac{\sum_{i=1}^{N \cdot M} (B_{1,i})^2}{N \cdot M}}, \quad (4.3)$$

the linear and zigzag SHOT pulses for ^1H decoupling yield $(\gamma/(2\pi))B_{1,RMS} = 0.43$ kHz and $(\gamma/(2\pi))B_{1,RMS} = 0.42$ kHz, respectively. For the ^{13}C pulse, $(\gamma/(2\pi))B_{1,RMS} = 0.89$ kHz.

4.6.2 NMR Pulse Sequences

The pulse sequence for ^{13}C detected hyperpolarized experiments consisted of elements [(p1 - g1)₃ - pe - acq - g2], and was repeated two times on a single hyperpolarized sample to measure a SHOT decoupled spectrum and an undecoupled spectrum. p1 is a selective $\frac{\pi}{2}$ pulse on the ^{13}C channel (EBURP shape, 10 ms duration), applied at the solvent resonance of DMSO (40.17 ppm). g1 (40.6 G/cm, 42.0 G/cm, 97.2 G/cm, 1 ms) is a pulsed field gradient applied along x, y and z axes to de-phase the coherences from the solvent signal. pe is a hard ^{13}C excitation pulse $(\gamma/(2\pi))B_1 = 29.41$ kHz) applied with a flip-angle of $\frac{\pi}{4}$ in the first scan, and $\frac{\pi}{2}$ in the second scan in order to equally distribute signal. Here, the flip angle is not compensated for relaxation, because spin lattice relaxation in vallin ($T_1 \sim 6$ s) is not significant during the experimental time. g2 (50 G/cm, 2.5 ms) is another pulsed field gradient applied along the z axis to remove the unwanted coherence from the previous acquisition.

The pulse sequence for the ^1H detected experiment included additionally a filter element to remove ^1H coherence from atoms not coupled to ^{13}C . It consists of [pe - τ_1 - p1 - τ_2 - p2/p3 - g1/ τ_2 - p1 - g2/ τ_1 - acq - g3]. Parameters are similar to the ^{13}C detected experiments described above. The hard ^1H excitation pulse pe (small flip angle, see above) was applied with a field strength of

$(\gamma/(2\pi))B_1 = 22.22$ kHz. p1 is a 90 degree hard pulse $((\gamma/(2\pi))B_1 = 29.41$ kHz) applied on ^{13}C . p2 $((\gamma/(2\pi))B_1 = 11.11$ kHz) and p3 $((\gamma/(2\pi))B_1 = 14.71$ kHz) are 180 degree hard pulses applied simultaneously on the ^1H and ^{13}C channels for chemical shift refocusing. Pulses p2 and p3 have a phase difference of $\frac{\pi}{2}$ compared to p1 and the first p1 pulse. The second p1 pulse has a phase difference of π compared to the first p1 pulse. The time delay for the heteronuclear filter is $\tau_1 = 1/(2J) = 3.57$ ms. The pulsed field gradients for coherence selection are g1 (40.6 G/cm, 42.0 G/cm, 97.2 G/cm, 1 ms) and g2 (-30.5 G/cm, -31.4 G/cm, -74.3 G/cm, 1 ms), applied along x , y , and z axes. τ_2 is a short time delay for stabilization after pulsed field gradients.

4.7 Appendix B: Figures and Tables

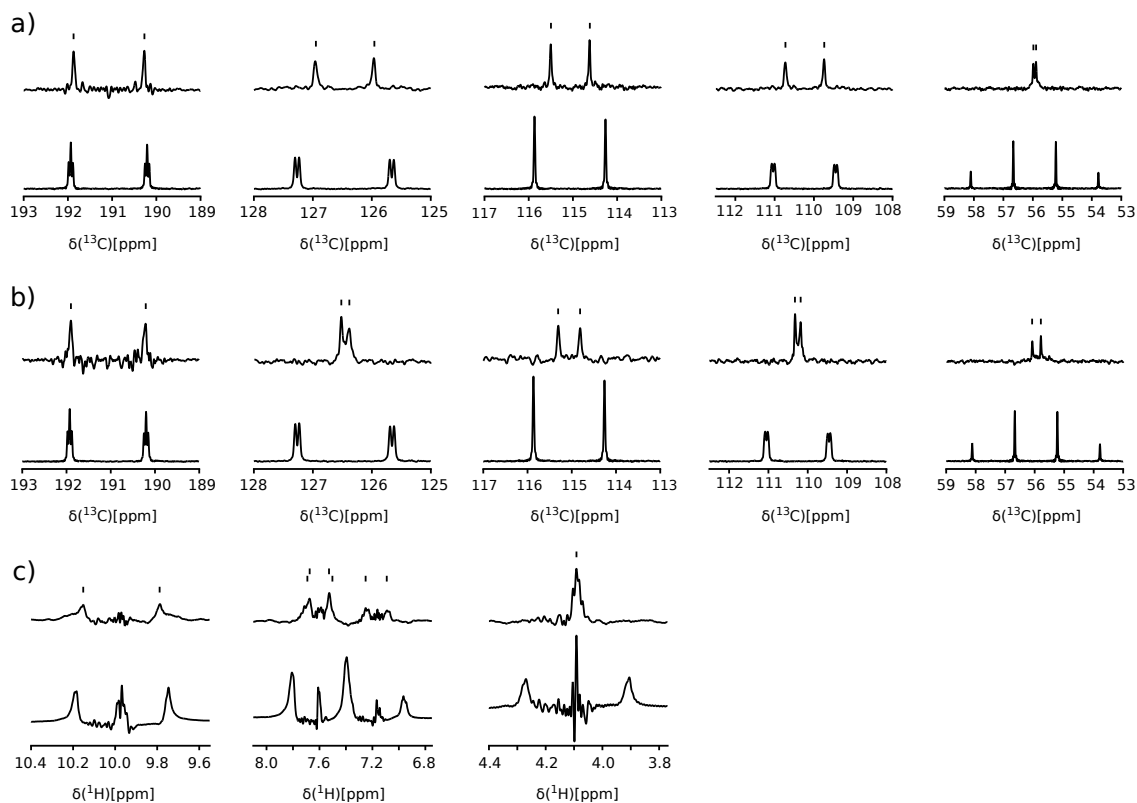


Figure 4.6: Expanded view of peaks obtained from SHOT decoupling experiments with SHOT decoupled upper trace and undecoupled lower trace in each panel. a) ^{13}C detected experiment with ^1H decoupling using linear SHOT pulse. b) ^{13}C detected experiment with ^1H decoupling using zigzag pulse. In a and b, the different spectra represent atoms number 1,5,6,7 and 8 from left to right. c) ^1H detected experiment with ^{13}C decoupling. Spectra represent atoms number 1(left),5,7, and 6 (middle) and 8 (right) from left to right. Marks above peaks indicate the positions used for calculation of residual coupling constants J_{SHOT} . In case of splitting by ^1H - ^1H coupling, the better resolved of the two multiplet peaks was used.

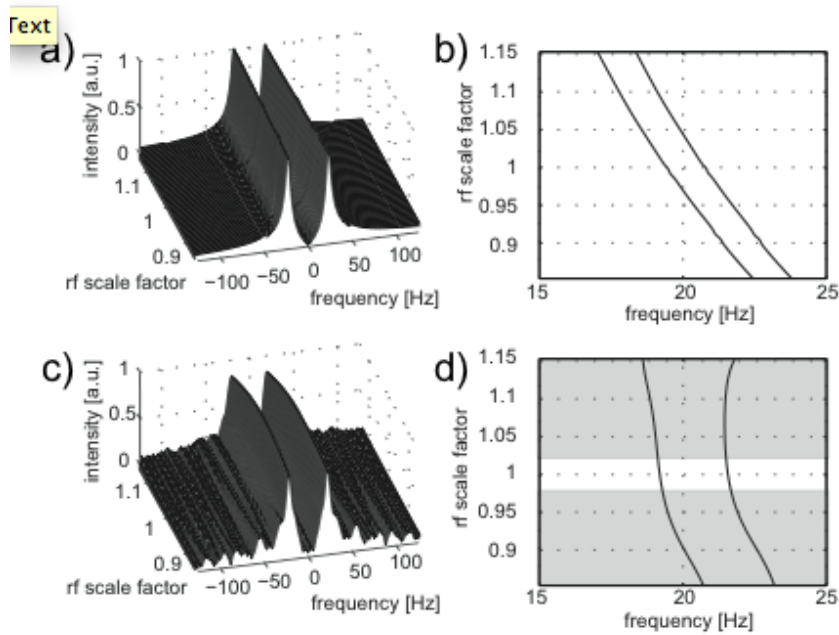


Figure 4.7: Simulations of B_1 variations in a range of $\pm 15\%$ for spectra with 40 Hz peak splitting at unscaled B_1 showing both CW decoupling (a and b) and linear ^1H SHOT decoupling (c and d). Contour plots show contour lines at 95 % of the maximum peak amplitude from a single coupled peak. The region which was not optimized for B_1 miscalibrations is underlayed in gray texture for the linear SHOT pulse.

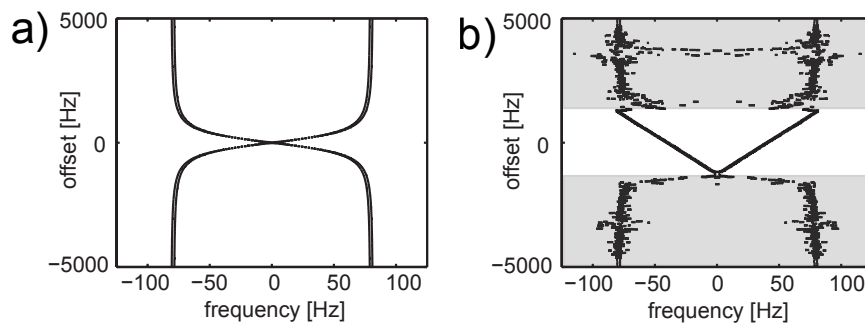


Figure 4.8: Wide-bandwidth simulations of a) CW off-resonance decoupling with $(\gamma/(2\pi))B_1 = 0.5$ kHz, and b) the linear SHOT pulse for ^1H decoupling. The region over which the linear SHOT pulse was not optimized for is underlayed in gray texture.

Table 4.1: Proton chemical shift calculation using linear and zigzag SHOT with ^{13}C detection

^{13}C group	$\delta^1\text{H}(ppm)$	Linear SHOT			Zigzag SHOT		
		J_{SHOT}/J_{opt}	$\delta^1\text{H}_{linear}(ppm)$	$\Delta\delta(ppm)$	J_{SHOT}/J_{opt}	$\delta^1\text{H}_{zigzag}(ppm)$	$\Delta\delta(ppm)$
1	9.809	1.01	9.833	-0.024	1.06	9.798	0.011
5	7.448	0.62	7.449	-0.001	0.08	7.440	0.008
6	7.000	0.55	7.001	-0.001	0.31	6.988	0.012
7	7.436	0.62	7.429	0.007	0.09	7.429	0.007
8	3.931	0.06	3.909	0.022	0.18	3.920	0.011

Table 4.2: Carbon chemical shift calculation using linear SHOT with ^1H detection

^1H group	$\delta^{13}\text{C}(ppm)$	J_{SHOT}/J_{opt}	$\delta^{13}\text{C}_{linear}(ppm)$	$\Delta\delta(ppm)$
1	191.37	0.91	191.49	-0.12
5	126.70	0.47	126.58	0.12
6	115.17	0.40	115.54	-0.37
7	110.31	0.37	110.58	-0.27
8	56.00	0.00	56.00	0.00

5 Diffusion of hyperpolarized ^{13}C -metabolites in tumor cell spheroids using real-time NMR spectroscopy

“Science is grounded in evidence and consistency, but scientific insights are always creative acts. We are always looking for a new direction to explore or a new experimental trick for encouraging nature to reveal herself.”

— Sir Paul Terence Callaghan (* 1947; † 2012)

Reprinted from *NMR in Biomedicine*, volume 26, pp. 557-568 (2013); Franz Schilling, Stephan Düwel, Ulrich Köllisch, Markus Durst, Rolf F. Schulte, Steffen J. Glaser, Axel Haase, Angela M. Otto, and Marion I. Menzel. **Diffusion of hyperpolarized ^{13}C -metabolites in tumor cell spheroids using real-time NMR spectroscopy**. With permissions from John Wiley & Sons, Ltd. Modifications: replacement of Abstract by Summary, addition of Appendices A and B.

Summary

The detection of tumors non-invasively, the characterization of their progression by defined markers, and the monitoring of response-to-treatment are goals of medical imaging techniques. Here, a method which measures apparent diffusion coefficients (ADCs) of metabolites using hyperpolarized ^{13}C diffusion-weighted spectroscopy is presented. A pulse sequence based on the pulsed gradient spin echo (PGSE) was developed that encodes both kinetics and diffusion information. In experiments with MCF-7 human breast cancer cells, we detected an ADC of intracellularly produced lactate of $(1.06 \pm 0.15) \mu\text{m}^2/\text{ms}$, which is about half of the value measured with

pyruvate in extracellular culture medium. When monitoring tumor cell spheroids during progressive membrane permeabilization with Triton X-100, the ratio of lactate ADC to pyruvate ADC increases as the fraction of dead cells increases. Therefore, ^{13}C ADC detection can yield sensitive information on changes in membrane permeability and subsequent cell death. Our results suggest that both metabolic label exchange, and ^{13}C ADCs can be acquired simultaneously and may potentially serve as non-invasive biomarkers for pathological changes in tumor cells.

5.1 Introduction

Quantifying and understanding tumor metabolism is a central issue in diagnosis and treatment of tumors. Significant progress in this field has been made since the introduction of hyperpolarized ^{13}C metabolic imaging, which enables a $> 10,000$ fold increase in signal-to-noise ratio (SNR) as compared to thermal ^{13}C measurements⁹. Key to understanding both uptake and metabolism of hyperpolarized ^{13}C labeled agents in tumors^{11,154}, such as $[1-^{13}\text{C}]$ pyruvate, is a careful analysis of the observed ^{13}C label exchange kinetics, which involve delivery of pyruvate, membrane transport and intracellular metabolic label exchange into lactate via lactate dehydrogenase (LDH)^{41,155}. Several kinetic models have been proposed^{39,42–44,156–160}, which allow analyzing uptake and metabolism after injection of hyperpolarized $[1-^{13}\text{C}]$ pyruvate. However, one major challenge of all ^{13}C kinetic models is the fact that the ^{13}C signal of each metabolite emanates from both extra- and intracellular compartments, which currently are difficult to separate in typical hyperpolarization experiments. One approach to differentiate metabolite signals from different compartments is via their diffusion behavior, since the diffusion coefficient of metabolites located in different cellular compartments can vary up to 10-fold^{51,52}. There is evidence that the intracellular apparent diffusion coefficient (ADC) is lower than that of extracellular ADC, because diffusion inside the cell is restricted and hindered^{53–55}. In ^1H diffusion MRI, this effect is well established as a diagnostic option for tumor diagnosis, staging, and response-to-treatment in a variety of tumor entities^{161–163}. Consequently, diffusion-weighted ^{13}C spectroscopy may be well suited to differentiate metabolites in different cellular compartments, but it suffers from a low natural abundance of the ^{13}C isotope and a fourfold smaller gyromagnetic ratio compared to ^1H , requiring \sim fourfold stronger magnetic field gradients to encode diffusion¹⁶⁴. Some effort has been made to overcome low SNR of thermally polarized ^{13}C -metabolites in-vivo using indirect detection techniques such as ACED-STEAM¹⁶⁵ in combination with approaches to increase the ^{13}C isotope concentration in-vivo by continuous infusion of ^{13}C -labelled glucose¹⁶⁶. In this study, hyperpolarization⁹ is used to overcome the low SNR limitation of ^{13}C diffusion-spectroscopy. This enabled the determination of ADCs of $[1-^{13}\text{C}]$ pyruvate and $[1-^{13}\text{C}]$ lactate in tumor cell spheroids.

5.2 Methods

5.2.1 Hyperpolarized diffusion-weighted NMR spectroscopy

A diffusion-weighted NMR pulse sequence based on the pulsed gradient spin echo (PGSE) sequence¹¹⁰ was developed for measuring ADCs of hyperpolarized ^{13}C nuclei. It relies on the principle of signal loss through diffusion dependent phase dispersion in the presence of a magnetic field gradient. Diffusion in tumor cell spheroids is restricted and hindered by cellular compartments. Hence, an ADC instead of a pure molecular self-diffusion coefficient is being determined. The non-equilibrium longitudinal magnetization of hyperpolarized nuclei irreversibly decays with the relaxation time constant T_1 , therefore it has to be used efficiently during the pulse sequence. The PGSE sequence was modified to excite spins with a small flip angle ($\alpha = 30^\circ$) (see Fig. 5.1 A). The diffusion time was set to $\Delta = 40$ ms, the gradient time to $\delta = 3.15$ ms, and the gradient amplitudes were varied up to a maximum of $g = 2.0$ T/m for a half-sine gradient pulse along z -direction. We used hard pulses for both excitation and refocusing with a pulse duration of $40 \mu\text{s}$ for a 180° pulse. The repetition time T_R of the sequence was set to 1.5 s with an acquisition time of $T_{acq} = 0.5$ s. The signal equation is given by the Stejskal-Tanner expression modified with an exponential damping term $T_{1,eff}$, which consists of T_1 relaxation and loss of M_z due to repeated excitation:

$$\frac{1}{T_{1,eff}} = \frac{1}{T_1} - \frac{\ln(\cos(\alpha))}{T_R}. \quad (5.1)$$

The gradient amplitude dependent signal I_g is given by:¹⁶⁷

$$I_g(b, t) = I_0 \cdot \exp\left(\frac{-t}{T_{1,eff}}\right) \cdot \exp(-bD) \quad (5.2)$$

$$= I_0 \cdot \exp\left(\frac{-t}{T_{1,eff}}\right) \cdot \exp\left(-(\Delta - \delta/4)(2\gamma g\delta/\pi)^2 D\right), \quad (5.3)$$

where b is the amount of diffusion sensitivity introduced by the magnetic field gradients, also known as b -value. I_0 denotes the initial signal at $t = 0$ s, γ is the gyromagnetic ratio of carbon, and D denotes the ADC. The sequence was repeated for different gradient amplitudes in a loop structure, starting with $b = 0$ $\text{ms}/\mu\text{m}^2$, jumping to a b -value of 2.85 $\text{ms}/\mu\text{m}^2$ (which corresponds to $g = 2$ T/m), and thereafter decreasing the gradient amplitudes linearly in nine steps by a decrement of -0.2 T/m until the gradients were set to zero again. Finally, five acquisitions without gradient diffusion encoding were recorded, so that in total 16 scans were acquired with diffusion encoding during 10 out of 16 excitations (see Fig. 5.1 B). The six scans without diffusion encoding were used to determine relaxation time constants T_1 of different metabolites independently and to estimate the kinetic rate constant for label exchange from pyruvate to lactate. Each ADC measurement was started 20 s after injection of hyperpolarized pyruvate with a reference scan to determine the initial signal amplitudes of pyruvate and pyruvate hydrate. The pulse sequence was

continued first with strong diffusion weightings in order to obtain enough SNR, and then diffusion weighting was gradually reduced, while T_1 relaxation reduced SNR over time. A standard diffusion-weighted spectrum acquired following injection of hyperpolarized $[1-^{13}\text{C}]$ pyruvate into 40×10^6 breast cancer cells is shown in Fig. 5.1 C.

5.2.2 Data analysis

Correct determination of ADCs from pyruvate and its metabolites in general requires adequate kinetic modeling of the metabolites under investigation^{41,44,154,160,168}, since metabolite concentrations vary as a function of time, which would impair accurate determination of the ADC value. Note that this is not the case for pyruvate hydrate because of instantaneous reversible reaction from pyruvate to pyruvate hydrate^{169,170}. Tumor cells received a high concentration of pyruvate, leading to saturation and a signal intensity ~ 40 fold higher than that of lactate. Changes in pyruvate signal due to exchange of the hyperpolarized label from lactate to pyruvate or from pyruvate to lactate was found to have a negligible effect on the signal intensities and was therefore neglected. Metabolite signals below the noise-level, mostly occurring for lactate at high b -values due to the low metabolite concentration, were not included in the further data analysis. ADCs of pyruvate and pyruvate hydrate were modeled by the standard signal equation (c.f. equation 5.3). With the known flip angle decay (c.f. equation 5.1), individual T_1 times were determined by a mono-exponential fit to the pyruvate and pyruvate hydrate signal amplitudes at $b = 0$. Data were then corrected for the effective damping constant $T_{1,eff}$ and plotted on a semi-logarithmic scale, such that the ADC could be determined from the linear time-independent correlation:

$$\ln(I(b)) = \ln(I_0) - bD. \quad (5.4)$$

Lactate signal in viable cells emanates purely from intracellular metabolic label exchange from pyruvate and is modeled on the basis of classical Bloch-McConnell differential equations^{39,42}, assuming a constant pyruvate-to-lactate label exchange with the rate constant $k_{pyr \rightarrow lac}$. The solution of these differential equations based on the respective z -magnetizations of lactate $M_{lac,z}$ and pyruvate $M_{pyr,z}$, with initial conditions $M_{lac,z}(t_0=-20s) = 0$ and $M_{pyr,z}(t_0) = [\text{Pyr}]_0$ is given by³⁹:

$$M_{lac,z}(t) = \frac{[\text{Pyr}]_0 \cdot k_{pyr \rightarrow lac}}{\Delta\rho - k_{pyr \rightarrow lac}} \cdot \exp\left(-\frac{(t+20s)}{T_{1,eff,lac}}\right) \cdot \{-1 + \exp[(t+20s)(\Delta\rho - k_{pyr \rightarrow lac})]\}, \quad (5.5)$$

with $\Delta\rho = (1/T_{1,lac}) - (1/T_{1,pyr})$ being the difference of inverse T_1 times of lactate and pyruvate. To estimate the lactate T_1 at high accuracy with higher SNR than in the diffusion experiment, we obtained it from a separate standard 'pulse-and-acquire' NMR experiment without diffusion weightings, where we followed the signal build-up of lactate over the course of 50 s with TR = 1.5 s and a flip angle of 5° . Two-site exchange kinetic modeling¹⁶⁰ gave a $T_{1,lac}$ of 13.2 s, which is significantly shorter

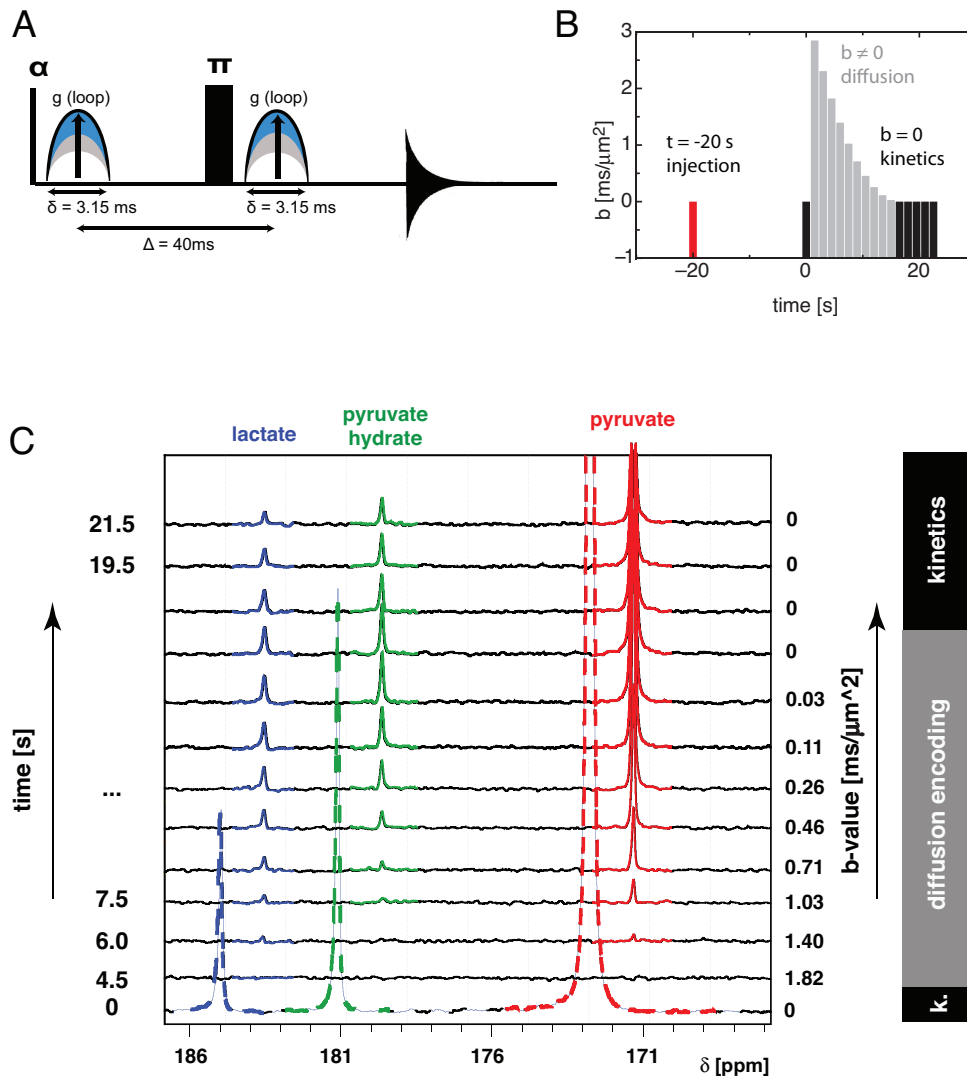


Figure 5.1: NMR sequence for hyperpolarized real-time diffusion-weighted spectroscopy encoding both diffusion and kinetics at the same time. (A) The sequence is a modified pulsed-gradient spin echo sequence (PGSE) with low flip angle excitation ($\alpha = 30^\circ$) and is repeated with $T_R = 1.5$ s with an acquisition time of $T_{acq} = 0.5$ s. (B) The experiment starts with the injection of hyperpolarized pyruvate into a tumor cell solution at $t = -20$ s. At $t = 0$, the first spectrum is acquired with $b = 0$. Then, nine diffusion-weighted spectra are acquired to encode the diffusion properties of all metabolites. At the end of the pulse sequence, 5 spectra with $b = 0$ are acquired, giving a total of 6 spectra without diffusion-weighting for determining T_1 relaxation times and pyruvate-to-lactate label exchange. (C) Here, a part of an exemplary dataset is depicted, showing the relevant carbon spectra starting from $t = 4.5$ s to $t = 21.5$ s. In addition, the signal at $t = 0$ (dashed line) is shown and shifted to the left in the graph for better interpretation.

than the T_1 of pyruvate, which is on the order of 22 s. The exchange rate constant was determined to be $k_{pyr \rightarrow lac} = 0.0031 \text{ s}^{-1}$ (see Appendix A, Fig. 5.10).

The lactate signal was corrected by multiplication with the inverse effective decay of the lactate signal $\exp[+(t + 20s)/T_{1,eff,lac}]$. The argument of the exponential in eq. 5.5 $(t + 20s)(\Delta\rho - k)$ can be expanded into a Taylor series. Because the diffusion experiments are relatively short (40 s), it is possible to neglect higher order terms and use only the first order, hence enabling a linear least squares fit of eq. 5.5. At the expansion point $t = 0$, within the time range $t + 20 \text{ s} = (-20 \text{ s} \dots 20 \text{ s})$ around the expansion point, $\max |(t+20 \text{ s})(\Delta\rho - k)| < 0.57$ holds, leading to a maximum relative error of 11 % due to the approximation for $(t + 20 \text{ s})=20 \text{ s}$ ($T_{1,lac} \sim 13 \text{ s}$, $T_{1,pyr} \sim 22 \text{ s}$, $\Delta t = \pm 20 \text{ s}$, $k_{pyr \rightarrow lac} = 0.0031 \text{ s}^{-1}$). Therefore the following approximation holds for our experiment:

$$M_{lac,z}(t) \cong [Pyr]_0 \cdot k_{pyr \rightarrow lac} \cdot (t + 20s). \quad (5.6)$$

Using this linear approximation, we can estimate $k_{pyr \rightarrow lac}$ from a linear fit to our $T_{1,eff,lac}$ corrected lactate signal intensities at $b = 0$, including the initial signal $I_{lac}(t_0) = 0$. The diffusion-weighted signal of lactate (c.f.) is therefore corrected for both $T_{1,eff,lac}$ and signal increase due to kinetic label exchange with $k_{pyr \rightarrow lac}$, so that we can fit it to a time-independent linear signal equation (c.f. equation 5.3), yielding the ADC of lactate. Postprocessing of all spectra was done with MATLAB 2011b (The MathWorks Inc., Natick, MA).

5.2.3 Calibration and hyperpolarized carbon diffusion

Since gradient performance and eddy currents influence the measurement of ADCs, gradient strength calibration was verified on an in-vitro test sample. The self-diffusion coefficient of 10 % molar fraction H_2O in D_2O at 25°C was determined as $D = (1.97 \pm 0.03) \mu\text{m}^2/\text{ms}$ ($R^2 = 0.9997$, with the error given by the standard deviation (SD) of the fit, see Fig. 5.2 A), corresponding with published values, $D = (1.94 \pm 0.01) \mu\text{m}^2/\text{ms}$ ¹⁷¹. Since diffusion coefficients strongly depend on temperature, we performed an internal temperature calibration with an ethylene glycol NMR thermometer¹⁷². A standard PGSE sequence applied on pure water sample at 25°C gave $D = (2.33 \pm 0.01) \mu\text{m}^2/\text{ms}$, which again is confirmed by literature values¹⁷³. Pure water at 37°C showed an ADC of $D = (3.65 \pm 0.05) \mu\text{m}^2/\text{ms}$, which is around 25 % above literature values¹⁷³ and can be attributed to convection effects arising from temperature gradients due to the nitrogen air flow, which keeps samples at a stable temperature inside the NMR spectrometer. Even though the whole sample is confined to the coil region and susceptibility plugs were used (see subsection NMR measurements), convective flow is present in thermal ^1H diffusion measurements at both low and high temperatures¹⁷⁴.

A carbon reference spectrum of thermally polarized 100 mM pyruvate and 100 mM lactate was acquired, each in cell-free medium (see Fig. 5.2 B) within 128 scans and 30 min at 25°C and ADCs were determined $D_{lac} = (0.91 \pm 0.05) \mu\text{m}^2/\text{ms}$ and $D_{pyr} = (0.98 \pm 0.04) \mu\text{m}^2/\text{ms}$. This shows that there is no difference in diffusion properties between pyruvate and lactate arising from their different molecular sizes.

A hyperpolarized ^{13}C diffusion measurement of 2 mM $[1-^{13}\text{C}]$ pyruvate in 0.8 ml cell-free medium and 0.2 ml D_2O at 37°C is shown for two repeats in Fig. 5.3. Pyruvate signals were corrected for $T_{1,eff}$ ($\alpha = 30^\circ$, $T_1 = 22$ s). ADCs ($\mu\text{m}^2/\text{ms}$) were determined for the first measurement 1.76 ± 0.11 and for the second measurement 1.91 ± 0.13 , $R^2 > 0.99$. The two repeats of the measurement are in agreement and show an expected increase in ADC compared to the thermal measurement, with a factor of $37^\circ\text{C}/25^\circ\text{C}$ contributed by temperature increase according to the Stokes-Einstein equation and an additional increase due to the addition of 20 % D_2O dissolution medium. For hyperpolarized ^{13}C diffusion experiments, the build-up of convection effects is likely to be reduced, as the total measurement time is only 40 s, which is orders of magnitude less than the time required for thermal ^{13}C diffusion measurements at similar compound concentrations.

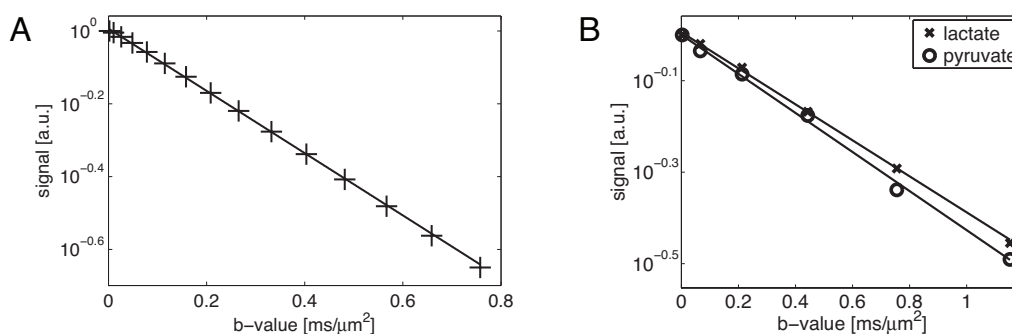


Figure 5.2: Gradient strength calibration verification and control of thermal ^{13}C NMR diffusion setup. (A) Proton NMR diffusion signal of 10 % molar fraction H_2O in D_2O at 25°C as function of b -value to verify calibration of gradient strength. The straight line in the semi-logarithmic plot with a self-diffusion coefficient of $D = (1.97 \pm 0.03) \mu\text{m}^2/\text{ms}$ ($R^2 = 0.9997$, error given by one standard deviation of the fit) well agrees with published values. (B) Thermal ^{13}C NMR diffusion signal of 100 mM pyruvate and lactate, respectively, in cell medium at 25°C as function of b -value acquired from 128 scans within 30 min. Both lactate ($D_{lac} = (0.91 \pm 0.05) \mu\text{m}^2/\text{ms}$) and pyruvate ($D_{pyr} = (0.98 \pm 0.04) \mu\text{m}^2/\text{ms}$) showed a lower apparent diffusion coefficient compared to the self-diffusion coefficient of water, confirming the higher viscosity of the cell medium compared to H_2O .

5.2.4 Hyperpolarization and NMR measurements

A polarization mixture (all chemicals by Sigma Aldrich unless otherwise stated) was prepared containing 14 M $[1-^{13}\text{C}]$ pyruvic acid (Cambridge Isotope Laboratories, Andover, MA), 15 mM OX063 trityl radical (Oxford Instruments, Abingdon, UK) and 10 mM Dotarem (Guerbet, Villeprente, France). In each experiment, 3.75 mg of this mixture were loaded into a HyperSense DNP polarizer (Oxford Instruments) operating at magnetic field ~ 3.35 T, temperature ~ 1.4 K, microwave frequency ~ 94.1 GHz and microwave power ~ 100 mW, and polarized for ~ 40 min. The polarized sample was rapidly dissolved with ~ 5 mL of a dissolution agent, consisting of 10 mM NaOH, 10 mM tris(hydroxymethyl)aminomethane (TRIS) buffer and

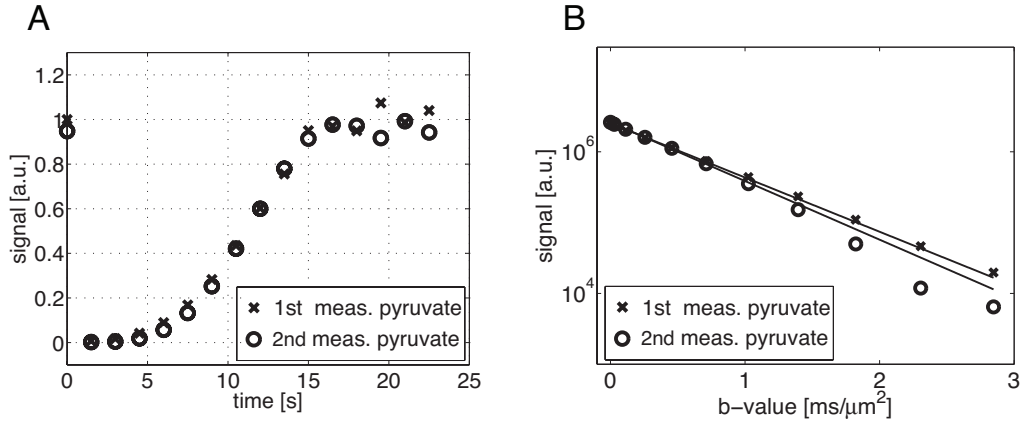


Figure 5.3: Hyperpolarized ^{13}C diffusion measurement of 2 mM ^{13}C -pyruvate in 0.8 ml cell medium and 0.2 ml D_2O at 37°C : (A) pyruvate signal shown for two repeats of the experiment as a function of time corresponding to the diffusion weighting of the sequence depicted in Fig. 5.1. Pyruvate signals were corrected for $T_{1,eff}$ ($\alpha = 30^\circ$, $T_1 = 22$ s). (B) Pyruvate signals were fitted to the Stejskal-Tanner signal equation (c.f. eq. 5.3). The values for the ADCs ($\mu\text{m}^2/\text{ms}$) are for the first measurement $D_{pyr} = 1.76 \pm 0.11$ and for the second measurement $D_{pyr} = 1.91 \pm 0.13$, $R^2_{pyr} > 0.99$. Errors of D are given as SD of a linear fit in the semi-logarithmic plots.

12.5 mg/L disodium ethylenediaminetetraacetate ($\text{Na}_2\text{-EDTA}$) in D_2O (temperature $\sim 185^\circ\text{C}$, pressure ~ 10 bar). The final solution contained 10 mM hyperpolarized $[1\text{-}^{13}\text{C}]\text{pyruvate}$ at 37°C with $\text{pH} \sim 7.4$ and liquid-state polarization of $\sim 25\%$, which was monitored in a Minispec mq40 NMR analyzer (Bruker Optik, Ettlingen, Germany) operating at 0.94 T.

Since the hyperpolarized sample had to be transported to another building, magnetization losses due to T_1 had to be minimized to maintain hyperpolarization. T_1 was increased from ~ 68 s (dissolution in H_2O , 35°C) to ~ 165 s (dissolution in D_2O , 45°C) at 0.94 T field strength, due to decreased dipolar relaxation from both deuterated solvent and increased temperature⁸⁸. After dissolution, the sample was attached to a preheated (45°C) 0.5 T permanent magnet while being transported 0.5 km distance by bicycle to a 14.1 T AvanceIII microimaging system (Bruker BioSpin, Rheinstetten, Germany). It is equipped with a 10 mm (inner diameter) water-cooled micro5-probehead supporting gradient strengths up to 3 T/m. We used an 8 mm double-tuned $^1\text{H}\text{-}^{13}\text{C}$ coil insert. The transport time was 100 s, which leads to a signal decay of around 50 % of the pyruvate in D_2O solution. Of the pyruvate- D_2O solution, 0.2 mL was injected into an 8 mm susceptibility matched NMR glass tube (susceptibility plug, Doty Scientific, Inc., Columbia, USA) containing 0.8 mL of a spheroid suspension (40×10^6 MCF-7 cells) in assay medium.

5.2.5 MCF-7 tumor cell spheroids

The human breast cancer cell line MCF-7 was maintained as a monolayer culture in Dulbecco's modified Eagle's medium (DMEM) supplemented with 5 % fetal calf serum. To obtain three-dimensional aggregates (spheroids), cells were gently stirred in spinner flasks for up to 6 days in a CO₂-incubator at 37°C. For ¹³C-NMR measurements outside of a CO₂-gased environment, spheroid suspensions were transferred to DMEM (with 5 % FCS) containing reduced NaHCO₃ (0.37 g/L) and 20 mM HEPES at pH 7.4 (assay medium) and maintained at 37°C until NMR measurements. The final cell concentration was 50 x 10⁶ cells per mL. Cell number was determined by treating the spheroids with a hypotonic buffer (20 mM HEPES, 1.0 mM MgCl₂, 0.5 mM CaCl₂, pH 7.2) and then with a 5 % benzalkonium chloride solution in glacial acetic acid to obtain a nuclei suspension for electronic counting (CASY)¹⁷⁵.

5.2.6 Determination of dead cells

After NMR-measurements, the spheroid suspension was centrifuged (150 g), the pellet washed twice with PBS, and an aliquot of spheroids incubated at room temperature for 30 min with a solution containing membrane-permeant ethidium homobromide (2 μM), which stains DNA only in dead cells. After centrifugation, the spheroids were fixed in a 3.7 % formaldehyde-PBS solution, analyzed by fluorescent microscopy (Axiovert 200 Zeiss, Göttingen, Germany), and documented with a camera (AxioCam) and AxioVision software. Spheroids were viewed with a FITC and a rhodamine filter to discriminate between general green autofluorescence and the red dead cell staining, resulting in yellow upon merging the two images. The fraction of dead cells was determined from microscopic images (n = 3) using simple color discrimination, which allowed to quantify the area occupied by living cells (shades of green, see Appendix A Fig. 5.11 A,B) as well as the space filled with dead cells (shades of yellow, see Appendix A Fig. 5.11 C). To discriminate fluorescent color intensities, the threshold level between yellow and green was individually adjusted based on color histogram information accounting for the specific lighting conditions. The fraction of dead cells was then calculated by dividing the area occupied by dead cells by the total area occupied by dead and living cells. To check for membrane integrity following Triton X-100 treatment, spheroids were suspended in a 0.03 % trypan blue solution and observed in a light microscope.

5.3 Results

5.3.1 ^{13}C -diffusion coefficients of live and dead tumor cell spheroids

MCF-7 cell spheroids were analyzed at two time points following their transfer to the assay medium: 1) after 2:30 h and 2) after 3:45 h 5.4. Twenty seconds after injection of hyperpolarized $[1-^{13}\text{C}]$ pyruvate, diffusion-weighted spectra were acquired. Pyruvate, pyruvate hydrate, and lactate signals were measured with a linewidth of 10 Hz, allowing for a good separation of signals. At the first time point (Fig. 5.4 A), ^{13}C metabolite ADCs showed apparent differences between pyruvate and lactate, the latter originating in the cells. Lactate has an almost twofold lower ADC than pyruvate. There is no indication of a bi-exponential decay of the pyruvate signal, indicating that it is not detectable in the intracellular compartment. This means that pyruvate is presumably immediately converted into lactate inside the cell. However, at the later time point (Fig. 5.4 B) the ^{13}C ADC values for pyruvate and lactate were very similar, indicating a change in the physiological state of the spheroids. This experiment was repeated at two different time points following the transfer of MCF-7 cells to the assay medium: 1) after 3:00 h and 2) after 5:00 h (see Appendix A Fig. 5.12). Again, at the first time point, lactate has an almost twofold lower ADC than pyruvate. At the second time point ^{13}C ADC values for pyruvate and lactate were very similar, with both pyruvate and lactate ADC decreasing compared to the first time point. An overview of pyruvate and lactate ADCs is given in Fig. 5.4 A and the relative $\text{ADC}_{lac}/\text{ADC}_{pyr}$ ratio is shown in Fig. 5.4 B. Since the spheroid suspension is of high density and is maintained at 37°C in the assay medium without replenishment, the extracellular conditions will eventually change with the depletion of nutrients. This is known to induce cell death accompanied with cell membrane disintegration¹⁷⁶. To determine the pyruvate ADCs within a sample containing such dead spheroids, the assay medium was adjusted to contain 50 % ethanol, which has a self-diffusion coefficient of $1.07 \mu\text{m}^2/\text{ms}$ and is thus twofold lower than that of water at 25°C ¹⁷¹. A concentration of 50 % ethanol is known to lead to cell death due to disruption and inactivation of membranes and cell proteins. As shown in Fig. 5.6 for spheroids maintained under these conditions longer than six hours, the ADCs of both pyruvate and pyruvate hydrate were indeed markedly reduced, and no lactate formation could be determined under this condition, indicating that LDH was also inactivated. The ADCs for pyruvate and pyruvate dehydrate were very similar in two independent experiments, demonstrating the robustness of the method for hyperpolarized diffusion measurement.

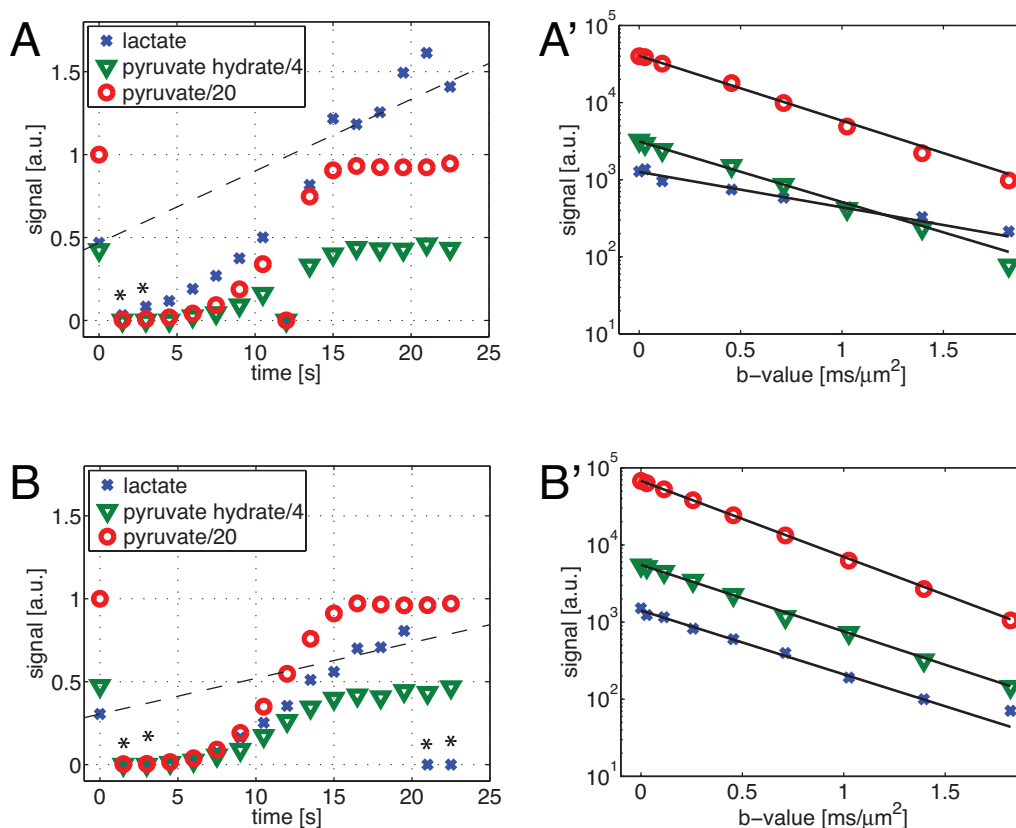


Figure 5.4: Hyperpolarized ^{13}C NMR diffusion signal and label exchange rates from pyruvate to lactate in untreated tumor cells spheroids after various times in assay medium before injection of hyperpolarized ^{13}C -pyruvate: (A) after 2:30 h, and (B) after 3:45 h. For the time corresponding b -values see Fig. 5.1 B. In (A, B) the signals for pyruvate, pyruvate hydrate and lactate are shown as a function of time, as well as the label exchange rate fit (dashed lines). The signal at 12 s was recorded at an incorrect gradient strength and was therefore discarded. (A', B') Signals depicted for lactate, pyruvate hydrate and pyruvate are values fitted according to the Stejskal-Tanner signal equation (c.f. eq. 5.3) and are on a semi-logarithmic scale. All signals exhibit a mono-exponential decay. The values for the ADCs ($\mu\text{m}^2/\text{ms}$) are in (A') for pyruvate 1.94 ± 0.07 , for pyruvate dehydrate 1.81 ± 0.11 , and for lactate 1.06 ± 0.15 ; in (B') for pyruvate 2.27 ± 0.02 , for pyruvate dehydrate 1.99 ± 0.07 , and for lactate 1.91 ± 0.16 . $R^2_{pyrh,pyr} > 0.99$, $R^2_{lac} > 0.95$. Errors of D are given as SD of a linear fit in the semi-logarithmic plots. The signal amplitude of pyruvate at $t = 0$ s was always set as a reference with signal intensity 1. Black asterisks mark signals too weak to be included in further analysis.

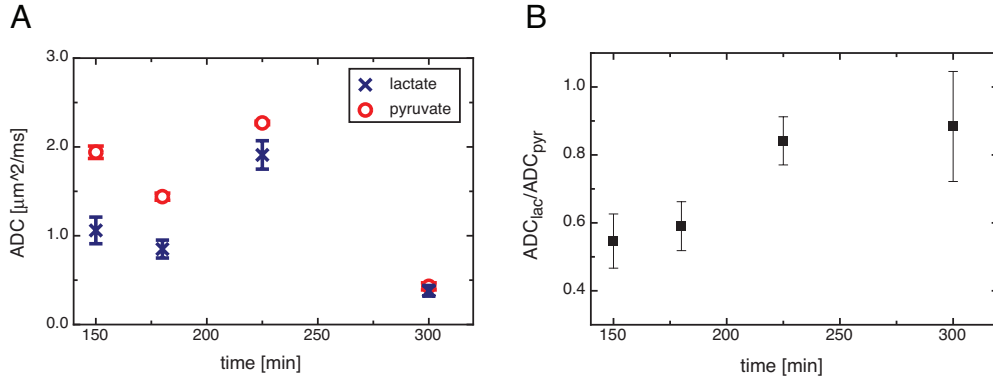


Figure 5.5: Pyruvate and lactate ADCs (A) and their ratio (B) for untreated tumor cell spheroids as a function of time. Time points 2:30 h and 3:45 h correspond to the signals shown in Fig. 5.4, time points 3:00 h and 5:00 h correspond to the signals shown in Fig. 5.12. Variations in both lactate and pyruvate ADC can be observed with time, whereas the $\text{ADC}_{\text{lac}}/\text{ADC}_{\text{pyr}}$ ratio continuously increases over time.

5.3.2 ^{13}C -diffusion coefficients of tumor cell spheroids following gradual membrane permeabilization

To further investigate the diffusion characteristics of tumor cell spheroids undergoing membrane changes, the spheroids were incubated with 0.015 % Triton X-100 in the assay medium. At this concentration of Triton X-100, membrane permeabilization was a gradual process over several hours, as tested in a preceding experiment with trypan blue staining. The results from two independent experiments are summarized in Table 5.1.

exp. & time [label, h]	D_{lac} [$\mu\text{m}^2/\text{ms}$]	D_{pyr} [$\mu\text{m}^2/\text{ms}$]	R^2_{lac}	R^2_{pyr}	$D_{\text{lac}}/D_{\text{pyr}}$	dead cells [%]	$k_{\text{pyr} \rightarrow \text{lac}}$ [$10^{-4}/\text{s}$]
A 1:00	1.38 ± 0.12	2.58 ± 0.10	> 0.98	> 0.98	0.53 ± 0.05	3 ± 1	9.14 ± 1.97
A 2:20	2.03 ± 0.32	2.38 ± 0.03	> 0.96	> 0.98	0.85 ± 0.13	14 ± 5	6.03 ± 1.04
A 3:45	1.81 ± 0.12	1.56 ± 0.06	> 0.99	> 0.99	1.16 ± 0.08	24 ± 8	3.72 ± 1.76
A 5:00	(2.54 ± 0.06)	1.85 ± 0.09	> 0.99	> 0.99	1.37 ± 0.06	n.d.	2.47 ± 0.37
B 0:30	2.42 ± 0.09	2.21 ± 0.42	> 0.99	> 0.96	1.09 ± 0.17	18 ± 3	13.95 ± 2.40
B 1:50	2.16 ± 0.09	2.33 ± 0.35	> 0.99	> 0.97	0.93 ± 0.09	28 ± 9	10.54 ± 1.50
B 3:45	1.40 ± 0.12	1.52 ± 0.19	> 0.98	> 0.98	1.08 ± 0.07	34 ± 11	8.60 ± 0.93

Table 5.1: ADCs acquired after pyruvate-to-lactate label exchange in MCF-7 tumor cell spheroids treated with 0.015 % membrane permeabilizing Triton X-100 in two experiments A (see Fig. 5.7) and B (see Appendix A, 5.13). Errors are given as SD of fits for ADCs and exchange rates. The error for the fraction of dead cells was determined from $n = 3$ microscopy images of the same sample. In experiment A, time point 5:00, the fraction of dead cells was not determinable, since the tumor cell spheroids already disintegrated. Lactate SNR was also very low for this point, such that only 4 points could be used for ADC determination (compare Fig. 5.7 D”).

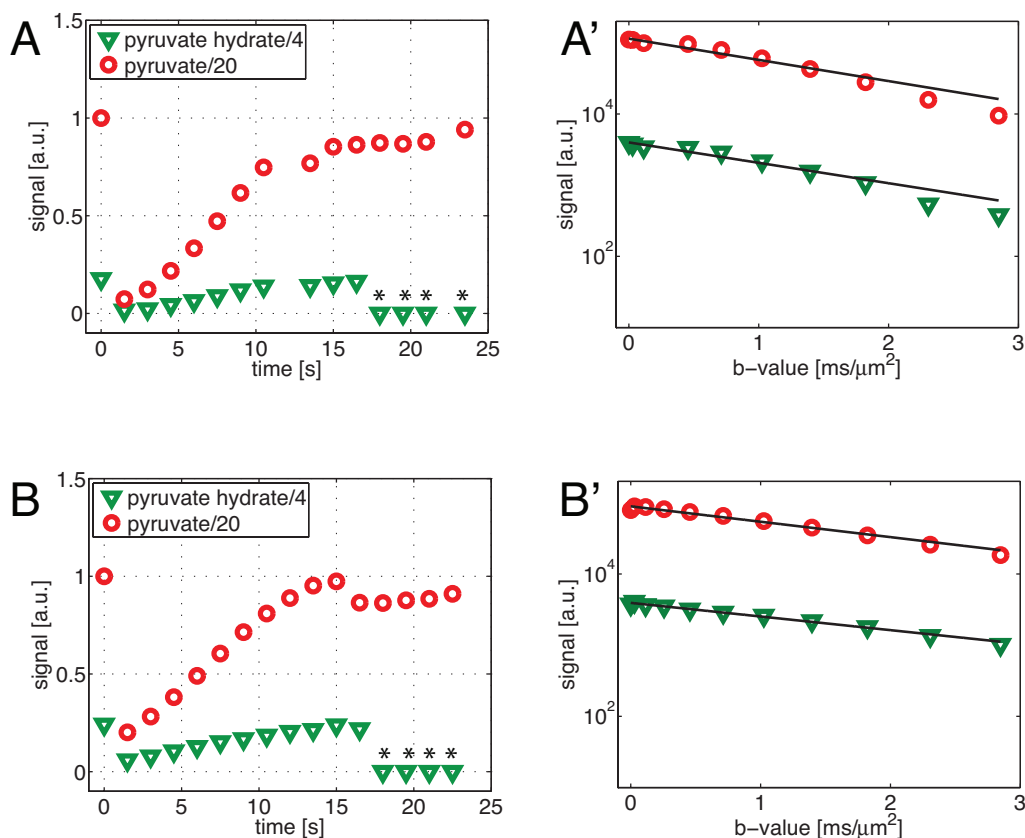


Figure 5.6: Hyperpolarized ^{13}C NMR diffusion signal of ^{13}C -pyruvate metabolites in ethanol-fixed tumor spheroids. ^{13}C -pyruvate was injected into the suspension following transfer into assay medium containing 50 % ethanol (A) after 5:30 h and (B) after 6:30 h. For the time corresponding b -values see Fig. 5.1 B. The signals for (A) pyruvate and (B) pyruvate hydrate are shown as a function of time. (A', B') Signals depicted for pyruvate hydrate and pyruvate are value fitted according to the Stejskal-Tanner signal equation (c.f. eq. 5.3) and are on a semi-logarithmic scale. All signals exhibit a mono-exponential decay. The values for the ADCs ($\mu\text{m}^2/\text{ms}$) are in (A') for pyruvate 0.69 ± 0.07 , and for pyruvate dehydrate 0.66 ± 0.01 ; in (B') for pyruvate 0.50 ± 0.04 , and for pyruvate dehydrate 0.44 ± 0.04 ($R^2_{\text{pyr}h,\text{pyr}} > 0.95$). No lactate was detected. Errors are given as SD of a linear fit in semi-logarithmic plots. The signal amplitude of pyruvate at $t = 0$ s was always set as a reference with signal intensity 1. Black asterisks mark signals too weak to be included in further analysis.

In the first series of experiments, within 4 h, lactate ADCs increased almost twofold during Triton X-100 exposure and $\text{ADC}_{lac}/\text{ADC}_{pyr}$ ratio approached unity, indicating a gradual blending of intracellular and extracellular compartments. In the same time span, the metabolic rates of pyruvate-to-lactate label exchange, i.e. lactate dehydrogenase activity, diminished, while the fraction of dead cells increased. To confirm membrane breakdown, dead cells were labeled with a DNA staining solution immediately after the NMR measurement and fixed for fluorescent microscopy to determine the extent of cell death (Fig. 5.7 A"-D"). After 5 h, very few cell aggregates remained (Fig. 5.7 D"), indicating that Triton X-100 had ruptured the cell membranes, leading to cell lysis and spheroid deterioration. In this sample, a quantification of dead cells was no longer possible.

In the second series of experiments, after 30 min of Triton X-100 exposure $\text{ADC}_{lac}/\text{ADC}_{pyr}$ ratio is at unity, indicating already a gradual blending of intracellular and extracellular compartments. This more sensitive response to the Triton X-100 treatment compared to the first experiment corresponds to a relatively high number of 18 % dead cells at the first time point. Within 4 h, lactate dehydrogenase activity diminished, while the fraction of dead cells increased. ADCs of both pyruvate and lactate decreased until the latest timestep, with the $\text{ADC}_{lac}/\text{ADC}_{pyr}$ ratio around unity.

An overview of both experiments with cells undergoing treatment with Triton X-100 is given in Fig. 5.8, relating the fraction of dead cells to the pyruvate and lactate ADCs (Fig. 5.8 A), to the $\text{ADC}_{lac}/\text{ADC}_{pyr}$ (Fig. 5.8 B), and to the pyruvate-to-lactate label exchange rate (Fig. 5.8 C).

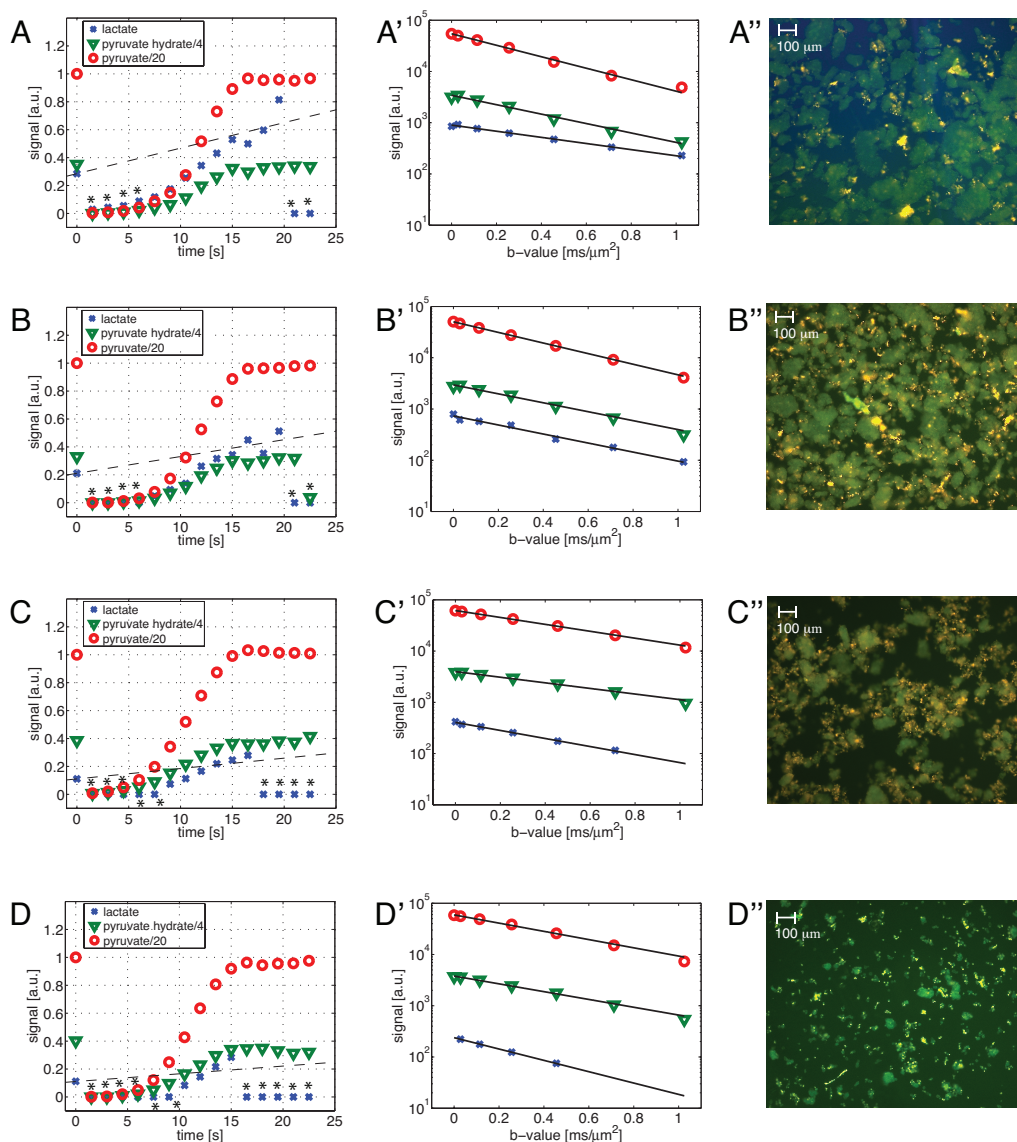


Figure 5.7: Hyperpolarized ^{13}C NMR diffusion signal of tumor cell metabolites and label exchange rate from pyruvate to lactate in cancer cells at 37°C after various times of incubation with Triton X-100 (0.015 %). Numerical results are shown in Table 5.1, corresponding to experiment A. (A, B, C, D) Lactate, pyruvate hydrate and pyruvate signal as a function of time, as well as label exchange rate fit from pyruvate to lactate, for hyperpolarized pyruvate injected into cell medium after 1:00 h, 2:20 h, 3:45 h, and 5:00 h of treatment with Triton X-100. Black asterisks mark signals too weak to be included in further analysis. (A', B', C', D') Lactate, pyruvate hydrate and pyruvate signals from Fig. 5.7 A, B, C, D and the corresponding fits to the Stejskal-Tanner signal equation on a semi-logarithmic scale as function of the b -value. (A'', B'', C'', D'') Fluorescent microscopy images of live cells (green) and dead cells (yellow), corresponding to the respective experiments in Fig. 5.7 A, B, C, D. The method to determine the extent of cell death is described in the supporting information, Fig. 5.11. The signal amplitude of pyruvate at $t = 0$ s was always set as a reference with signal intensity 1.

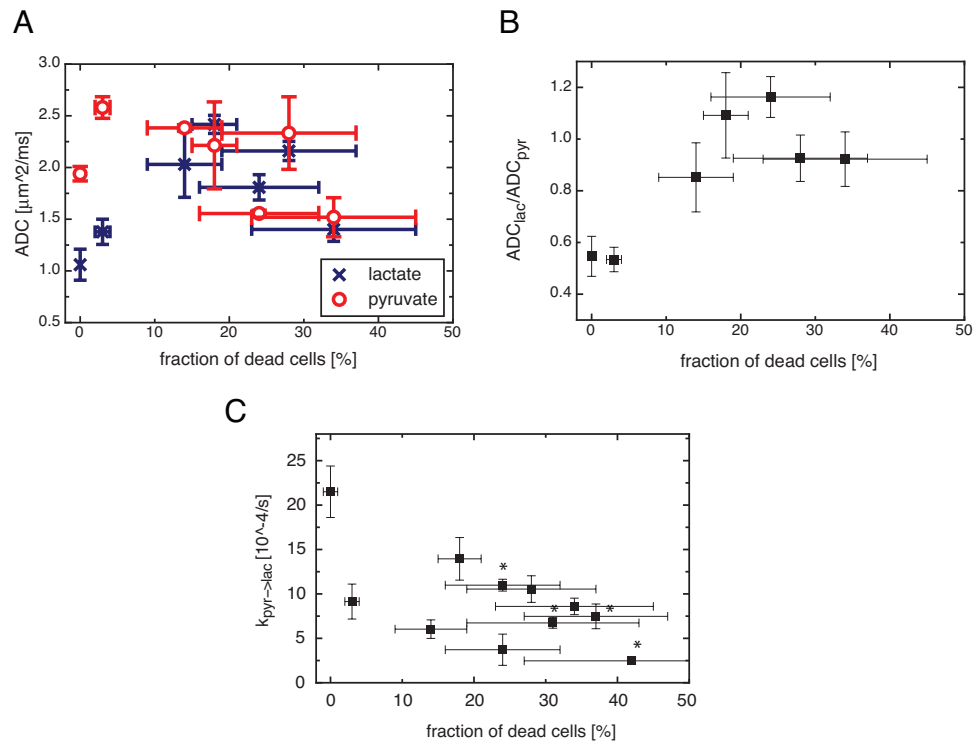


Figure 5.8: Overview of ADCs of pyruvate and lactate (A), $\text{ADC}_{\text{lac}}/\text{ADC}_{\text{pyr}}$ ratio (B), and pyruvate-to-lactate label exchange rates (C) related to the fraction of dead cells determined by fluorescence microscopy. Data from the experiment with untreated tumor cell spheroids after 2:30 h (data from Fig. 5.4) was combined with that from further experiments (shown in Table 5.1), where tumor cell spheroids were treated with membrane permeabilizing Triton X-100. Black asterisks mark kinetic rate constant values for which no corresponding diffusion information could be obtained due to low signal.

5.4 Discussion

In the past ^{13}C -metabolite ADC measurements were very time extensive, making such measurements prone to errors due to macroscopic motion and flow¹⁰⁸. However, taking advantage of the $> 10,000$ fold amplified hyperpolarized ^{13}C signal, we were able to measure metabolite ADCs in combination with metabolic rate constants in real-time. ADCs were measured within 25 s for pyruvate and pyruvate hydrate at concentrations below 2 mM and for lactate below 100 μM . In a conventional thermally polarized ^{13}C diffusion experiment, this sensitivity would require experiment times of several months.

Since in this study our focus was on the determination of the ADC, the relative errors arising from simplified determination of the kinetics were accepted. Further experiments with a pulse sequence that alternates between diffusion encoding and regular acquisition are being performed, so that a full kinetic modeling approach can be applied in the future¹⁶⁰. The robustness of our method for determining ADCs from hyperpolarized substrates was demonstrated in experiments, where hyperpolarized pyruvate was injected into cell-free medium. The possibility of measuring low concentrations of substrates within 25 s at a temperature of 37°C might be advantageous for other cases where long signal averaging cannot be performed due to convection effects.

Hyperpolarized diffusion measurements rely on signal correction for flip angle excitation, T_1 relaxation, and the kinetic rate constant for lactate ADCs. While the flip angle could be calibrated very accurately in our high field spectrometer, T_1 and $k_{pyr \rightarrow lac}$ had to be determined experimentally. Artificially introducing a $\pm 10\%$ error in T_1 led to an error $< \pm 5\%$ for the ADC values, whereas introducing a $\pm 10\%$ error for kinetic rate constants $k_{pyr \rightarrow lac}$ led to an error $< \pm 2\%$ for the ADC values. Both results demonstrate a high robustness of ADC determination.

Analyzing MCF-7 tumor cell spheroids under standard growth conditions yielded a lactate ADC of $D_{lac} = (1.06 \pm 0.15) \mu\text{m}^2/\text{ms}$, a value about twofold lower than that of pyruvate. Both the absolute value of intracellular lactate ADC and the ratio between lactate ADC and pyruvate ADC match the values obtained by proton diffusion spectroscopy^{177,178}. However, thermal $[1-^{13}\text{C}]$ lactate ADC measurements obtained from rat glioma *in vivo* after signal-averaging showed significantly lower ADCs than in our cell study¹⁶⁵, which could be explained by a higher cellularity of a tumor *in vivo*. No experimental evidence was found in our diffusion measurements for pyruvate being present in the same intracellular diffusion compartment as lactate, since this would have led to a bi-exponential decay of pyruvate. This suggests that pyruvate was converted to lactate inside the cell faster than the timescale of our diffusion encoding and moreover supports the assumption that, at least in these cells, the observed exchange rate of pyruvate to lactate was not limited by intracellular LDH activity and NADH levels, but rather by the rate of uptake mediated by monocarboxylate transporters^{155,179}. The situation of pyruvate uptake in viable cells is depicted in a model in Fig. 5.9 A. The evidence that lactate ADC stems from the intracellular compartment, whereas pyruvate ADC represents extracellular compartment in viable cells, made us investigate situations, in which cell are under detrimental conditions:

Such conditions were given when 1) the cells were maintained in the assay medium outside of an CO_2 -gas environment at 37°C for up to five hours, and 2) cells were treated with Triton X-100 to gradually permeabilize the cell membrane to mimic a necrotic process. While the untreated cells undergoing pathological changes presumably due to nutrient consumption by the cells at high density, which is known to lead to necrosis and thus cell leakage¹⁷⁶, the treated cells were permeabilized due to the effect of Triton X-100. In both cases, initially an initial increase in lactate ADC was observed. The $\text{ADC}_{\text{lac}}/\text{ADC}_{\text{pyr}}$ ratio increased with time, finally approaching unity, which can be explained by an increased blending of the intra- and extracellular compartments with time. In the last time steps, both lactate ADC and pyruvate ADC decreased again, presumably due to further cell lysis, which leads to molecular leaching through the disrupted membrane and eventually exposes the metabolites to a common molecular environment. This situation of membrane breakdown and the blending of compartments is illustrated in a model in Fig. 5.9 B. Fluorescent staining showed that an increase of the $\text{ADC}_{\text{lac}}/\text{ADC}_{\text{pyr}}$ ratio correlates

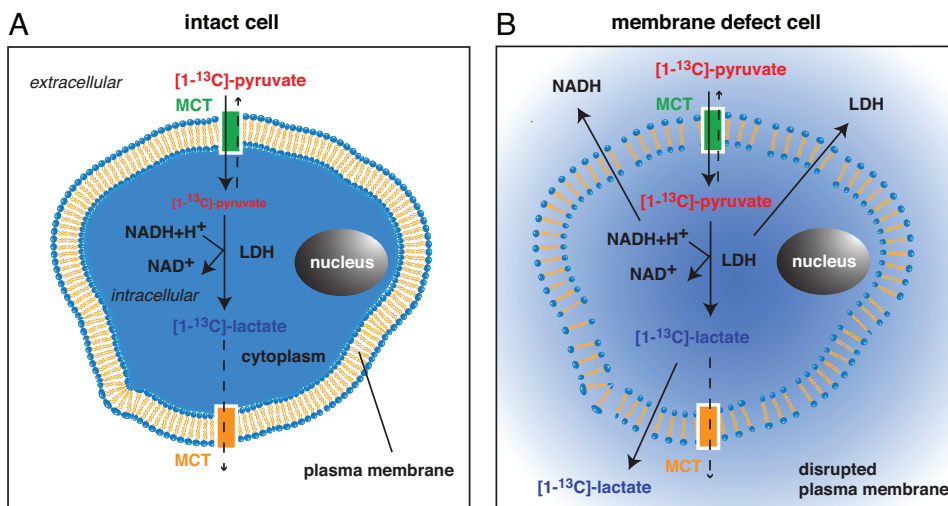


Figure 5.9: Model of pyruvate-to-lactate label exchange (A) in intact (live) cells and (B) with permeabilized cells. In intact cells pyruvate is taken up via monocarboxylate transporters (MCTs) located in the plasma membrane. Within the intact cell (A), pyruvate is rapidly converted to lactate, catalyzed by lactate dehydrogenase (LDH) and depending on the level of NADH produced by glycolysis. This scenario corresponds to the different diffusion coefficients measured for pyruvate (extracellular, relatively high ADC) and lactate (intracellular, relatively low ADC). When cell membranes become leaky due to beginning necrosis or permeabilization by detergents or other agents (B), small molecules, including pyruvate, lactate and NADH, are the first to diffuse out of the cell; at later stages with the breakdown of intracellular membrane structures, proteins and nucleic acids will also be solubilized in the overall blending of extracellular and intracellular compartments. This scenario of blended compartments can explain why pyruvate and lactate have the same diffusion coefficients. It should be noted that LDH remains active, but the conversion rate of pyruvate to lactate is low due to dilution of NADH.

to an increase in the fraction of dead cells until a complete blending of the intra- and extracellular compartments is reached and $\text{ADC}_{\text{lac}}/\text{ADC}_{\text{pyr}}$ ratio approaches unity.

Then, the ADCs of both pyruvate and lactate were decreased, while the fraction of dead cells increased. This decrease suggests an increase in the viscosity of the molecular environment, resulting from the release of proteins and DNA from the lysing cells^{156,180}.

In our experiments, a decrease in the exchange rate of pyruvate to lactate, as a measure of metabolic activity, also appears to correlate with the fraction of dead cells. This would be expected when NADH concentration decreases (see Fig. 5.9 B). However, the exchange rate depends on various other factors, cellular pyruvate uptake, LDH activity, the intracellular lactate pool³⁹, as well as perfusion *in vivo*, so that it does not necessarily correlate with the fraction of dead cells. In a recent study, pyruvate-to-lactate conversion has been shown to decrease in breast but not in prostate cancer cells upon treatment, indicating the complexity of different factors affecting pyruvate-to-lactate exchange⁴⁶. In contrast to a characterization of response-to-treatment solely by exchange measurements, the combination of both kinetic and diffusion measurements is a new approach which could give an added benefit in characterizing membrane permeability and cell death upon treatment. For measurements in tumors, one has to consider that lactate may also be extruded into the extracellular space, making interpretation of lactate ADC measurements more complex. But diffusion spectroscopy of lactate would allow to differentiate between extra- and intracellular compartments and to quantify the relative fraction of metabolites in their respective compartment. Increased extracellular lactate could be an indicator of necrotic cells. Proton diffusion has been used as marker for response-to-treatment analysis in tumors for more than a decade^{46,162,163}. In contrast to protons, which are present in all tissue compartments, hyperpolarized lactate is a purely intracellular marker in viable cells following pyruvate-to-lactate conversion inside the cell. Therefore, the ADC of lactate in combination with the detection of the ADC of pyruvate, may be a more sensitive marker than the ADC of protons for detecting changes in membrane permeability. Quantitative real-time diffusion measurement benefits not only spectroscopic applications, but also localized ¹³C imaging techniques. It has been shown recently that diffusion-weighted imaging based on the stimulated-echo acquisition mode sequence (STEAM) is feasible for producing diffusion-weighted ¹³C-images from ¹³C-metabolites, highlighting tumor areas and at the same time suppressing signals from the vasculature⁴⁹. However, the method lacks of quantitative molecular information on diffusion in terms of an ADC. We therefore see many new applications of a real-time spectroscopic imaging technique¹⁸¹, if it is combined with quantitative diffusion weighting. One problem arising when dealing with human MRI is that the common gradient systems supply gradient strengths only up to 50 mT/m. While special gradient inserts operating at higher gradient strengths are commercially available, peripheral nerve stimulation has to be considered when performing experiments *in vivo*.

In conclusion, we have demonstrated that hyperpolarized ¹³C diffusion-weighted spectroscopy is feasible. For the first time, ADCs of ¹³C-metabolites could be measured in real-time in cells. As a new technique, ¹³C ADCs can also provide information on the viability of tumor cells. Since an increase in ADC_{lac}/ADC_{pyr} ratio correlated with the fraction of dead cells, these metabolite ADCs are good indicators of necrosis making them useful tools for monitoring the pathological state of tumors *in vivo*.

5.5 Acknowledgements

For cultivation and preparation of the tumor cell spheroids we received the expert assistance of Josef Hintermair, while Johannes D. Scholz was of indispensable help with the experiments by operating between the different locations. We greatly appreciate the fruitful discussions with Jan Henrik Ardenkjær-Larsen. The NMR experiments were performed at the Bavarian NMR Center, Technische Universität München. This work was supported by a grant from the Bundesministerium für Bildung und Forschung (BMBF, FKZ 01EZ1114). The authors take responsibility for the content of the publication. F.S. thanks the Fonds der Chemischen Industrie and the Institute for Advanced Study at the TUM for financial support and acknowledges support from the TUM Graduate School and the Faculty Graduate Centre of Chemistry. S.J.G. acknowledges support from the DFG (GI 203/6-1) and from the Fonds der Chemischen Industrie.

5.6 Appendix A: Supplementary figures

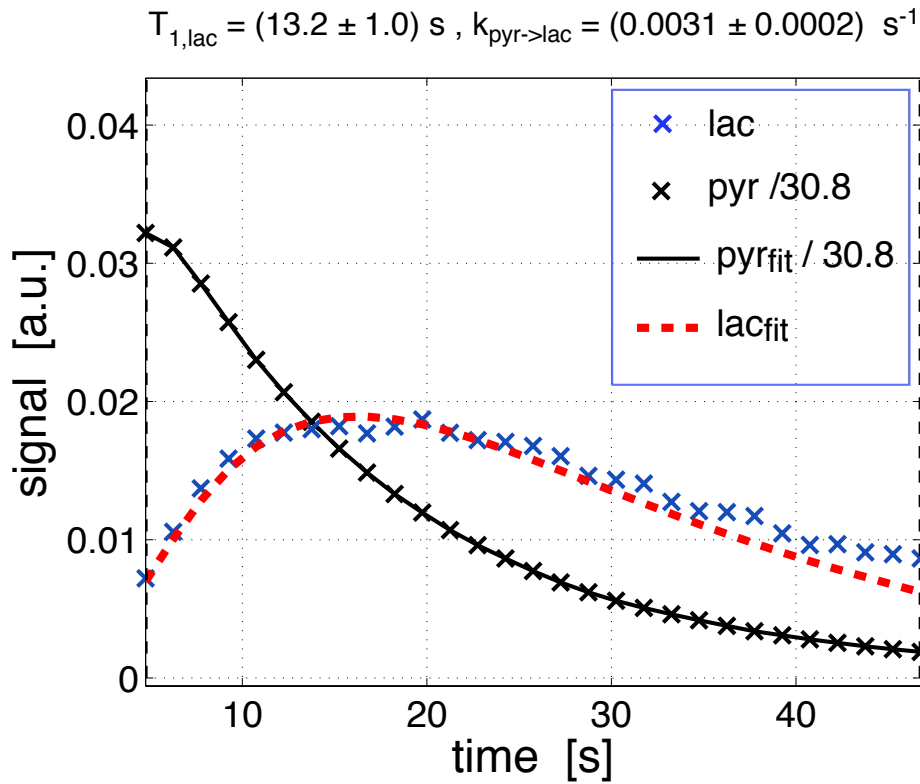


Figure 5.10: Standard pulse-acquire NMR experiment without diffusion weightings, where we followed the signal build-up of lactate seven seconds after injection of pyruvate with $\text{TR} = 1.5 \text{ s}$ and a flip angle of 5° . 2-site kinetic modeling¹⁶⁰ gave a $T_{1,\text{lac}}$ of 13.2 s. The exchange rate constant was determined to be $k_{\text{pyr} \rightarrow \text{lac}, 2\text{-site}} = 0.0031 \text{ s}^{-1}$.

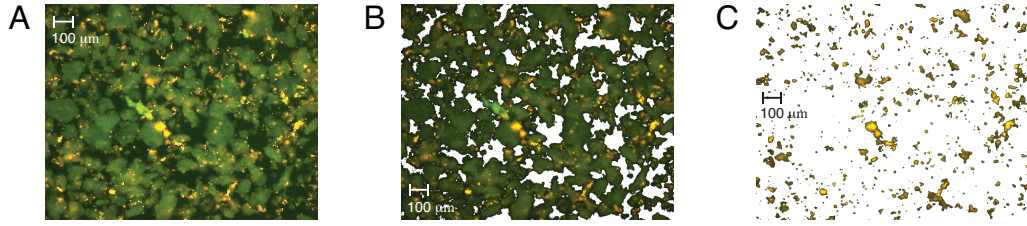


Figure 5.11: Staining and quantification of dead cells. (A) Exemplary fluorescent microscopy image of live spheroids (green) and dead cells (yellow) after NMR-measurements. (B) Area occupied by live and dead cells (green and yellow) without background (white). The threshold level between cells and background was based on color histogram information accounting for specific illumination conditions. (C) Area occupied by dead cells (yellow) only. The threshold level between living and dead cells was again based on color histogram information accounting for specific lighting conditions.

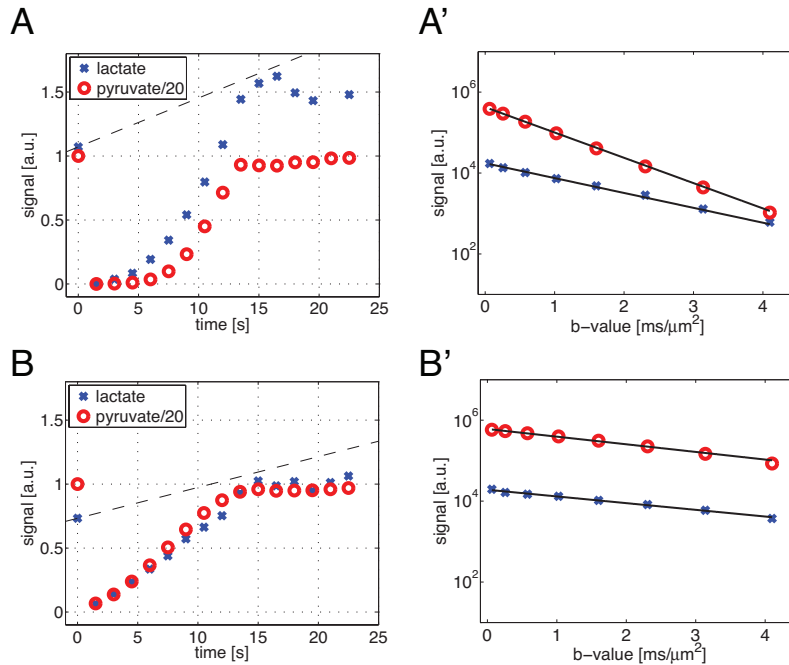


Figure 5.12: Hyperpolarized ^{13}C NMR diffusion signal and label exchange rates from pyruvate to lactate in untreated tumor cells spheroids after various times in assay medium before injection of hyperpolarized ^{13}C -pyruvate: (A) after 3:00 h, and (B) after 5:00 h. In (A, B), the signals for pyruvate and lactate are shown as a function of time, as well as the label exchange rate fit (dashed lines). (A', B') Signals depicted for lactate and pyruvate are values fitted according to the Stejskal-Tanner signal equation (c.f. eq. 5.3) and are on a semi-logarithmic scale. All signals exhibit a mono-exponential decay. The values for the ADCs ($\mu\text{m}^2/\text{ms}$) are in (A') for pyruvate 1.44 ± 0.03 and for lactate 0.85 ± 0.10 ; in (B') for pyruvate 0.43 ± 0.03 and for lactate 1.38 ± 0.06 . $R_{pyr}^2 > 0.99$, $R_{lac}^2 > 0.96$. Errors of D are given as SD of a linear fit in the semi-logarithmic plots. The signal amplitude of pyruvate at $t = 0$ s was always set as a reference with signal intensity 1. The set of gradient strengths [T/m] in temporal order was 0, 2.7, 2.4, 2.1, 1.8, 1.5, 1.2, 0.9, 0.6, 0.3, 0, 0, 0, 0, 0 with the sequence parameters depicted in Fig. 5.1 A.

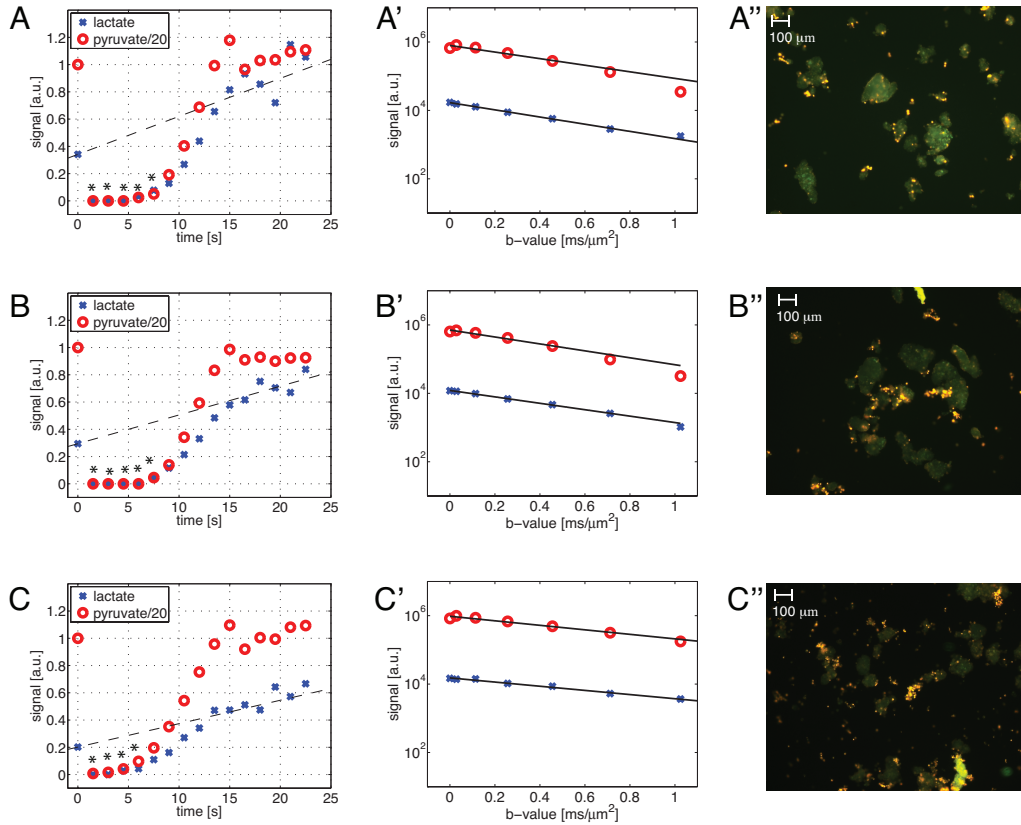


Figure 5.13: Hyperpolarized ^{13}C NMR diffusion signal of tumor cell metabolites and label exchange rate from pyruvate to lactate in cancer cells at 37°C after various times of incubation with Triton X-100 (0.015 %). Numerical results are shown in Table 5.1, corresponding to experiments B. (A, B, C) Lactate and pyruvate signal as a function of time, as well as label exchange rate fit from pyruvate to lactate, for hyperpolarized pyruvate injected into cell medium after 0:30 h, 1:50 h, and 3:45 h of treatment with Triton X-100. Black asterisks mark signals too weak to be included in further analysis. (A', B', C') Lactate and pyruvate signals from A, B, C and the corresponding fits to the Stejskal-Tanner signal equation on a semi-logarithmic scale as function of the b-value. (A'', B'', C'') Exemplary fluorescent microscopy images of live cells (green) and dead cells (yellow), corresponding to the respective experiments in A, B, C. The method to determine the extent of cell death is described in the supporting information, Fig. 5.2. The signal amplitude of pyruvate at $t = 0$ s was always set as a reference with signal intensity 1.

5.7 Appendix B: Measurement of ADCs of hyperpolarized ^{13}C -metabolites in vivo

5.7.1 Introduction

Measurements of diffusion or T_2 relaxation are mostly based on the spin echo or stimulated echo pulse sequence, consisting of an excitation pulse in combination with a refocusing pulse and three excitation pulses respectively¹⁸². Since the magnetization of hyperpolarized ^{13}C -metabolites decays irreversibly to thermal equilibrium with a relaxation time constant T_1 , typically one to two orders of magnitude larger than T_2 ^{50,183}, it is preferable to store the magnetization along the longitudinal axis during the measurement. Repeated low flip angle excitation and refocusing allows creation of spin echoes with arbitrarily chosen echo times and at the same time stores the hyperpolarized magnetization along the z -axis, allowing adjustment of the echo time. Compared to the spin echo, in a stimulated echo only half of the spins contribute to the signal leading to a reduction in signal-to-noise ratio. Additionally, varying diffusion weightings without changing the echo time interferes with storage of the longitudinal magnetization. Therefore, we focus on the spin echo sequence for diffusion measurements of hyperpolarized metabolites.

The most important part of the spin echo pulse sequence when it comes to *in vivo* measurements of hyperpolarized metabolites is the refocusing pulse, since imperfect refocusing or inversion leads to an additional irreversible decay of the hyperpolarized signal. Therefore, an optimal pulse for *in vivo* spin echo measurements of hyperpolarized metabolites has a perfect band-selective inversion and refocusing profile with minimal chemical shift displacement error; at the same time the pulse is as short as possible to minimize relaxation losses during the pulse and is robust to B_1 amplitude deviations; obviously such a pulse does not exist under realistic conditions. Previously, Shinnar-Le-Roux (SLR) pulses^{183,184} and adiabatic pulses^{50,185} have been used to this end but suffer from limitations, e.g. SLR pulses have relatively low robustness with regard to B_1 inhomogeneities and adiabatic pulses have to be used in pairs preventing the use of short echo times.

In collaboration with researchers from the *DTU Copenhagen* we have implemented and tested for *in vivo* ^{13}C -diffusion experiments a S-BURBOP-20% universal-rotation pulse optimized using optimal control theory^{17,18,22,26}, which is robust to 20 % B_1 imperfections and shows a stable refocusing and inversion profile over a bandwidth of 2 kHz for a maximum amplitude $B_{1,max} = 714$ Hz and pulse length 9.1 ms.

5.7.2 Methods

We designed a diffusion-weighted pulse sequence based on the pulsed gradient spin echo (PGSE) sequence using low flip angle ($\alpha = 20^\circ$) slice selective excitation (Fig. 5.14 A). A universal-rotation pulse optimized with optimal control theory (S-BURBOP-20%) was implemented for the 180° refocusing pulse. The 9.1 ms long

pulse is robust to 20 % B_1 imperfections and shows a stable refocusing and inversion profile over a bandwidth of 2 kHz. We used diffusion time $\Delta = 20$ ms, gradient time $\delta = 8$ ms, and rectangular gradient pulses with amplitudes up to $g = 0.5$ T/m in x -, y -, and z -direction. The sequence was repeated (TR = 200 ms) in a loop structure starting with a reference scan for $b = 0$ and then continuing with large b -values in all three gradient directions (Fig. 5.14 B). The signal equation is given by the Stejskal-Tanner expression modified by an $T_{1,eff}$ decay, consisting of T_1 and loss of M_z due to repeated excitations.

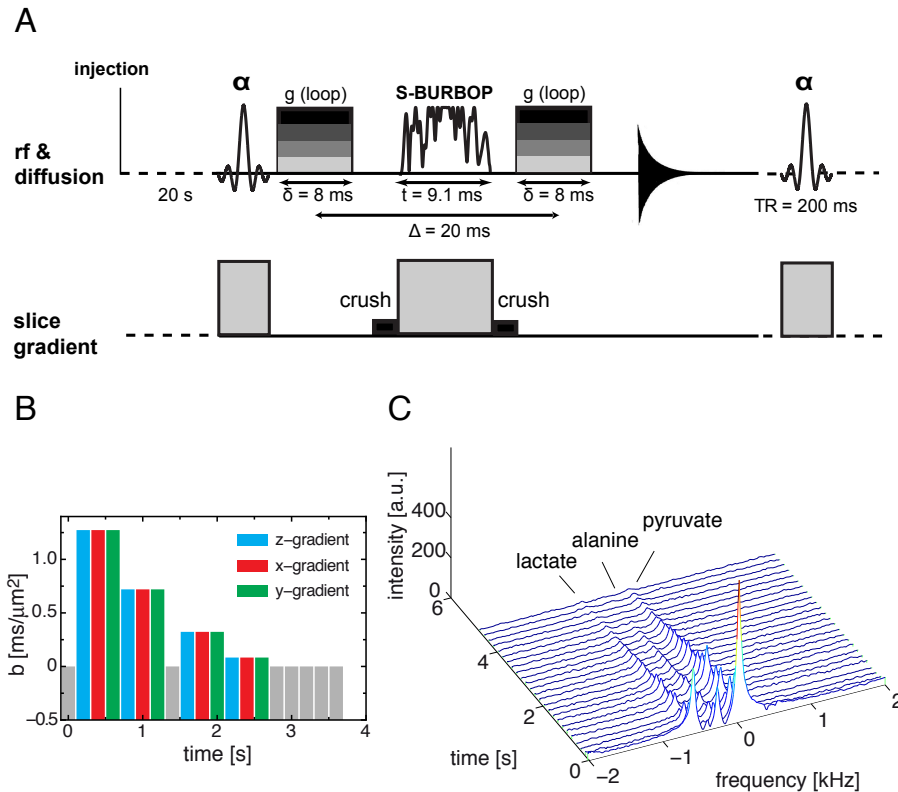


Figure 5.14: (A) Pulse sequence for measurement of hyperpolarized ^{13}C -metabolite ADCs *in vivo*. (B) Gradient scheme for diffusion encoding in 3 orthogonal directions (C) Exemplary *in vivo* diffusion dataset in muscle tissue acquired 20 s after injection of pyruvate.

An exemplary dataset from a diffusion experiment is shown in Fig. 5.14 C. For post-processing, a correction based on $T_{1,eff}$ was performed before data were fitted to the signal equation assuming a mono-exponential damping term (Fig. 5.15 A,B,C). Two rats were scanned using this protocol in a preclinical 4.7 T MR scanner (Agilent, USA), equipped with a 4-channel ^{13}C receive array and a single volume transmit coil ($\gamma/2\pi B_{1,max} = 714$ Hz) (RAPID Biomedical, Germany). A 20 mm axial slice covering the animal's thigh muscle was chosen. Metabolite concentration maps were acquired with a FID-CSI sequence with spiral ordering (see Fig. 5.16, shown for coil element 1). $[1-^{13}\text{C}]$ pyruvate was hyperpolarized using a HyperSense DNP polarizer

(Oxford Instruments, UK) and 1.5 ml was injected into a tail vein over ~ 15 s followed by data acquisition 20 s later.

5.7.3 Results and discussion

The new diffusion pulse sequence was tested in a reference phantom with two syringes, containing ^{13}C -urea and ^{13}C -glycine respectively. Shifting the transmitter offset to 500 Hz and 1000 Hz from resonance yielded equivalent ADC values (data not shown) proving the robustness of the sequence. The S-BURBOP pulse was shown to be useful because of its universal rotation property, broad bandwidth, frequency-selectivity, and B_1 robustness. In rats, we acquired ^{13}C -metabolite ADCs in 3 spatial directions from lactate, alanine and pyruvate in muscle tissue at 4 different positions corresponding to the respective coil element. Quantitative ADC values are shown for all coil elements in Fig. 5.15. Lactate and alanine ADCs were lower compared to pyruvate ADC, indicating a more confined diffusion space consistent with the presence of the two metabolites in the intracellular compartment. In conclusion, we have demonstrated for the first time, that *in vivo* ADC measurement of ^{13}C metabolite ADCs is possible using hyperpolarized nuclei. The analysis of diffusion properties of intracellularly produced hyperpolarized compounds might potentially be useful for characterizing pathological changes in tumor cells, e.g. if the cellular compartments and diffusion properties change due to breakdown of the plasma membrane.

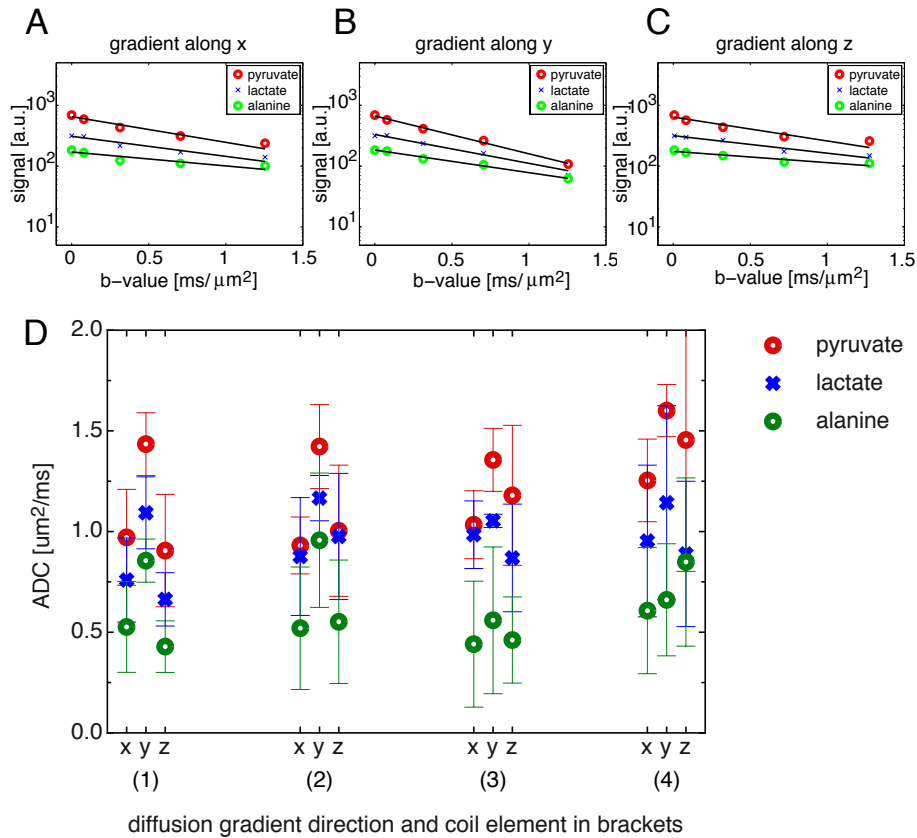


Figure 5.15: (A,B,C) $T_{1,eff}$ corrected diffusion peak intensities for x -, y -, z -gradient direction and mono-exponential fits ($R^2 > 0.95$) for coil element 1. (D) Respective ADC values for all four coil elements.

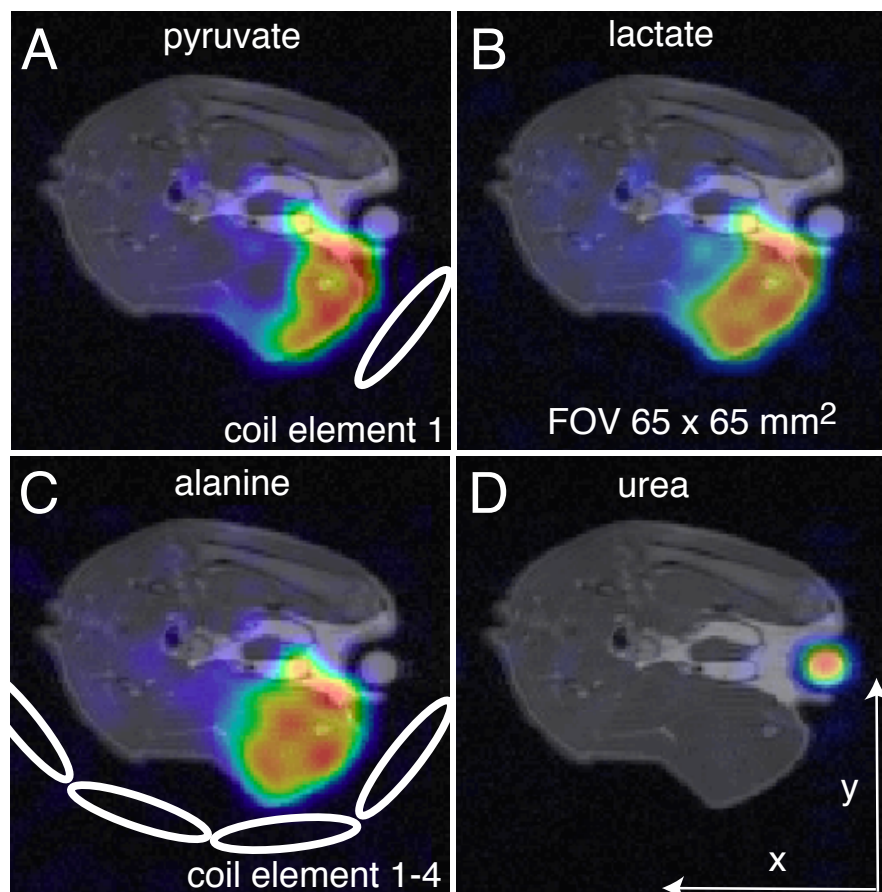


Figure 5.16: FID-CSI images showing the spatial distribution of (A) pyruvate, (B) lactate, (C) alanine, and (D) a urea phantom in a rat thigh muscle. In (A) and (D) the coil position positions are depicted. (D) shows the gradient directions. Signals are only depicted for coil element 1 in all images.

6 Non-invasive lipid measurement in living insects using NMR microscopy

“There are living systems; there is no living ‘matter’. No substance, no single molecule, extracted and isolated from a living being possess, of its own, the aforementioned paradoxical properties. They are present in living systems only; that is to say, nowhere below the level of the cell”

— Jacques Lucien Monod (* 1910; † 1976)

Reprinted from *The Journal of Experimental Biology*, volume 215, pp. 3137-3147 (2012); Franz Schilling*, Kai Dworschak*, Reinhard Schopf, Ralph Kühn, Steffen J. Glaser, and Axel Haase; **Non-invasive lipid measurement in living insects using NMR microscopy**. With permissions from The Company of Biologists Ltd. Modifications: replacement of Abstract by Summary, addition of Appendix A. *contributed equally.

Summary

Nuclear magnetic resonance (NMR) microscopy allows us to image and quantify the distribution of NMR-active nuclei in living specimens. Using high-field NMR microscopy at a magnetic field strength of 14.1 T and strong gradients up to 3 T/m, we show that separation of fat and water nuclear resonances in living insects can be achieved. In contrast to destructive conventional photometric and mass measurements, we demonstrate exemplarily in the European spruce bark beetle that NMR can be efficiently used to quantify absolute fat and water content in living insects. Additionally, anatomic images with a spatial in-plane resolution up to 10 μm and with high soft tissue contrast were acquired. We demonstrate that fat

distribution and fat consumption of living insects can be obtained by magnetic resonance imaging (MRI). This enables future research to address questions where single individuals have to be measured several times, which is not possible with conventional destructive methods.

6.1 Introduction

Lipids in the form of triglycerides, which are stored in the diffuse fat body, are the main energy reserves in most insects. These reserves are crucial for processes such as insect flight^{186,187} or the survival success of overwintering insects¹⁸⁸. Lipid reserves are regularly used as fitness parameters for animals^{189–191}. Classic lipid measurement methods such as chromatography and vanillin or ferric perchlorate assays require chemical extraction and thus the killing of animals¹⁸⁷. This fact disables researchers to test fluctuations in the amount of lipid(s) in the same individuals with changing conditions over time. For this purpose, only indirect measures such as correlations with body mass adjusted for size or measuring reference individuals from the same population remain. These indirect methods are much more inaccurate and in many cases may be inappropriate^{192,193}.

In recent years, zoology has adopted non-invasive methods widely used in human medicine. Anatomy of fossil amber arthropods was reconstructed and visualized using computed tomography^{194,195}, morphology of an octopus was studied using ultrasound¹⁹⁶ and quantitative nuclear magnetic resonance (NMR) was used to quantitatively measure the body composition of small rodents^{197,198}. NMR is a non-destructive and non-invasive technique used to analyse and study the internal morphology of living specimens⁶³. In every living animal, there are many water protons whose NMR-specific parameters, such as the proton spin density, chemical shift, and T_1 and T_2 relaxation times, can be spatially resolved by magnetic resonance imaging (MRI)⁵⁹. With the advent of high magnetic field strengths and strong magnetic gradients, spatial resolution of up to one micrometer resolution is achievable¹⁹⁹. The first NMR microscopy images were obtained by Aguayo et al. in 1986, when they studied ova from the toad *Xenopus laevis*²⁰⁰. Since then, a new dimension of investigating animals opened up and many different species have been characterized by NMR microscopy: e.g. the development of a locust embryo²⁰¹, pH metabolism of living insects²⁰², development and metamorphosis of lepidopteran pupae^{203,204}, metamorphosis of the silkworm²⁰⁵ and the morphology of diving beetles²⁰⁶ and bees^{207,208}. However, because of the high cost of MRI machines, only few zoological studies have been performed. Given its unique properties, 'MRI could in fact be used more widely in zoology'²⁰⁹.

In this study we used one of the main features of NMR, namely, that different chemical environments can be separated due to their different chemical shift. As model organism we chose the European spruce bark beetle, *Ips typographus* L. (Coleoptera: Curculionidae: Scolytinae). This beetle is 4 to 6 mm long and has a fresh mass of 10 to 14 mg. We show that NMR microscopy can be used to quantify and visualize fat and water distribution in small living insects.

6.2 Materials and Methods

6.2.1 Animal handling

Freshly emerged *I. typographus* individuals of approximately 5 mm length and 2 mm width were investigated. Beetles originated from the 29th generation of a laboratory rearing. To immobilize beetles, they were cooled to approximately 2°C prior to the experiments. Before transferring the beetles to the NMR microimaging system they were fixed mechanically in their position in a 5 mm Shigemi tube (Shigemi, Allison Park, PA, USA) by glass rods from the top and the bottom. Temperature inside the tube containing the beetle was adjusted to 2°C with a constant nitrogen flow around the glass tube. NMR spectral signal intensities of fat and water of 10 different beetles were correlated to water and lipid amount obtained by conventional measurements (see below).

In addition to NMR spectroscopy, two beetles were examined by NMR microscopy before and after tethered flight. Cooled beetles were warmed up to room temperature after their initial NMR measurement and attached to flight mills for approximately 20 h. Flight mills consisted of a vertical pivot with a rotary arm attached perpendicularly to it. The pivot consisted of a glass microcapillary. To minimize friction, we attached the tips of insect needles to each end of the capillary. The rotary arm was made of a gas chromatography column and its radius was 10.5 cm. Hence, one rotation of the arm corresponded to a flight distance of 0.66 m. Each full rotation of the arm triggered a photo sensor and was recorded using DIAdem version 10.0 (National Instruments, Austin, TX, USA, 2005).

6.2.2 NMR methods

The beetles were analyzed in a 14.1 T NMR microscopy system (BrukerBioSpin, Rheinstetten, Germany) with gradient strengths up to 3 T/m. Magnetic field inhomogeneity was improved by manual shimming up to second order. One-dimensional (1-D) proton spectra of the whole insect without any spatial encoding were acquired with a standard pulse-acquire NMR experiment within 16 averages and a repetition time of 4 s.

In addition to spectroscopy, multi-slice spin echo images with an in-plane resolution of 31 x 31 μm and a slice thickness of 150 μm were acquired. The repetition time was set to $\text{TR} = 1000$ ms, the echo time was set to $\text{TE} = 9.4$ ms, we used a field-of-view (FOV) of 0.8 cm x 0.8 cm, the matrix had a size of 256 x 256 and the overall acquisition time was $t_{\text{acq}} = 4$ min 16 s. Optionally, fat saturation using a 90° Gaussian pulse at 4.0 ppm offset with respect to the proton resonance (bandwidth = 3.5 ppm) was performed before image acquisition. Transverse magnetization was dephased by a spoiler gradient. Before and after flight of the beetles, images with and without fat saturation were taken. Then, the difference of the two pictures yielded the fat distribution. Maps of fat distribution were calculated with ImageJ²¹⁰. The acquisition time for the two images was 8 min 32 s. To identify the spatial distribution of

fat more clearly, pictures with a transparent-zero projection²¹⁰ were produced. High-resolution three-dimensional imaging with an in-plane resolution of 12 μm x 12 μm and a slice thickness of 120 μm of the bark beetles was performed to study the insects' morphology. The repetition time was set to $\text{TR} = 1000$ ms, the echo time was set to $\text{TE} = 7.3$ ms, we used an FOV of 0.6 cm x 0.6 cm, the matrix had a size of 512 x 512 and the overall acquisition time was $t_{\text{acq}} = 7$ h 7 min.

6.2.3 Conventional water and lipid measurements

We determined the water content of the beetles by calculating the difference between their fresh and dry mass. Therefore, beetles were dried at 60°C for 24 h. For conventional destructive fat measurement, beetles were killed in a freezer at - 20°C. They were then cut into three pieces, making incisions between the head and the thorax and between the thorax and the abdomen. Fatty acid esters were extracted from the dissected beetles three times in 1 ml chloroform at 30°C in an ultrasonic bath. The chloroform samples were dried overnight at 65°C. Fat reserves were measured photometrically as fatty acid ester equivalents based on the method of Snyder and Stephens²¹¹, modified after Krauße-Opatz et al.²¹². This measurement is based on a hydroxylaminolysis, in which an ester group forms a hydroxamic acid when reacting with alkaline hydroxylamine. After addition of acid ferric perchlorate, the hydroxamic acid forms a purple iron-chelate complex. This can be measured photometrically at 530 nm. A standard calibration curve for fatty acid esters was calculated based on 10 samples of methyl oleate (Sigma-Aldrich, St Louis, MO, USA) dissolved in chloroform in concentrations between 0.5 and 5.0 μmol in 0.5 μmol steps (Pearson's product-moment correlation: $R^2 > 0.99$, $t = 41.50$, d.f. = 8, $P < 0.0001$, $N = 10$).

6.3 Results and Discussion

6.3.1 Anatomy

Using high-resolution spin-echo imaging, the anatomy of living spruce bark beetle individuals was analyzed. In the acquired oblique coronal slices through the beetle's body, the different body segments such as the head including mouthparts, legs and wings and their respective muscles and intestinal^{213,214} and genital organs²¹⁵ have been identified (Fig. 6.1, see also supplementary material Movie 1). Susceptibility artifacts were greatly reduced by using Shigemi tubes. In addition, the Shigemi tube allowed us to fix the beetle in position and eliminate movement artifacts caused by gradient vibrations. Cooling beetles to 2°C erased all motion artifacts during the measurement without harming them.

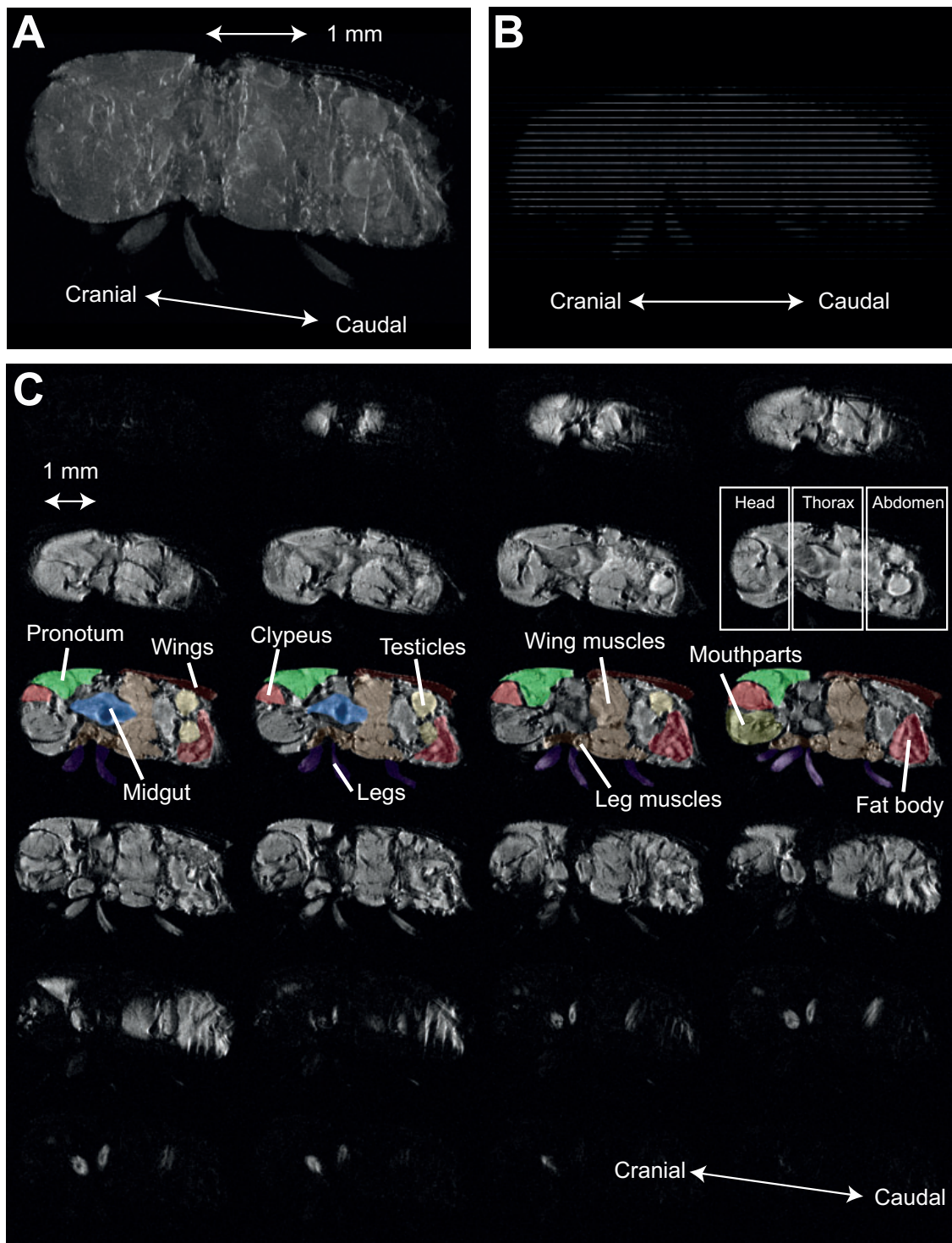


Figure 6.1: (A) Maximum-intensity projection of all slices of the bark beetle *Ips typographus*. (B) Orientation of the reconstructed oblique coronal slices. (C) Oblique coronal slices. Several internal structures and organs can be identified: mouthparts, testicles, mid-gut, wing and leg muscles, and legs.

6.3.2 Spectroscopy

Fat and water content of living bark beetles were investigated by conventional NMR techniques. ^1H -NMR spectra of bark beetles showed a clear chemical shift separation between fat (4.7 ppm) and water (0 ppm), which arises from the different electronic environment of fat and water protons (Fig. 6.2 A). The NMR peak integrals of fat and water of 10 beetles significantly correlated with the data obtained by the destructive standard detection method (Pearson's product-moment correlation: water, $R^2 > 0.99$, $t = 66.04$, d.f. = 8, $P < 0.0001$, $N = 10$; fat, $R^2 > 0.99$, $t = 19.99$, d.f. = 8, $P < 0.0001$, $N = 10$; Fig. 6.2 B,C). Such a set of independent measurements can serve as a calibration of NMR integrals on every NMR spectrometer, relating the dimensionless NMR peak integrals to absolute standard units of fat (nmol) and water (mg) content.

Fat and water content of small insects can therefore be quantitatively analyzed by NMR. In contrast to traditional methods, this technique opens up the possibility to measure one specimen repeatedly, which we demonstrated by determining fat content of two bark beetles before and after tethered flight (Fig. 6.3 C,D, supplementary material Fig. 6.4 C,D).

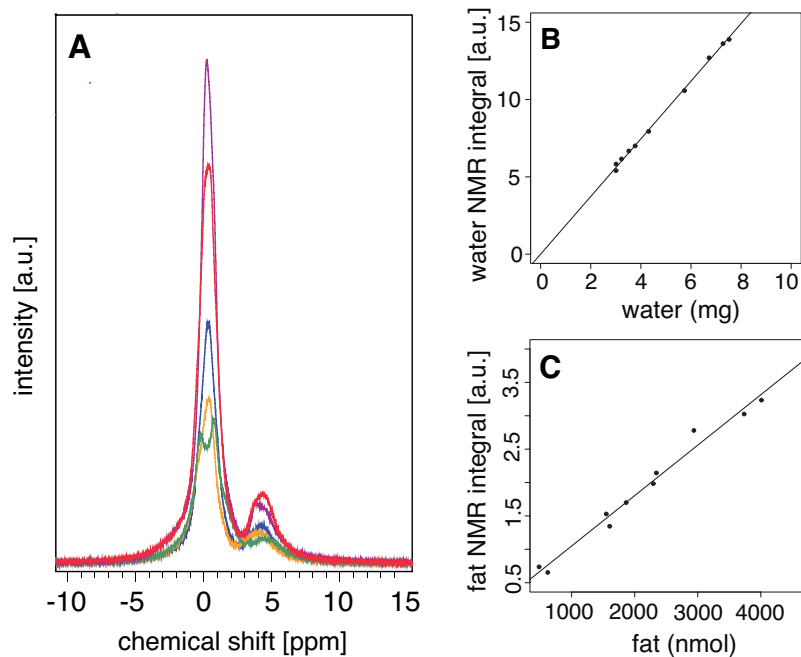


Figure 6.2: (A) Proton nuclear magnetic resonance (NMR) spectra of five bark beetles (indicated by different colors) showing a clear separation between the water peak (0 ppm) and the fat peak (4.7 ppm). The spectra were acquired using a conventional pulse-acquire 1-D NMR experiment with 16 scans. (B) Correlation between NMR and conventional water measurement, $R^2 > 0.99$. (C) Correlation between NMR and conventional fat measurement, $R^2 > 0.99$.

6.3.3 Relative fat distribution

To image the relative spatial distribution of fat in bark beetles, fat saturation was performed before a spin-echo imaging sequence. An image overlay of anatomy images (grey) with the corresponding areas of relative fat distribution (purple) shows where the bark beetles store their energy reserves and where they are used up after flight (Fig. 6.3 A,B, Appendix A Fig. 6.4 A,B). In contrast to standard spectroscopic 1-D methods, signal intensity was not correlated to standard units of fat and water because signal intensities are more prone to errors. Therefore we obtained a relative spatial fat distribution. In addition, absolute quantification of fat and water content, as well as fat and water consumption, was performed by acquiring a standard 1-D proton NMR spectrum (Table 6.1, Fig. 6.3 C,D; see NMR methods).

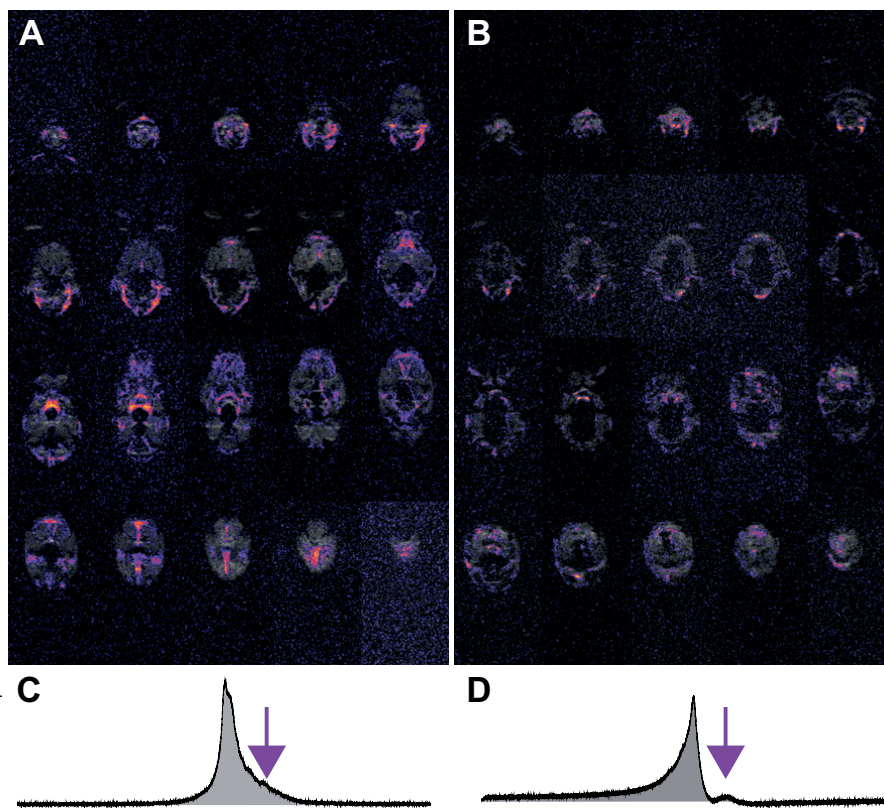


Figure 6.3: (A) Oblique sagittal slices of fat distribution (darker color resembles lower fat amount and brighter color resembles higher fat amount) and proton density (grey tones) before flight in *Ips typographus*. (B) Oblique sagittal slices after flight. (C) NMR spectrum before flight. (D) NMR spectrum after flight. The purple arrows indicate the fat saturation pulse used to obtain spectral information in the images. Quantitative analysis is shown in Table 6.1 (beetle no. 1).

We identified one major fat reservoir in the abdomen of the beetle, most likely the diffuse fat body, and one in the center of the body. Spatial information of the bark beetles has been combined with spectral information, which we can gain because of the spectral separation of fat and water signals. Within 8 min 32 s, two

Beetle no.	Fat [nmol]	Fat [nmol]	consumption [nmol]	Water [mg]	Water [mg]	water loss [mg]	Flight distance [km]
	Before flight	After flight		Before flight	After flight		
1	1519.55	1137.64	381.91	3.64	2.89	0.74	0.34
1	1688.17	1312.71	375.46	4.92	4.13	0.79	13.45

Table 6.1: Covered flight distances and absolute amounts of fat and water content and consumption of two different bark beetles measured by NMR spectroscopy before and after flight

high-resolution images can be acquired, allowing identification of the relative fat distribution within the beetle with regard to its internal morphology before and after flight. This method non-invasively images and, in combination with spectroscopic techniques, quantifies spatial fat consumption in certain areas of interest in a specimen.

6.3.4 Conclusions

Here we demonstrated the potential of NMR microscopy in zoology and especially entomology to follow fat distribution across whole insects and fat consumption in different organs of interest as a function of external parameters over time. It was possible to quantify lipid reserves of living insects giving a direct measure of total stored energy. The method allows monitoring dynamic processes of lipid consumption non-invasively, as we have shown for the energy consumption of bark beetles before and after flight. This study is exemplary for any other non-invasive investigation in zoology and especially entomology, where energy consumption and its spatial distribution in living species are of interest.

6.4 Acknowledgements

The authors thank Axel Gruppe for helpful suggestions and comments during the experiments. F.S. acknowledges financial support from the Fonds der Chemischen Industrie, the Faculty Graduate Center Chemistry, Technische Universität München Graduate School, and the Institute for Advanced Study (IAS) at Technische Universität München. This work was supported by the Bavarian State Ministry for the Environment and Public Health [UGV 06070204028 to K.D.]. S.J.G. acknowledges support from the German Research Foundation (DFG) [GI 203/6-1] and the Fonds der Chemischen Industrie.

6.5 Appendix A: Supplementary figures

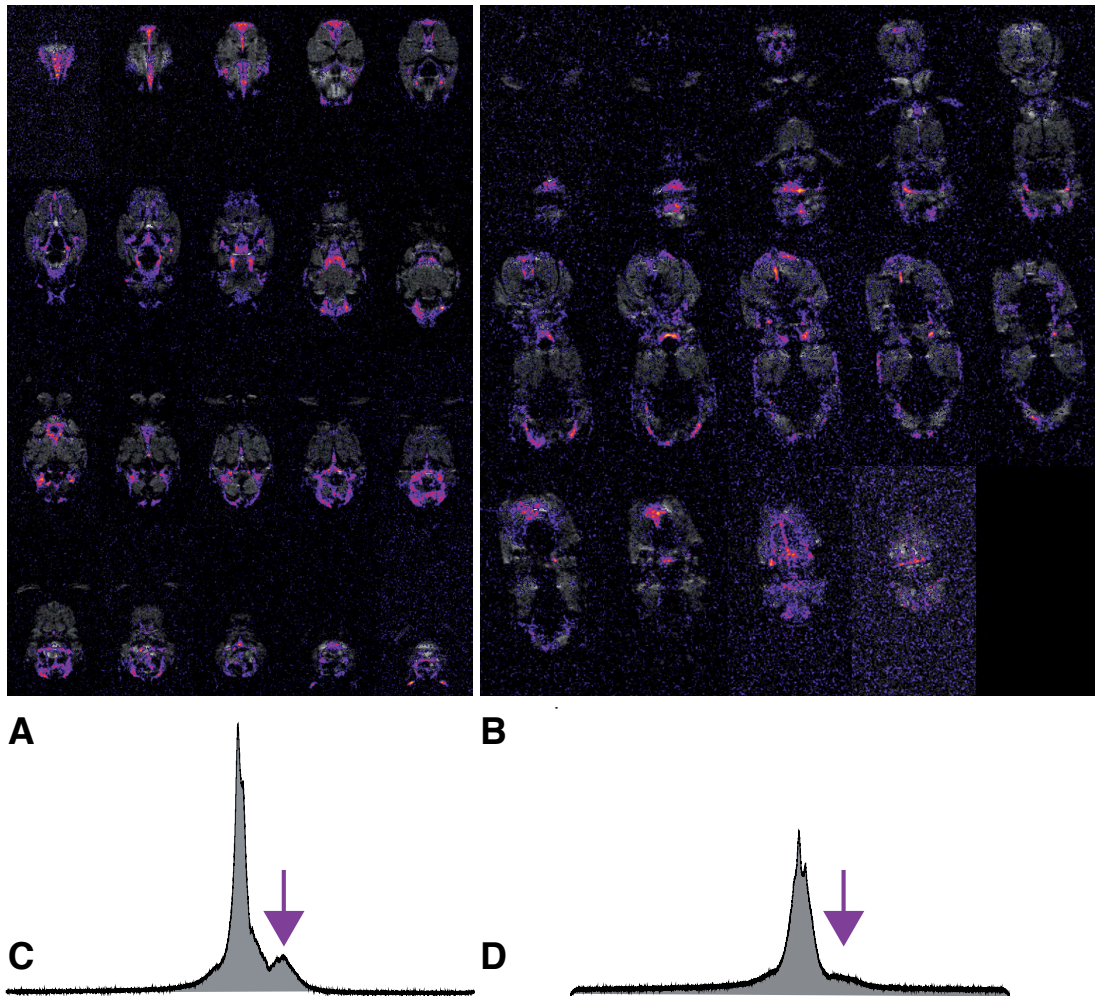


Figure 6.4: (A) Oblique sagittal slices of fat distribution (darker color resembles lower fat amount and brighter color resembles higher fat amount) and proton density (grey tones) before flight in the bark beetle *Ips typographus*. (B) Oblique coronal slices after flight. (C) NMR spectrum before flight, purple arrow indicates fat saturation pulse to obtain spectral information in the images. Quantitative analysis is shown in Table 1, beetle no. 2. (D) NMR spectrum after flight.

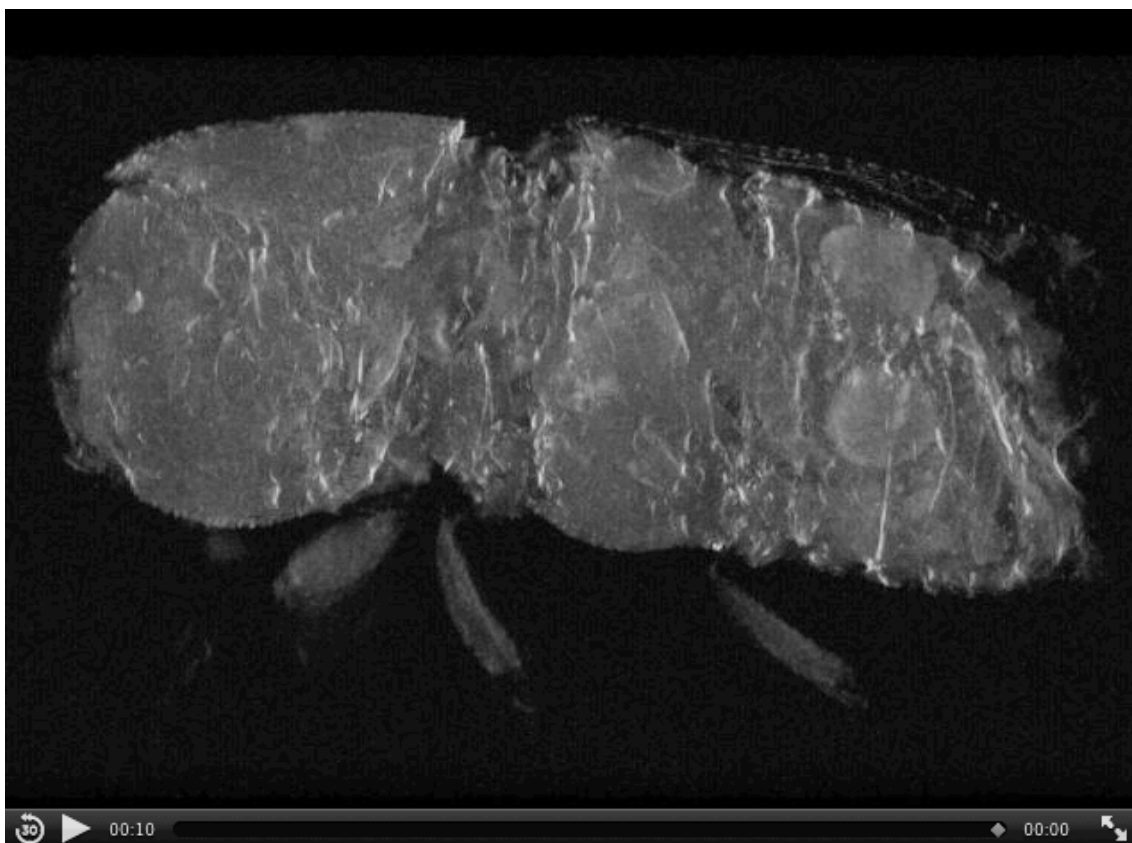


Figure 6.5: Three-dimensional reconstruction of the slices through the bark beetle from Fig. 6.1 in the main text. Maximum intensity projections were calculated with ImageJ. A movie showing the 3D reconstruction from different angles can be found at: <http://jeb.biologists.org/content/suppl/2012/08/22/jeb.071209.DC1/Movie1.avi>.

Conclusion

Novel methods for NMR were developed based on a dual core of optimal control pulse design in combination with hyperpolarization techniques trying to push NMR's capabilities as a diverse tool for applications at the interface of physics, chemistry, biology, and medicine. This enables applications at fundamentally different scales ranging from molecular structure to metabolite diffusion properties in animals. In detail the following major innovations have been achieved in this contribution:

- In **chapter 3**, an extension of the GRAPE tracking algorithm was introduced. With this algorithm, RF pulses for heteronuclear coupled spin systems such as tailored decoupling sequences were optimized. Continuous-wave (CW) decoupling has an intrinsic non-linear offset dependence of the scaling of the effective J -coupling constant. In contrast to CW decoupling we have shown using optimal control pulse optimization that virtually arbitrary off-resonance scaling of the J -coupling constant can be achieved. A new class of tailored decoupling pulses was introduced and named SHOT (Scaling of Heteronuclear couplings by Optimal Tracking). SHOT pulses offer a robust approach of encoding chemical shift information indirectly through off-resonance decoupling, which however made it possible for the first time to achieve linear J scaling as a function of offset frequency. For a simple mixture of eight aromatic compounds, it was demonstrated experimentally that a 1D-SHOT $\{^1\text{H}\}$ - ^{13}C experiment yields comparable information to a 2D-HSQC and can give full assignment of all coupled spins. SHOT pulses offer great potential for reduction of dimensionality without loss of information in pseudo-multidimensional experiments, thereby allowing to reduce measurement time. This might enable high-throughput routine NMR screenings at lower cost.
- A significant challenge in realizing the promise of the dissolution dynamic nuclear polarization (DNP) technique for signal enhancement in high-resolution NMR lies in the non-renewability of the hyperpolarized spin state. This property prevents the application of traditional two-dimensional correlation spectroscopy, which relies on regeneration of spin polarization before each successive increment of the indirect dimension. Seeing this challenge, SHOT decoupling pulses were numerically optimized for applications with DNP as described in **chapter 4**. Vanillin, which contains a number of functional groups

was used as a test molecule allowing the demonstration of SHOT decoupling tailored towards simplified and accurate data analysis. In these measurements, error ranges of ± 0.03 ppm for the indirectly determined ^1H chemical shifts, and of ± 0.4 ppm for the indirectly determined ^{13}C chemical shifts were found. In all cases, we show that chemical shift correlations can be obtained from information contained in a single scan which maximizes the ratio of signal to stochastic noise. A unique feature of this technique is the ability to control the accuracy of chemical shift determination in spectral regions of interest adaptively to the needs within the physical limits. The possibility to obtain chemical shift correlations within a few milliseconds makes SHOT decoupling ideally suited for applications in real-time spectroscopy.

- In **chapter 5**, a method which measures apparent diffusion coefficients (ADCs) of metabolites using hyperpolarized ^{13}C diffusion-weighted spectroscopy was presented. The pulse sequence based on the pulsed gradient spin echo (PGSE) can encode both kinetics and diffusion information. In experiments with MCF-7 human breast cancer cells an ADC of intracellularly produced lactate of $(1.06 \pm 0.15) \mu\text{m}^2/\text{ms}$ was detected, which is about half of the value measured with pyruvate in extracellular culture medium. By these results, clear assignment of the metabolites to their respective compartment was possible. In addition it was shown that ^{13}C ADC detection can yield sensitive information on changes in membrane permeability and subsequent cell death. Our results suggest that both metabolic label exchange and ^{13}C ADCs can be acquired simultaneously and may potentially serve as non-invasive biomarkers for pathological changes in tumor cells. In addition, techniques for robust and accurate determination of ^{13}C -metabolite ADCs *in vivo* were developed. Robust, broadband, and slice-selective refocusing pulses improved by optimal control theory were introduced in this context. First results have demonstrated the feasibility of this promising quantitative technique for preclinical research.
- **Chapter 6** addresses the biologically relevant question how to quantify fat and water content non-invasively in living insects by NMR. In contrast to destructive conventional photometric and mass measurements, we demonstrated exemplarily in the European spruce bark beetle that NMR can be efficiently and accurately used to quantify absolute fat and water content. Additionally, anatomic images with a spatial in-plane resolution up to $10 \mu\text{m}$ and with high soft tissue contrast were acquired. It was demonstrated that fat distribution and fat consumption of living insects can be obtained by magnetic resonance imaging (MRI). This enables future research including observations of specific single individuals by multiple measurements for trend analyses, which is impossible with conventional destructive methods.

In summary, novel NMR methods were developed in this work. Highlights are a technique for quantitative characterization of tumor necrosis and a method for measurements of heteronuclear chemical shift correlations within a single scan.

Bibliography

- [1] F. Bloch, J. H. Hansen, and M. Packard, “The Nuclear Induction Experiment,” *Phys. Rev.*, vol. 70, pp. 474–485, 1946.
- [2] E. M. Purcell, H. C. Torrey, and R. V. Pound, “Resonance absorption by nuclear magnetic moments in a solid,” *Phys. Rev.*, vol. 69, pp. 37–38, 1946.
- [3] R. R. Ernst, G. Bodenhausen, and W. A. Principles of Nuclear Magnetic Resonance in One and Two Dimensions. Oxford: Oxford University Press, 1990.
- [4] P. Mansfield and P. Grannell, “NMR ‘diffraction’ in solids?,” *Journal of Physics C*, vol. 6, pp. L422–L426, 1973.
- [5] P. Lauterbur, “Image Formation by Induced Local Interactions: Examples Employing Nuclear Magnetic Resonance,” *Nature*, vol. 242, pp. 190–191, 1973.
- [6] J. Frahm, K. D. Merboldt, and W. Hänicke, “Functional MRI of human brain activation at high spatial resolution,” *Magn. Reson. Med.*, vol. 29, pp. 139–144, 1993.
- [7] R. Weissleder and U. Mahmood, “Molecular imaging,” *Radiology*, vol. 219, pp. 316–333, 2001.
- [8] C. Witte and L. Schröder, “NMR of hyperpolarised probes,” *NMR Biomed.*, 2012. DOI: 10.1002/nbm.2873.
- [9] J. H. Ardenkjær-Larsen, B. Fridlund, A. Gram, G. Hansson, L. Hansson, M. H. Lerche, R. Servin, M. Thaning, and K. Golman, “Increase in signal-to-noise ratio of > 10,000 times in liquid-state NMR,” *Proc. Natl. Acad. Sci. USA*, vol. 100, pp. 10158–10163, 2003.
- [10] J. Kurhanewicz, D. B. Vigneron, K. Brindle, E. Y. Chekmenev, A. Comment, C. H. Cunningham, R. J. Deberardinis, G. G. Green, M. O. Leach, S. S. Rajan, R. R. Rizi, B. D. Ross, W. S. Warren, and C. R. Malloy, “Analysis of cancer metabolism by imaging hyperpolarized nuclei: prospects for translation to clinical research,” *Neoplasia*, vol. 13, pp. 81–97, 2011.
- [11] F. A. Gallagher, M. I. Kettunen, and K. M. Brindle, “Biomedical applications of hyperpolarized ^{13}C magnetic resonance imaging,” *Prog. NMR Spectrosc.*, vol. 55, pp. 285–295, 2009.
- [12] K. M. Brindle, S. E. Bohndiek, F. A. Gallagher, and M. I. Kettunen, “Tumor imaging using hyperpolarized ^{13}C magnetic resonance spectroscopy,” *Magn. Reson. Med.*, vol. 66, pp. 505–519, 2011.
- [13] R. E. Hurd, Y.-F. Yen, A. Chen, and J. H. Ardenkjær-Larsen, “Hyperpolarized ^{13}C metabolic imaging using dissolution dynamic nuclear polarization,” *J. Magn. Res. Imaging*, vol. 36, pp. 1314–1328, 2012.
- [14] M. H. Levitt, “Singlet nuclear magnetic resonance,” *Annu. Rev. Phys. Chem.*, vol. 63, pp. 89–105, 2012.

- [15] M. H. Levitt, “Symmetrical composite pulse sequences for NMR population inversion 1. Compensation of radiofrequency field inhomogeneity,” *J. Magn. Reson.*, vol. 48, pp. 234–264, 1982.
- [16] M. H. Levitt, “Symmetrical composite pulse sequence for NMR population inversion 2. Compensation for resonance offset,” *J. Magn. Reson.*, vol. 50, pp. 95–110, 1982.
- [17] N. Khaneja, T. Reiss, C. Kehlet, T. Schulte-Herbrüggen, and S. Glaser, “Optimal control of coupled spin dynamics: Design of NMR pulse sequences by gradient ascent algorithms,” *J. Magn. Reson.*, vol. 172, pp. 296–305, 2005.
- [18] B. Luy, K. Kobzar, T. E. Skinner, N. Khaneja, and S. J. Glaser, “Construction of universal rotations from point-to-point transformations,” *J. Magn. Reson.*, vol. 176, pp. 179–186, 2005.
- [19] J. Neves, B. Heitmann, T. Reiss, H. Schor, N. Khaneja, and S. Glaser, “Exploring the limits of polarization transfer efficiency in homonuclear three spin systems,” *J. Magn. Reson.*, vol. 181, pp. 126–134, 2006.
- [20] T. Skinner, K. Kobzar, B. Luy, R. Bendall, W. Bermel, N. Khaneja, and S. Glaser, “Optimal control design of constant amplitude phase-modulated pulses: Application to calibration-free broadband excitation,” *J. Magn. Reson.*, vol. 179, pp. 241–249, 2006.
- [21] N. Gershenson, K. Kobzar, B. Luy, S. Glaser, and T. Skinner, “Optimal control design of excitation pulses that accommodate relaxation,” *J. Magn. Reson.*, vol. 188, pp. 330–336, 2007.
- [22] K. Kobzar, T. E. Skinner, N. Khaneja, S. J. Glaser, and B. Luy, “Exploring the Limits of Excitation and Inversion Pulses II. RF-Power Optimized Pulses,” *J. Magn. Reson.*, vol. 194, pp. 58–66, 2008.
- [23] J. L. Neves, B. Heitmann, N. Khaneja, and S. J. Glaser, “Heteronuclear decoupling by optimal tracking,” *J. Magn. Reson.*, vol. 201, pp. 7–17, 2009.
- [24] Z. Tošner, T. Vosegaard, C. Kehlet, N. Khaneja, S. Glaser, and N. Nielsen, “Optimal control in NMR spectroscopy: Numerical implementation in SIMPSON,” *J. Magn. Reson.*, vol. 197, pp. 120–134, 2009.
- [25] M. Braun and S. J. Glaser, “Cooperative pulses,” *J. Magn. Reson.*, vol. 207, pp. 114–123, 2010.
- [26] M. A. Janich, R. F. Schulte, M. Schwaiger, and S. J. Glaser, “Robust slice-selective broadband refocusing pulses,” *J. Magn. Reson.*, vol. 213, pp. 126–135, 2011.
- [27] P. de Fouquieres, S. G. Schirmer, S. J. Glaser, and I. Kuprov, “Second order gradient ascent pulse engineering,” *J. Magn. Reson.*, vol. 212, pp. 412–417, 2011.
- [28] T. Schulte-Herbrüggen, R. Marx, A. Fahmy, L. Kauffman, S. Lomonaco, N. Khaneja, and S. J. Glaser, “Control aspects of quantum computing using pure and mixed states,” *Philos. Transact. A Math. Phys. Eng. Sci.*, vol. 370, pp. 4651–4670, 2012.
- [29] K. Kobzar, S. Ehni, T. E. Skinner, S. J. Glaser, and B. Luy, “Exploring the limits of broadband 90° and 180° universal rotation pulses,” *J. Magn. Reson.*, vol. 225, pp. 142–160, 2012.
- [30] P. E. Spindler, Y. Zhang, B. Endeward, N. Gershenson, T. E. Skinner, S. J. Glaser, and T. F. Prisner, “Shaped optimal control pulses for increased excitation bandwidth in EPR,” *J. Magn. Reson.*, vol. 218, pp. 49–58, 2012.
- [31] M. Levitt, R. Freeman, and T. Frenkiel, “Broadband heteronuclear decoupling,” *J. Magn. Reson.*, vol. 47, pp. 328–330, 1982.

- [32] A. J. Shaka, J. Keeler, T. Frenkiel, and R. Freeman, "An improved sequence for broadband decoupling: WALTZ-16," *J. Magn. Reson.*, vol. 52, pp. 335–338, 1983.
- [33] S. Bowen and C. Hilty, "Temporal chemical shift correlations in reactions studied by hyperpolarized nuclear magnetic resonance," *Anal. Chem.*, vol. 81, pp. 4543–4547, 2009.
- [34] C. Hilty and S. Bowen, "Applications of dynamic nuclear polarization to the study of reactions and reagents in organic and biomolecular chemistry," *Org. Biomol. Chem.*, vol. 8, pp. 3361–3365, 2010.
- [35] L. Frydman, T. Scherf, and A. Lupulescu, "The acquisition of multidimensional NMR spectra within a single scan," *Proc. Natl. Acad. Sci. USA*, vol. 99, pp. 15858–15862, 2002.
- [36] L. Frydman and D. Blazina, "Ultrafast two-dimensional nuclear magnetic resonance spectroscopy of hyperpolarized solutions," *Nat. Phys.*, vol. 3, pp. 415–419, 2007.
- [37] M. Mishkovsky and L. Frydman, "Principles and progress in ultrafast multidimensional nuclear magnetic resonance," *Annu. Rev. Phys. Chem.*, vol. 60, pp. 429–448, 2009.
- [38] P. Giraudeau and S. Akoka, "Sources of sensitivity losses in ultrafast 2D NMR," *J. Magn. Reson.*, vol. 192, pp. 151–158, 2008.
- [39] S. E. Day, M. I. Kettunen, F. A. Gallagher, D.-E. Hu, M. Lerche, J. Wolber, K. Golman, J. H. Ardenkjaer-Larsen, and K. M. Brindle, "Detecting tumor response to treatment using hyperpolarized ^{13}C magnetic resonance imaging and spectroscopy," *Nat. Med.*, vol. 13, pp. 1382–1387, 2007.
- [40] C. S. Ward, H. S. Venkatesh, M. M. Chaumeil, A. H. Brandes, M. Vancrackinge, H. Dafni, S. Sukumar, S. J. Nelson, D. B. Vigneron, J. Kurhanewicz, C. D. James, D. A. Haas-Kogan, and S. M. Ronen, "Noninvasive detection of target modulation following phosphatidylinositol 3-kinase inhibition using hyperpolarized ^{13}C magnetic resonance spectroscopy," *Cancer Res.*, vol. 70, pp. 1296–305, 2010.
- [41] T. H. Witney, M. I. Kettunen, and K. M. Brindle, "Kinetic Modeling of Hyperpolarized ^{13}C Label Exchange between Pyruvate and Lactate in Tumor Cells," *J. Biol. Chem.*, vol. 286, pp. 24572–24580, 2011.
- [42] H. M. Mc Connell, "Reaction rates by nuclear magnetic resonance," *J. Chem. Phys.*, vol. 28, pp. 430–431, 1958.
- [43] J. M. Park, S. Josan, T. Jang, M. Merchant, Y.-F. Yen, R. E. Hurd, L. Recht, D. M. Spielman, and D. Mayer, "Metabolite kinetics in C6 rat glioma model using magnetic resonance spectroscopic imaging of hyperpolarized $[1-^{13}\text{C}]$ pyruvate," *Magn. Reson. Med.*, vol. 68, pp. 1886–1893, 2012.
- [44] M. L. Zierhut, Y.-F. Yen, A. P. Chen, R. Bok, M. J. Albers, V. Zhang, J. Tropp, I. Park, D. B. Vigneron, J. Kurhanewicz, R. E. Hurd, and S. J. Nelson, "Kinetic modeling of hyperpolarized $^{13}\text{C}_1$ -pyruvate metabolism in normal rats and TRAMP mice," *J. Magn. Reson.*, vol. 202, pp. 85–92, 2009. doi: 10.1016/j.jmr.2009.10.003.
- [45] A. P. Chen, R. E. Hurd, and C. H. Cunningham, "Spin tagging for hyperpolarized ^{13}C metabolic studies," *J. Magn. Reson.*, vol. 214, pp. 319–323, 2012.
- [46] A. Lodi, S. M. Woods, and S. M. Ronen, "Treatment with the MEK inhibitor U0126 induces decreased hyperpolarized pyruvate to lactate conversion in breast, but not prostate, cancer cells," *NMR Biomed.*, 2012. DOI: 10.1002/nbm.2848.

- [47] A. P. Chen, K. Leung, W. Lam, R. E. Hurd, D. B. Vigneron, and C. H. Cunningham, "Design of spectral-spatial outer volume suppression RF pulses for tissue specific metabolic characterization with hyperpolarized ^{13}C pyruvate," *J. Magn. Reson.*, vol. 200, pp. 344–348, 2009.
- [48] S. Josan, Y.-F. Yen, R. Hurd, A. Pfefferbaum, D. Spielman, and D. Mayer, "Application of double spin echo spiral chemical shift imaging to rapid metabolic mapping of hyperpolarized $[1-^{13}\text{C}]$ -pyruvate," *J. Magn. Reson.*, vol. 209, pp. 332–336, 2011.
- [49] P. E. Z. Larson, A. B. Kerr, G. D. Reed, R. E. Hurd, J. Kurhanewicz, J. M. Pauly, and D. B. Vigneron, "Generating Super Stimulated-Echoes in MRI and Their Application to Hyperpolarized C-13 Diffusion Metabolic Imaging," *IEEE Trans. Med. Imag.*, vol. 31, pp. 265–275, 2012.
- [50] M. I. Kettunen, B. W. C. Kennedy, D.-e. Hu, and K. M. Brindle, "Spin echo measurements of the extravasation and tumor cell uptake of hyperpolarized $[1-^{13}\text{C}]$ lactate and $[1-^{13}\text{C}]$ pyruvate," *Magn. Reson. Med.*, 2012. DOI: 10.1002/mrm.24591.
- [51] P. C. Van Zijl, C. T. Moonen, P. Faustino, J. Pekar, O. Kaplan, and J. S. Cohen, "Complete separation of intracellular and extracellular information in NMR spectra of perfused cells by diffusion-weighted spectroscopy," *Proc. Natl. Acad. Sci. USA*, vol. 88, pp. 3228–3232, 1991.
- [52] J. Ackerman and J. Neil, *Biophysics of Diffusion in Cells*. Oxford, UK: Oxford University Press, 2010.
- [53] M. Hoehn-Berlage, "Diffusion-weighted NMR imaging: application to experimental focal cerebral ischemia," *NMR Biomed.*, vol. 8, pp. 345–358, 1995.
- [54] M. E. Moseley, Y. Cohen, J. Mintorovitch, L. Chileuitt, H. Shimizu, J. Kucharczyk, M. F. Wendland, and P. R. Weinstein, "Early detection of regional cerebral ischemia in cats: comparison of diffusion- and T_2 -weighted MRI and spectroscopy," *Magn. Reson. Med.*, vol. 14, pp. 330–346, 1990.
- [55] D. G. Norris, "The effects of microscopic tissue parameters on the diffusion weighted magnetic resonance imaging experiment," *NMR Biomed.*, vol. 14, pp. 77–93, 2001.
- [56] F. Schilling, S. Düwel, U. Köllisch, M. Durst, R. F. Schulte, S. J. Glaser, A. Haase, A. M. Otto, and M. I. Menzel, "Diffusion of hyperpolarized ^{13}C -metabolites in tumor cell spheroids using real-time NMR spectroscopy," *NMR. Biomed.*, vol. 26, pp. 557–568, 2013.
- [57] B. L. Koelsch, K. R. Keshari, T. H. Peeters, P. E. Z. Larson, D. M. Wilson, and J. Kurhanewicz, "Diffusion MR of hyperpolarized ^{13}C molecules in solution," *Analyst*, vol. 138, pp. 1011–1014, 2013.
- [58] P. E. Z. Larson, R. E. Hurd, A. B. Kerr, J. M. Pauly, R. A. Bok, J. Kurhanewicz, and D. B. Vigneron, "Perfusion and diffusion sensitive ^{13}C stimulated-echo MRSI for metabolic imaging of cancer," *Magn. Reson. Imaging*, 2012. DOI: 10.1016/j.mri.2012.10.020.
- [59] W. Kuhn, "NMR microscopy – fundamentals, limits and possible applications," *Angew. Chem. Int. Ed. Engl.*, vol. 29, pp. 1–19, 1990.
- [60] A. Abragam, *Principles of Nuclear Magnetism*. Oxford University Press, 1983.
- [61] J. Keeler, *Understanding NMR Spectroscopy*. John Wiley & Sons Ltd., 2005.
- [62] M. H. Levitt, *Spin Dynamics: Basics of Nuclear Magnetic Resonance*. John Wiley & Sons Ltd., 2008.
- [63] P. T. Callaghan, *Principles of Nuclear Magnetic Resonance Microscopy*. Clarendon Press, Oxford, 1991.

- [64] F. L. C. Cohen-Tannoudji, B. Diu, *Quantum Mechanics*. Hermann, Paris and John Wiley & Sons Ltd., 1977.
- [65] L. Emsley and A. Pines, “Lectures on Pulsed NMR (3rd edition),” in *Proceedings of the International School of Physics Enrico Fermi* (B. Maraviglia, ed.), 1998.
- [66] W. Magnus, “On the exponential solution of differential equations for a linear operator,” *Comm. Pure Appl. Math.*, vol. 7, pp. 649–673, 1954.
- [67] U. Haeberlen, *High Resolution NMR in Solids: Selective Averaging*. New York: Academic Press, 1976.
- [68] A. Shaka and J. Keeler, “Broadband spin decoupling in isotropic liquids,” *Prog. NMR Spectrosc.*, vol. 19, pp. 47–129, 1987.
- [69] M. H. Levitt and R. Freeman, “Composite pulse decoupling,” *J. Magn. Reson.*, vol. 43, pp. 502–507, 1981.
- [70] S. Conolly, D. Nishimura, and A. Macovski, “Optimal control solutions to the magnetic resonance selective excitation problem,” *IEEE Trans. Med. Imag.*, vol. MI-5, pp. 106–115, 1986.
- [71] N. Khaneja, B. Luy, and S. J. Glaser, “Boundary of quantum evolution under decoherence,” *Proc. Natl. Acad. Sci. USA*, vol. 100, pp. 13162–13166, 2003.
- [72] R. A. de Graaf, *In Vivo NMR Spectroscopy*, ch. 8.9, p. 420. John Wiley & Sons, Ltd, 2007.
- [73] D. Suter, V. Schenker, and A. Pines, “Theory of broadband heteronuclear decoupling in multispin systems,” *J. Magn. Reson.*, vol. 73, pp. 90–98, 1987.
- [74] J. Du, X. Rong, N. Zhao, Y. Wang, J. Yang, and R. B. Liu, “Preserving electron spin coherence in solids by optimal dynamical decoupling,” *Nature*, vol. 461, pp. 1265–1268, 2009.
- [75] B. Goodson, “Using injectable carriers of laser-polarized noble gases for enhancing NMR and MRI,” *Concepts in Magnetic Resonance*, vol. 11, pp. 203–223, 1999.
- [76] G. Frossati, “Polarization of ^3He , D_2 (and possibly ^{129}Xe) using cryogenic techniques,” *Nuc. Instrum. Meth. A*, vol. 402, pp. 479–483, 1998.
- [77] N. Biskup, N. Kalechofsky, and D. Candela, “Spin polarization of xenon films at low-temperature induced by ^3He ,” *Physica B*, vol. 329, pp. 437–438, 2003.
- [78] B. M. Goodson, “Nuclear magnetic resonance of laser-polarized noble gases in molecules, materials, and organisms,” *J. Magn. Reson.*, vol. 155, pp. 157–216, 2002.
- [79] T. G. Walker and W. Happer, “Spin-Exchange Optical Pumping of Noble-Gas Nuclei,” *Rev. Mod. Phys.*, vol. 69, pp. 629–642, 1997.
- [80] A.-M. Oros and N. J. Shah, “Hyperpolarized xenon in NMR and MRI,” *Phys. Med. Biol.*, vol. 49, pp. R105–R153, 2004.
- [81] L. Schröder, T. Lowery, C. Hilty, D. Wemmer, and A. Pines, “Molecular imaging using a targeted magnetic resonance hyperpolarized biosensor,” *Science*, vol. 314, pp. 446–449, 2006.
- [82] L. Schröder, L. Chavez, T. Meldrum, and M. Smith, “Temperature-Controlled Molecular Depolarization Gates in Nuclear Magnetic Resonance,” *Angew. Chem. Int. Ed. Engl.*, vol. 47, pp. 4316–4320, 2008.
- [83] L. Schröder, T. Meldrum, M. Smith, T. J. Lowery, D. E. Wemmer, and A. Pines, “Temperature Response of ^{129}Xe Depolarization Transfer and Its Application for Ultrasensitive NMR Detection,” *Phys. Rev. Lett.*, vol. 100, p. 257603, 2008.

- [84] F. Schilling, L. Schröder, K. K. Palaniappan, S. Zapf, D. E. Wemmer, and A. Pines, "MRI thermometry based on encapsulated hyperpolarized xenon," *ChemPhysChem*, vol. 11, pp. 3529–3533, 2010.
- [85] M. Kunth, J. Döpfert, C. Witte, F. Rossella, and L. Schröder, "Optimized Use of Reversible Binding for Fast and Selective NMR Localization of Caged Xenon," *Angew. Chem. Int. Ed. Engl.*, vol. 51, pp. 8217–8220, 2012.
- [86] A. Abragam and M. Goldman, "Principles of dynamic nuclear polarization," *Rep. Prog. Phys.*, vol. 41, pp. 395–467, 1978.
- [87] A. Abragam and M. Goldman, "Nuclear Magnetism: Order and Disorder," *Clarendon Press. Oxford*, 1982.
- [88] J. H. Ardenkjær-Larsen, H. Johannesson, J. S. Petersson, and J. Wolber, "Hyperpolarized molecules in solution," *Methods Mol. Biol.*, vol. 771, pp. 205–226, 2011.
- [89] C. R. Bowers and D. P. Weitekamp, "Nuclear magnetic resonance by measuring reaction yield of spin symmetry species," *Solid State Nucl. Magn. Reson.*, vol. 11, pp. 123–128, 1998.
- [90] J. Natterer and J. Bargon, "Parahydrogen Induced Polarization," *Prog. NMR Spectrosc.*, vol. 31, p. 293, 1997.
- [91] S. B. Duckett and R. E. Mewis, "Application of parahydrogen induced polarization techniques in NMR spectroscopy and imaging," *Acc. Chem. Res.*, vol. 45, pp. 1247–1257, 2012.
- [92] A. W. Overhauser, "Polarization of nuclei in metals," *Phys. Rev.*, vol. 92, pp. 411–415, 1953.
- [93] A. Abragam and W. G. Proctor, "Spin temperature," *Phys. Rev.*, vol. 109, pp. 1441–1458, 1958.
- [94] T. R. Carver and C. P. Slichter, "Polarization of Nuclear Spins in Metals," *Phys. Rev.*, vol. 92, pp. 212–213, 1953.
- [95] S. C. Serra, A. Rosso, and F. Tedoldi, "Electron and nuclear spin dynamics in the thermal mixing model of dynamic nuclear polarization," *Phys. Chem. Chem. Phys.*, vol. 14, pp. 13299–13308, 2012.
- [96] D. Shimon, Y. Hovav, A. Feintuch, D. Goldfarb, and S. Vega, "Dynamic Nuclear Polarization in the solid state: a transition between the cross effect and the solid effect," *Phys. Chem. Chem. Phys.*, vol. 14, pp. 5729–5743, 2012.
- [97] F. A. Gallagher, M. I. Kettunen, D.-E. Hu, P. R. Jensen, R. I. t. Zandt, M. Karlsson, A. Gisselsson, S. K. Nelson, T. H. Witney, S. E. Bohndiek, G. Hansson, T. Peitersen, M. H. Lerche, and K. M. Brindle, "Production of hyperpolarized [1,4- $^{13}\text{C}_2$]malate from [1,4- $^{13}\text{C}_2$]fumarate is a marker of cell necrosis and treatment response in tumors," *Proc. Natl. Acad. Sci. USA*, vol. 106, pp. 19801–19806, 2009.
- [98] S. E. Bohndiek, M. I. Kettunen, D.-e. Hu, T. H. Witney, B. W. C. Kennedy, F. A. Gallagher, and K. M. Brindle, "Detection of tumor response to a vascular disrupting agent by hyperpolarized ^{13}C magnetic resonance spectroscopy," *Mol. Cancer Ther.*, vol. 9, pp. 3278–3288, 2010.
- [99] T. H. Witney and K. M. Brindle, "Imaging tumour cell metabolism using hyperpolarized ^{13}C magnetic resonance spectroscopy," *Biochem. Soc. Trans.*, vol. 38, pp. 1220–1224, 2010.
- [100] A. P. Chen, R. E. Hurd, M. A. Schroeder, A. Z. Lau, Y.-p. Gu, W. W. Lam, J. Barry, J. Tropp, and C. H. Cunningham, "Simultaneous investigation of cardiac pyruvate dehydrogenase flux, Krebs cycle metabolism and pH, using hyperpolarized [1,2- $^{13}\text{C}_2$]pyruvate in vivo," *NMR Biomed.*, vol. 25, pp. 305–311, 2012.

- [101] M. A. Schroeder, H. J. Atherton, M. S. Dodd, P. Lee, L. E. Cochlin, G. K. Radda, K. Clarke, and D. J. Tyler, "The cycling of acetyl-coenzyme A through acetylcarnitine buffers cardiac substrate supply: a hyperpolarized ^{13}C magnetic resonance study," *Circ. Cardiovasc. Imaging*, vol. 5, pp. 201–209, 2012.
- [102] M. A. Schroeder, A. Z. Lau, A. P. Chen, Y. Gu, J. Nagendran, J. Barry, X. Hu, J. R. B. Dyck, D. J. Tyler, K. Clarke, K. A. Connelly, G. A. Wright, and C. H. Cunningham, "Hyperpolarized ^{13}C magnetic resonance reveals early- and late-onset changes to in vivo pyruvate metabolism in the failing heart," *Eur. J. Heart Fail.*, vol. 15, pp. 130–140, 2013.
- [103] C. von Morze, P. E. Z. Larson, S. Hu, K. Keshari, D. M. Wilson, J. H. Ardenkjaer-Larsen, A. Goga, R. Bok, J. Kurhanewicz, and D. B. Vigneron, "Imaging of blood flow using hyperpolarized [^{13}C]urea in preclinical cancer models," *J. Magn. Reson. Imaging*, vol. 33, pp. 692–697, 2011.
- [104] M. R. Clatworthy, M. I. Kettunen, D.-E. Hu, R. J. Mathews, T. H. Witney, B. W. C. Kennedy, S. E. Bohndiek, F. A. Gallagher, L. B. Jarvis, K. G. C. Smith, and K. M. Brindle, "Magnetic resonance imaging with hyperpolarized [$1,4\text{-}^{13}\text{C}_2$]fumarate allows detection of early renal acute tubular necrosis," *Proc. Natl. Acad. Sci. USA*, vol. 109, pp. 13374–13379, 2012.
- [105] C. Laustsen, J. A. Ostergaard, M. H. Lauritzen, R. Nørregaard, S. Bowen, L. V. Søgaard, A. Flyvbjerg, M. Pedersen, and J. H. Ardenkjaer-Larsen, "Assessment of early diabetic renal changes with hyperpolarized [$1\text{-}^{13}\text{C}$]pyruvate," *Diabetes Metab. Res. Rev.*, vol. 29, pp. 125–129, 2013.
- [106] A. Einstein, "Über die von der molekularkinetischen Theorie der Wärme geforderte Bewegung von in ruhenden Flüssigkeiten suspendierten Teilchen," *Annalen der Physik*, vol. 17, p. 549, 1905.
- [107] R. A. de Graaf, *In Vivo NMR Spectroscopy*, ch. 3.4, p. 142. John Wiley & Sons, Ltd, 2007.
- [108] R. A. de Graaf, *In Vivo NMR Spectroscopy*, ch. 3.4, p. 151. John Wiley & Sons, Ltd, 2007.
- [109] E. L. Hahn, "Spin echoes," *Phys. Rev.*, vol. 80, pp. 580–594, 1950.
- [110] E. O. Stejskal and J. E. Tanner, "Spin Diffusion Measurements: Spin Echoes in the Presence of a Time-Dependent Field Gradient," *J. Chem. Phys.*, vol. 42, pp. 288–292, 1965.
- [111] A. Kumar, D. Welti, and R. Ernst, "NMR Fourier Zeugmatography," *J. Magn. Reson.*, vol. 18, pp. 69–83, 1975.
- [112] A. L. Bloom and J. N. Shoolery, "Effects of Perturbing Radiofrequency Fields on Nuclear Spin Coupling," *Phys. Rev.*, vol. 97, pp. 1261–1265, 1955.
- [113] M. Levitt, R. Freeman, and T. Frenkiel, "Broadband decoupling in high-resolution NMR spectroscopy," *Adv. Magn. Reson.*, vol. 11, pp. 47–110, 1983.
- [114] W. A. Anderson and R. Freeman, "Influence of a second radiofrequency field on high-resolution nuclear magnetic resonance spectra," *J. Chem. Phys.*, vol. 37, pp. 85–103, 1962.
- [115] R. Freeman, S. Kempell, and M. Levitt, "Broadband decoupling and scaling of heteronuclear spin-spin interactions in high-resolution NMR," *J. Magn. Reson.*, vol. 35, pp. 447–450, 1979.
- [116] W. P. Aue, D. P. Burum, and R. R. Ernst, "Scaling of heteronuclear spin interactions by multipulse sequences. Practical guidelines," *J. Magn. Reson.*, vol. 38, pp. 375–380, 1980.
- [117] G. A. Morris, G. L. Nayler, A. J. Shaka, J. Keeler, and R. Freeman, "Real-time J scaling in carbon-13 NMR. I. A simple technique for multiplicity determination," *J. Magn. Reson.*, vol. 58, pp. 155–160, 1984.

- [118] R. V. Hosur, "Scaling in one and two dimensional NMR spectroscopy in liquids," *Prog. NMR Spectrosc.*, vol. 22, pp. 1–53, 1990.
- [119] E. R. P. Zuiderweg and S. W. Fesik, "Band-selective heteronuclear decoupling using shaped pulses as an aid in measuring long-range heteronuclear coupling constants," *J. Magn. Reson.*, vol. 93, pp. 653–658, 1991.
- [120] U. Eggenberger, P. Schmidt, M. Sattler, S. J. Glaser, and C. Griesinger, "Frequency-selective decoupling with recursively expanded soft pulses in multinuclear NMR," *J. Magn. Reson.*, vol. 100, pp. 604–610, 1992.
- [121] M. A. McCoy and L. Mueller, "Selective decoupling," *J. Magn. Reson. A*, vol. 101, pp. 122–130, 1993.
- [122] Z. Starcuk Jr., K. Bartusek, and Z. Starcuk, "Heteronuclear broadband spin-flip decoupling with adiabatic pulses," *J. Magn. Reson. A*, vol. 107, pp. 24–31, 1994.
- [123] M. R. Bendall, "Broadband and narrowband spin decoupling using adiabatic spin flips," *J. Magn. Reson. A*, vol. 112, pp. 26–129, 1995.
- [124] R. R. Ernst, "Nuclear magnetic double resonance with an incoherent radio-frequency field," *J. Chem. Phys.*, vol. 45, pp. 3845–3861, 1966.
- [125] H. J. Reich, M. Jautelat, M. Messe, J. Weigert, and J. D. Roberts, "Nuclear magnetic resonance spectroscopy. Carbon-13 spectra of steroids," *J. Am. Chem. Soc.*, vol. 91, pp. 7445–7454, 1969.
- [126] W. V. E. Breitmaier, *¹³C NMR spectroscopy*. Verlag Chemie, Weinheim, 1974.
- [127] S. W. Fesik, H. L. Eaton, E. T. Olejniczak, and R. T. Gampe, "Pseudo-four-dimensional nuclear magnetic resonance by off-resonance decoupling. An approach for distinguishing coupled proton pairs by the frequencies of their attached heteronuclei," *J. Am. Chem. Soc.*, vol. 112, pp. 5370–5371, 1990.
- [128] C. R. R. Grace and R. Riek, "Pseudomultidimensional NMR by spin-state selective off-resonance decoupling," *J. Am. Chem. Soc.*, vol. 125, pp. 16104–16113, 2003.
- [129] W. Kwiatkowski and R. Riek, "Chemical shift-dependent apparent scalar couplings: An alternative concept of chemical shift monitoring in multi-dimensional NMR experiments," *J. Biomol. NMR*, vol. 25, pp. 281–289, 2003.
- [130] R. Keller, C. R. R. Grace, and R. Riek, "Fast multidimensional NMR spectroscopy by spin-state selective off-resonance decoupling (SITAR)," *Magn. Res. Chem.*, vol. 44, pp. 196–205, 2006.
- [131] S. Bowen, H. Zeng, and C. Hilty, "Chemical Shift Correlations from Hyperpolarized NMR by Off-Resonance Decoupling," *Anal. Chem.*, vol. 80, pp. 5794–5798, 2008.
- [132] E. Kupče and R. Freeman, "SPEED: single-point evaluation of the evolution dimension," *Magn. Reson. Chem.*, vol. 45, pp. 711–713, 2007.
- [133] P. W. A. Howe, "Indirect determination of chemical shift by coupling evolution during adiabatic pulses," *J. Magn. Reson.*, vol. 192, pp. 177–182, 2008.
- [134] J. C. Hoch, "Maximum Entropy Signal Processing of Two-Dimensional NMR Data," *J. Magn. Reson.*, vol. 64, pp. 436–44, 1985.
- [135] B. T. Farmer II, "Simultaneous [¹³C, ¹⁵N]-HMQC, A Pseudo-Triple-Resonance Experiment," *J. Magn. Reson.*, vol. 93, pp. 635–641, 1991.

- [136] T. Szyperski, G. Wider, J. H. Bushweller, and K. Wüthrich, "Reduced Dimensionality in Triple-Resonance NMR Experiments," *J. Am. Chem. Soc.*, vol. 115, pp. 9307–9308, 1993.
- [137] E. Kupče, T. Nishida, and R. Freeman, "Hadamard NMR spectroscopy," *Prog. NMR Spectrosc.*, vol. 42, pp. 95–122, 2003.
- [138] P. Schanda, "Fast-pulsing longitudinal relaxation optimized techniques: Enriching the toolbox of fast biomolecular NMR spectroscopy," *Prog. NMR Spectrosc.*, vol. 55, pp. 238–265, 2009.
- [139] H. S. Atreya, "NMR methods for fast data acquisition," *Journal of the Indian Institute of Science*, vol. 90, pp. 87–104, 2010.
- [140] A. E. Bryson and Y.-C. Ho, *Applied Optimal Control*. Hemisphere, Washington, D.C, 1975.
- [141] T. Skinner, T. Reiss, B. Luy, N. Khaneja, and S. Glaser, "Application of optimal control theory to the design of broadband excitation pulses for high resolution NMR," *J. Magn. Reson.*, vol. 163, pp. 8–15, 2003.
- [142] J. S. Waugh, "Theory of Broadband Spin Decoupling," *J. Magn. Reson.*, vol. 50, pp. 30–49, 1982.
- [143] M. Eberstadt, G. Gemmecker, D. F. Mierke, and H. Kessler, "Scalar Coupling Constants - Their Analysis and Their Application for the Elucidation of Structures," *Angew. Chem. Int. Ed. Engl.*, vol. 34, pp. 1671–169, 1995.
- [144] I. Kuprov and C. Rodgers, "Derivatives of spin dynamics simulations," *J. Chem. Phys.*, vol. 131, p. 234108, 2009.
- [145] Y. Liu and J. H. Prestegard, "Multi-dimensional NMR without coherence transfer: Minimizing losses in large systems," *J. Magn. Reson.*, vol. 212, pp. 289–298, 2011.
- [146] S. J. Glaser, "NMR Quantum Computing," *Angew. Chem. Int. Ed.*, vol. 40, pp. 147–148, 2001.
- [147] T. Skinner, T. O. Reiss, B. Luy, N. Khaneja, and S. J. Glaser, "Tailoring the optimal control cost function to a desired output: application to minimizing phase errors in short broadband excitation pulses," *J. Magn. Reson.*, vol. 172, pp. 17–23, 2005.
- [148] S. Bowen and C. Hilty, "Time-resolved dynamic nuclear polarization enhanced NMR spectroscopy," *Angew. Chem. Int. Ed.*, vol. 47, pp. 5235–5237, 2008.
- [149] H. Zeng, S. Bowen, and C. Hilty, "Sequentially acquired two-dimensional NMR spectra from hyperpolarized sample," *J. Magn. Reson.*, vol. 199, pp. 159–165, 2009.
- [150] F. Schilling and S. Glaser, "Tailored real-time scaling of heteronuclear couplings," *J. Magn. Reson.*, vol. 223, pp. 207–218, 2012.
- [151] S. J. Glaser. <http://www.org.chemie.tu-muenchen.de/glaser/Downloads.html>.
- [152] S. Bowen and C. Hilty, "Rapid sample injection for hyperpolarized NMR spectroscopy," *Phys. Chem. Chem. Phys.*, vol. 12, pp. 5766–5770, 2010.
- [153] R. K. Harris, E. D. Becker, S. M. De Menezes, P. Granger, R. E. Hoffman, and K. W. Zilm, "Further conventions for NMR shielding and chemical shifts," *Magn. Reson. Chem.*, vol. 46, pp. 582–598, 2008.
- [154] K. M. Brindle, "NMR methods for measuring enzyme kinetics in vivo," *Prog. NMR Spectrosc.*, vol. 20, pp. 257–293, 1988.

- [155] T. Harris, G. Eliyahu, L. Frydman, and H. Degani, "Kinetics of hyperpolarized $^{13}\text{C}_1$ -pyruvate transport and metabolism in living human breast cancer cells," *Proc. Natl. Acad. Sci. USA*, vol. 106, pp. 18131–18136, 2009.
- [156] G. F. Mason, R. Gruetter, D. L. Rothman, K. L. Behar, R. G. Shulman, and E. J. Novotny, "Simultaneous determination of the rates of the TCA cycle, glucose utilization, alpha-ketoglutarate/glutamate exchange, and glutamine synthesis in human brain by NMR," *J. Cereb. Blood Flow Metab.*, vol. 15, pp. 12–25, 1995.
- [157] F. Wiesinger, I. Miederer, M. I. Menzel, E. Wiedl, M. A. Janich, J. H. Ardenkjaer-Larsen, M. Schwaiger, and R. F. Schulte, "Metabolic rate constant mapping of hyperpolarized ^{13}C pyruvate," in *Proc. Int. Soc. Magn. Res. Med.*, p. 3282, 2010.
- [158] S. Josan, D. Spielman, Y.-F. Yen, R. Hurd, A. Pfefferbaum, and D. Mayer, "Fast volumetric imaging of ethanol metabolism in rat liver with hyperpolarized $[1-^{13}\text{C}]$ pyruvate," *NMR Biomed.*, vol. 25, pp. 993–999, 2012.
- [159] D. M. Spielman, D. Mayer, Y.-F. Yen, J. Tropp, R. E. Hurd, and A. Pfefferbaum, "In vivo measurement of ethanol metabolism in the rat liver using magnetic resonance spectroscopy of hyperpolarized $[1-^{13}\text{C}]$ pyruvate," *Magn. Reson. Med.*, vol. 62, pp. 307–313, 2009.
- [160] P. A. G. Damian, J. I. Sperl, O. Khegai, S. Grott, E. Weidl, M. A. Janich, F. Wiesinger, S. J. Glaser, A. Haase, M. Schwaiger, R. F. Schulte, and M. I. Menzel, "Multi-side kinetic modeling of ^{13}C metabolic MR using $[1-^{13}\text{C}]$ pyruvate," *Proc. Intl. Soc. Mag. Reson. Med.*, vol. 20, p. 4302, 2012.
- [161] R. A. Kauppinen, "Monitoring cytotoxic tumour treatment response by diffusion magnetic resonance imaging and proton spectroscopy," *NMR Biomed.*, vol. 15, pp. 6–17, 2002.
- [162] R. H. El Khouli, M. A. Jacobs, S. D. Mezban, P. Huang, I. R. Kamel, K. J. Macura, and D. A. Bluemke, "Diffusion-weighted Imaging Improves the Diagnostic Accuracy of Conventional 3.0-T Breast MR Imaging1," *Radiology*, vol. 256, pp. 64–73, 2010.
- [163] S. E. Bohndiek, M. I. Kettunen, D. E. Hu, and K. M. Brindle, "Hyperpolarized ^{13}C spectroscopy detects early changes in tumor vasculature and metabolism after VEGF neutralization," *Cancer Res.*, vol. 72, pp. 854–64, 2012.
- [164] C. Malveau, B. Diter, F. Humbert, and D. Canet, "Self-Diffusion Measurements by Carbon-13 NMR Using Radiofrequency Field Gradients," *J. Magn. Reson.*, vol. 130, pp. 131–134, 1998.
- [165] J. Pfeuffer, J. C. Lin, L. DelaBarre, K. Ugurbil, and M. Garwood, "Detection of intracellular lactate with localized diffusion ^1H - ^{13}C -spectroscopy in rat glioma in vivo," *J. Magn. Reson.*, vol. 177, pp. 129–138, 2005.
- [166] J. Valette, M. Chaumeil, M. Guillermier, G. Bloch, P. Hantraye, and V. Lebon, "Diffusion-weighted NMR spectroscopy allows probing of ^{13}C labeling of glutamate inside distinct metabolic compartments in the brain," *Magn. Reson. Med.*, vol. 60, pp. 306–311, 2008.
- [167] R. A. de Graaf, *In Vivo NMR Spectroscopy*, ch. 3.4, p. 147. John Wiley & Sons, Ltd, 2007.
- [168] C. Harrison, C. Yang, A. Jindal, R. J. DeBerardinis, M. A. Hooshyar, M. Merritt, A. Dean Sherry, and C. R. Malloy, "Comparison of kinetic models for analysis of pyruvate-to-lactate exchange by hyperpolarized ^{13}C NMR," *NMR Biomed.*, vol. 25, pp. 1286–94, 2012.
- [169] H. J. Buschmann, E. Dutkiewicz, and W. Knoche, "The Reversible Hydration of Carbonyl Compounds in Aqueous Solution Part II: The Kinetics of the Keto/Gem-diol Transition," *Phys. Chem. Chem. Phys.*, vol. 86, pp. 129–141, 1982.

- [170] M. K. Maroń, K. Takahashi, R. K. Shoemaker, and V. Vaida, "Hydration of pyruvic acid to its geminal-diol, 2,2-dihydroxypropanoic acid, in a water-restricted environment," *Chem. Phys. Lett.*, vol. 513, pp. 184–190, 2011.
- [171] M. Holz and H. Weingärtner, "Calibration in Accurate Spin-Echo Self-Diffusion Measurements Using ^1H and Less-Common Nuclei," *J. Magn. Reson.*, vol. 92, pp. 115–121, 1991.
- [172] C. Amman, P. Meier, and A. E. Merbach, "A simple multinuclear NMR thermometer," *J. Magn. Reson.*, vol. 46, pp. 319–321, 1982.
- [173] M. Holz, S. R. Heil, and A. Sacco, "Temperature-dependent self-diffusion coefficients of water and six selected molecular liquids for calibration in accurate ^1H NMR PFG measurements," *Phys. Chem. Chem. Phys.*, vol. 2, pp. 4740–4742, 2000.
- [174] K.-C. Chung, H.-Y. Yu, and S. Ahn, "Convection Effects on PGSE-NMR Self-Diffusion Measurements at Low Temperature: Investigation into Sources of Induced Convective Flows," *Bull. Korean Chem. Soc.*, vol. 32, pp. 1970–1974, 2011.
- [175] W. B. Butler, "Preparing nuclei from cells in monolayer cultures suitable for counting and for following synchronized cells through the cell cycle," *Anal. Biochem.*, vol. 141, pp. 70–73, 1984.
- [176] W. X. Zong and C. B. Thompson, "Necrotic death as a cell fate," *Genes Dev.*, vol. 20, pp. 1–15, 2006.
- [177] J. V. Sehy, J. J. Ackerman, and J. J. Neil, "Apparent diffusion of water, ions, and small molecules in the *Xenopus* oocyte is consistent with Brownian displacement," *Magn. Reson. Med.*, vol. 48, pp. 42–51, 2002.
- [178] M. D. Silva, T. Omae, K. G. Helmer, F. Li, M. Fisher, and C. H. Sotak, "Separating changes in the intra- and extracellular water apparent diffusion coefficient following focal cerebral ischemia in the rat brain," *Magn. Reson. Med.*, vol. 48, pp. 826–837, 2002.
- [179] A. P. Halestrap and N. T. Price, "The proton-linked monocarboxylate transporter (MCT) family: structure, function and regulation," *Biochem. J.*, vol. 343 Pt 2, pp. 281–299, 1999.
- [180] J. Spitzer, "From water and ions to crowded biomacromolecules: in vivo structuring of a prokaryotic cell," *Microbiol. Mol. Biol. Rev.*, vol. 75, pp. 491–506, 2011.
- [181] F. Wiesinger, E. Weidl, M. I. Menzel, M. A. Janich, O. Khagai, S. J. Glaser, A. Haase, M. Schwaiger, and R. F. Schulte, "IDEAL spiral CSI for dynamic metabolic MR imaging of hyperpolarized $[1-^{13}\text{C}]$ pyruvate," *Magn. Reson. Med.*, vol. 68, pp. 8–16, 2011.
- [182] M. B. Bernstein, K. F. King, and X. J. Zhou, *Handbook of MRI pulse sequences*. Elsevier Academic Press, Burlington USA, 2004.
- [183] Y.-F. Yen, P. Le Roux, D. Mayer, R. King, D. Spielman, J. Tropp, K. Butts Pauly, A. Pfefferbaum, S. VasanaWala, and R. Hurd, " T_2 relaxation times of ^{13}C metabolites in a rat hepatocellular carcinoma model measured in vivo using ^{13}C -MRS of hyperpolarized $[1-^{13}\text{C}]$ pyruvate," *NMR Biomed.*, vol. 23, pp. 414–423, 2010.
- [184] J. Pauly, P. Le Roux, D. Nishimura, and A. Macovski, "Parameter relations for the Shinnar-Le Roux selective excitation pulse design algorithm," *IEEE Trans. Med. Imag.*, vol. 10, pp. 53–65, 1991.
- [185] M. Garwood and L. DelaBarre, "The return of the frequency sweep: designing adiabatic pulses for contemporary NMR," *J. Magn. Reson.*, vol. 153, pp. 155–177, 2001.

- [186] R. F. Nespolo, D. A. Roff, and D. J. Fairbairn, “Energetic trade-off between maintenance costs and flight capacity in the sand cricket (*Gryllus firmus*),” *Funct. Ecol.*, vol. 22, pp. 624–631, 2008.
- [187] W. I. Williams and I. C. Robertson, “Using automated flight mills to manipulate fat reserves in Douglas-fir beetles (Coleoptera: Curculionidae),” *Environ. Entomol.*, vol. 37, pp. 850–856, 2008.
- [188] D. A. Hahn and D. L. Denlinger, “Energetics of insect diapause,” *Annu. Rev. Entomol.*, vol. 56, pp. 103–121, 2011.
- [189] O. Anderbrant and F. Schlyter, “Causes and effects of individual quality in bark beetles,” *Holarctic Ecol.*, vol. 12, pp. 488–493, 1989.
- [190] P. G. May, “Flower selection and the dynamics of lipid reserves in two nectarivorous butterflies,” *Ecology*, vol. 73, pp. 2182–2191, 1992.
- [191] J. Peig and A. J. Green, “New perspectives for estimating body condition from mass/length data: the scaled mass index as an alternative method,” *Oikos*, vol. 118, pp. 1883–1891, 2009.
- [192] A. J. Green, “Mass/length residuals: measures of body condition or generators of spurious results ?,” *Ecology*, vol. 82, pp. 1473–1483, 2001.
- [193] J. Peig and A. J. Green, “The paradigm of body condition: a critical reappraisal of current methods based on mass and length,” *Funct. Ecol.*, vol. 24, pp. 1323–1332, 2010.
- [194] J. A. Dunlop, D. Penney, N. Dalüge, P. Jäger, A. McNeil, R. S. Bradley, P. J. Withers, and R. F. Preziosi, “Computed tomography recovers data from historical amber: an example from huntsman spiders,” *Naturwissenschaften*, vol. 98, pp. 519–527, 2011.
- [195] H. Pohl, B. Wipfler, D. Grimaldi, F. Beckmann, and R. G. Beutel, “Reconstructing the anatomy of the 42-million-year-old fossil *Mengea tertiaria* (Insecta, Strepsiptera),” *Naturwissenschaften*, vol. 97, pp. 855–859, 2010.
- [196] L. Margheri, G. Ponte, B. Mazzolai, C. Laschi, and G. Fiorito, “Non-invasive study of *Octopus vulgaris* arm morphology using ultrasound,” *J. Exp. Biol.*, vol. 214, pp. 3727–31, 2011.
- [197] J. P. Nixon, M. T. Zhang, C. F. Wang, M. A. Kuskowski, C. M. Nowak, J. A. Levine, C. J. Billington, and C. M. Kotz, “Evaluation of a quantitative magnetic resonance imaging system for whole body composition analysis in rodents,” *Obesity*, vol. 18, pp. 1652–1659, 2010.
- [198] F. C. Tinsley, G. Z. Taicher, and M. L. Heiman, “Evaluation of a quantitative magnetic resonance method for mouse whole body composition analysis,” *Obes. Res.*, vol. 12, pp. 150–160, 2004.
- [199] S. C. Lee, K. Kim, J. Kim, S. Lee, J. Han Yi, S. W. Kim, K. S. Ha, and C. Cheong, “One micrometer resolution NMR microscopy,” *J. Magn. Reson.*, vol. 150, pp. 207–213, 2001.
- [200] J. B. Aguayo, S. J. Blackband, J. Schoeniger, M. A. Mattingly, and M. Hintermann, “Nuclear magnetic resonance imaging of a single cell,” *Nature*, vol. 322, pp. 190–191, 1986.
- [201] G. Gassner and J. A. Lohman, “Combined proton NMR imaging and spectral analysis of locust embryonic development,” *Proc. Natl. Acad. Sci. USA*, vol. 84, pp. 5297–5300, 1987.
- [202] U. Skibbe, J. T. Christeller, C. D. Eccles, W. A. Laing, and P. T. Callaghan, “Phosphorus imaging as a tool for studying the pH metabolism in living insects,” *J. Magn. Reson. B*, vol. 108, pp. 262–268, 1995.

- [203] V. C. Behr, S. C. Müller, and D. Mahsberg, “A morphological study of the metamorphosis of butterflies using MR-microscopy at 17.6 T,” in *Proc. ESMRMB, Nr. 290, Leipzig, Germany*, 2011.
- [204] B. A. Goodman, S. C. Gordon, J. A. Chudek, G. Hunter, and J. A. T. Woodford, “Nuclear magnetic resonance microscopy as a non-invasive tool to study the development of lepidopteran pupae,” *J. Insect Physiol.*, vol. 41, pp. 419–424, 1995.
- [205] M. Mapelli, F. Greco, M. Gussoni, R. Consonni, and L. Zetta, “Application of NMR microscopy to the morphological study of the silkworm, *Bombyx mori*, during its metamorphosis,” *Magn. Reson. Imaging*, vol. 15, pp. 693–700, 1997.
- [206] S. Wecker, T. Hörnschemeyer, and M. Hoehn, “Investigation of insect morphology by MRI: assessment of spatial and temporal resolution,” *Magn. Reson. Imaging*, vol. 20, pp. 105–111, 2002.
- [207] D. Haddad, F. Schaupp, R. Brandtm, G. Manz, R. Menzel, and A. Haase, “NMR imaging of the honeybee brain,” *J. Insect. Sci.*, vol. 4, p. 7, 2004.
- [208] B. Tomanek, A. Jasinski, Z. Sulek, J. Muszynska, P. Kulinowski, S. Kwiecinski, A. Krzyzak, T. Skorka, and J. Kibinski, “Magnetic resonance microscopy of internal structure of drone and queen honey bees,” *J. Apic. Res.*, vol. 35, pp. 3–9, 1996.
- [209] A. Ziegler, M. Kunth, S. Mueller, C. Bock, R. Pohmann, L. Schröder, C. Faber, and G. Giribet, “Application of magnetic resonance imaging in zoology,” *Zoomorphology*, vol. 130, pp. 227–254, 2011.
- [210] M. D. A. P. J. Magalhaes and S. J. Ram, “Image processing with ImageJ,” *Biophoton. Int.*, vol. 11, pp. 36–42, 2004.
- [211] F. Snyder and N. Stephens, “A simplified spectrophotometric determination of ester groups in lipids,” *Biochim. Biophys. Acta*, vol. 34, pp. 244–5, 1959.
- [212] B. Krauß-Opatz, U. Köhler, and R. Schopf, “The energetic state of *Ips typographus* L. (Coleoptera: Scolytidae) during the life cycle,” *J. Appl. Entomol.*, vol. 119, pp. 185–194, 1995.
- [213] W. V. Baker and C. L. Estrin, “The alimentary canal of *Scolytus multistriatus* (Coleoptera: Scolytidae): a histological study,” *Can. Entomol.*, vol. 106, pp. 673–686, 1974.
- [214] E. Díaz, O. Arciniega, L. Sánchez, R. Cisneros, and G. Z. niga, “Anatomical and histological comparison of the alimentary canal of *Dendroctonus micans*, *D. ponderosae*, *D. pseudotsugae pseudotsugae*, *D. rufipennis*, and *D. terebrans* (Coleoptera: Scolytidae),” *Ann. Entomol. Soc. Am.*, vol. 96, pp. 144–152, 2003.
- [215] A. A. Calder, “Gross morphology of the soft parts of the male and female reproductive systems of Curculionoidea (Coleoptera),” *J. Nat. Hist.*, vol. 24, pp. 453–505, 1990.

Curriculum vitae

Personal details

Franz Schilling
Gundelindenstr. 3a
80805 München

mobile phone: 0171 6596604
e-mail: fschilling@tum.de

born on 21st of August 1983 in Bayreuth

Academic education and scholarships

- 10/2009-04/2013 **PhD** at the *Technische Universität München*, Department of Chemistry supervised by Prof. Steffen Glaser and Prof. Axel Haase and supported by a **Kekulé doctorate fellowship** from the *Fonds der chemischen Industrie* (grade: "summa cum laude")
- 07/2009 **Master of Science (physics) with honors** at the *Universität Würzburg* within the Elite program Elitenetzwerk Bayern (grade: 1.0, excellent)
- 2004-2009 Scholarship from the *Studienstiftung des deutschen Volkes*
- 05/2008-06/2009 **Master Thesis** at the *University of California, Berkeley* in the laboratory of Prof. Alexander Pines on magnetic resonance imaging with a scholarship from the *Lawrence Berkeley National Lab*
Title of the Master Thesis: "MRI Thermometry Based on Hyperpolarized Xenon Biosensors"
- 03/2008-05/2008 Research internship at the *Max-Planck Institut für Metallforschung* in Stuttgart
Title of the project: "Fabrication and Characterization of thin magnetic films (GMR-elements, NdFeB-systems)"

- 08/2007-11/2007 Bachelor Thesis at the chair of Biophysics (Prof. Peter Jakob) at the *Universität Würzburg*
Title of the Bachelor Thesis: "Characterisation of Magnetite-Nanoparticles for magnetically induced hyperthermia"
- 2003-2004 Civilian service as an "Ecological Year" at the Institut für Seenforschung in Langenargen at Lake Constance
- 1994-2003 Diploma from German secondary school *Spohn-Gymnasium* in Ravensburg qualifying for university admission (grade: 1.0, excellent)

Grants and awards

- 02/2013 ISMRM educational stipend for attendance of the 21th annual meeting in Salt Lake City
- 08/2012-12/2012 COST Short Term Scientific Mission for a research collaboration with Prof. Jan Henrik Ardenkjær-Larsen at *DTU Copenhagen*, within COST Action TD-1103 EuroHyperPol)
- 07/2012 EUROMAR stipend for attendance of the 2012 EUROMAR in Dublin
- 02/2012 ISMRM educational stipend for attendance of the 20th annual meeting in Melbourne
- 03/2010 Stipend from *Wilhelm und Else Heraeus-Stiftung* to join the annual meeting of the German physics association *Deutsche Physikalische Gesellschaft*
- 2008-2009 Scholarship from *Studienstiftung des deutschen Volkes* and *Lawrence Berkeley National Laboratory* for Master Thesis research at *University of California, Berkeley*
- 2003 Ferdinand Porsche price for the best performance in Mathematics & Physics in the Abitur
- 2001 Price winner at *Jugend forscht* state competition (physics) and 1st price at *Landeswettbewerb Mathematik* Baden-Württemberg

List of publications

Peer-reviewed articles

1. **Schilling, F.**, Schröder, L., Palaniappan K. K., Zapf, S., Wemmer, D. E., Pines, A. (2010): MRI Thermometry Based on Encapsulated Hyperpolarized Xenon. *ChemPhysChem*, 11:3529-3533, (cover page article).
2. **Schilling, F.*** , **Dworschak, K.***, Schopf, R., Kühn, R., Glaser, S. J., Haase, A. (2012): Non-invasive lipid measurement in living insects using NMR microscopy. *Journal of Experimental Biology*; 215(18):3137-3141, *contributed equally.
3. **Schilling, F.**, Glaser, S. J. (2012): Tailored real-time scaling of heteronuclear couplings. *Journal of Magnetic Resonance*, 223:207-218.
4. **Schilling, F.**, Düwel, S., Köllisch, U., Durst, M., Schulte, R. F., Glaser, S. J., Haase, A., Otto, A. M., Menzel, M. I. (2013): Diffusion of hyperpolarized ^{13}C metabolites in tumor cell spheroids using real-time NMR spectroscopy, *NMR in Biomedicine*; 26:557-568.
5. Zhang, G.*, **Schilling, F.***, Glaser, S. J., Hilty, C. (2013): Chemical Shift Correlations from Hyperpolarized NMR using a single SHOT. *Analytical Chemistry*; 85:2875-2881, *contributed equally.

Manuscripts in preparation

1. **Dworschak, K.***, **Schilling, F.***, Stoeckle, B. C., Kühn, R., Glaser, S. J., Haase, A., Schopf, R. (2013): The fatter the fitter? Analysis of the relationship between flight capacity and lipid reserves in a scolytid beetle using NMR spectroscopy; *contributed equally.
2. Vejby Sogaard, L.*, **Schilling, F.***, Janich, M. A., Menzel, M. I., Ardenkjær-Larsen, J. H. (2013): Measurement of apparent diffusion coefficients of hyper-

polarized ^{13}C -metabolites *in vivo*; *contributed equally.

3. **Schilling, F.**, Glaser, S. J. (2013): Scaling effective J -splittings larger than the J -coupling constant.

Conference contributions

1. **Schilling, F.**, Schröder, L., Palaniappan, K. K., Zapf, S., Wemmer, D. E., Pines, A. (2010): MRI Thermometry Based on Encapsulated Hyperpolarized Xenon. DPG Spring meeting, Regensburg, Germany, March 21-26, poster presentation.
2. Schröder, L., Meldrum, T., **Schilling, F.**, Wemmer, D. E., Pines, A. (2010): Encapsulated Xenon as an NMR Sensor for Biomedical Applications, Joint EUROMAR and 17th ISMAR Conference 2010, Florence, Italy, July 4-9.
3. **Schilling, F.**, Schröder, L., Palaniappan, K. K., Zapf, S., Wemmer, D. E., Pines, A. (2010): MRI Thermometry Based on Encapsulated Hyperpolarized Xenon. Joint EUROMAR and 17th ISMAR Conference 2010, Florence, Italy, July 4-9, poster presentation.
4. Schröder, L., Meldrum, T., Smith, M., **Schilling, F.**, Denger, P., Zapf, S., Wemmer, D., Pines, A. (2010): Xenon Biosensors for Multi-Purpose Molecular Imaging. World Congress on Medical Physics and Biomedical Engineering 2010, Munich, Germany, pp. 176-179.
5. **Schilling, F.**, Schröder, L., Palaniappan, K. K., Zapf, S., Wemmer, D. E., Pines, A. (2010): MRI Thermometry Based on Encapsulated Hyperpolarized Xenon. Meeting of the German Section of ISMRM 2010, Essen, Germany, September 16-17, oral presentation.
6. **Schilling, F.**, Dworschak, K., Stöckle, B., Kühn, R., Schopf, R., Glaser, S. J., Haase, A. (2011): NMR microscopy of living bark beetles - investigation of fat consumption with regard to internal morphology. ESMRMB annual meeting 2011, DOI: 10.1007/s10334-011-0267-6, Leipzig, Germany, October 2011, oral presentation and e-poster 289.
7. Durst, M., Schulte, R. F., **Schilling, F.**, Weidl, E., Khagai, O., Janich, M. A., Sperl, J. I., Wiesinger, F., Schwaiger, M., Haase, A. (2011): Parallel spiral CSI for metabolic imaging with hyperpolarized ^{13}C . ESMRMB annual meeting 2011, DOI: 10.1007/s10334-011-0268-5, Leipzig, Germany, October 2011.
8. Durst, M., Schulte, R. F., **Schilling, F.**, Weidl, E., Khagai, O., Janich, M. A., Sperl, J. I., Köllisch, U., Wiesinger, F., Schwaiger, M., Haase, A. (2012): Parallel Spiral Chemical Shift Imaging for Metabolic Imaging with Hyperpolarised ^{13}C . Proceedings of the ISMRM 2012, Melbourne, Australia, May 2012.

9. **Schilling, F.**, Düwel, S., Durst, M., Köllisch, U., Ardenkjaer-Larsen, J. H., Gomez Damian, P. A., Schwaiger, M., Schulte, R. F., Glaser, S. J., Haase, A., Otto, A. M., Menzel, M. I. (2012): Compartmentation of MCF-7 Tumour Cell Metabolites Characterised by Hyperpolarised ^{13}C Diffusion-Weighted Spectroscopy. Proceedings of the ISMRM 2012, Melbourne, Australia, May 2012, poster presentation.
10. **Schilling, F.**, Glaser, S. J. (2012): Tailored real-time scaling of heteronuclear couplings. EUROMAR conference, Dublin, Ireland, June 2012, poster presentation.
11. **Schilling, F.**, Ardenkjaer-Larsen, J. H., Janich, M. A., Menzel, M. I., Vejby Søggaard, L.: Measurement of apparent diffusion coefficients of hyperpolarized ^{13}C -metabolites *in vivo*. Proceedings of the ISMRM 2013, Salt Lake City, USA, May 2013, poster presentation.
12. **Schilling, F.**, Düwel, S., Köllisch, U., Durst, M., Schulte, R. F., Glaser, S. J., Haase, A., Menzel, M. I., Otto, A. M. (2012): Ratio of lactate-to-pyruvate apparent diffusion constants is an indicator of necrosis in tumor cells. ISMRM 2013, Salt Lake City, USA, May 2013, e-poster presentation.

Acknowledgements

Let's consider a *Gedankenexperiment*, in which we turn back the time of my dissertation and I would have to start all over again. How would my dissertation look like? Would I choose to solve the same problems? By doing this, I could in principle avoid all dead ends and go straight to the solution of the problems. However, in many cases the unsolved problems were leading the way to the interesting problems themselves. In addition, thinking about and discussing unsolved problems is what makes research fun. So, in the end, I would have to start out with something new. Nevertheless, I'm glad that this was only a thought experiment and that my research has led to this dissertation. There are many people who have supported, helped, and stimulated me on this way. By these few lines without making a claim to be complete I would like to thank:

- Prof. Steffen Glaser for his confidence and support as a mentor, scientific advisor, and creative stimulus from the beginning of my dissertation.
- Prof. Axel Haase for his trust and benefit as a scientific advisor and for many novel and fascinating research ideas.
- Prof. Silvio Aime for being my third examiner and for many interesting discussions.
- Dr. Marion Menzel for introducing me to the field of diffusion measurements by NMR and for her always positive "we can do this"-attitude.
- Dr. Angela Otto for her patience in teaching a physicist biology and for not blaming physics for biology.
- Prof. Jan Henrik Ardenkjær-Larsen, Dr. Lise Vejby Søgaard, Mette Hauge Lauritzen, and Sascha Gude for many exciting discussions and experiments in Copenhagen.
- Prof. Christian Hilty and Guannan Zhang for a very friendly, effective and fruitful collaboration.

- Kai Dworschak, Prof. Reinhardt Schopf, and Prof. Ralph Kühn for bringing the bark beetles from Weihenstephan to Garching.
- Dr. Robert Fisher and Dr. Uwe Sander for having been my allies and office-mates in the Chemistry department.
- Thomas Gaaß for sharing the coffee, the office, and the time at the IMETUM.
- Stephan Düwel for his help in preparing the diffusion manuscript and for his motivation in solving the "unknown-peak-puzzle".
- Ulrich Köllisch, Markus Durst, and Johannes Scholz for riding the bike, risking their lives, and for being the best movie stars ever.
- Dr. Rolf Schulte, Dr. Martin Janich, and Oleksandr Khagai for the good collaboration with GE.
- Dr. Yun Zhang, Ariane Garon, Corey O'Meara, Matthias Budzynski, Dr. Manoj Nimbalkar, Dr. Jorge Neves, Prof. Tom Skinner, and the rest of the Glaser group for the good working atmosphere.
- Dr. Raimund Marx for all kinds of aid with chemical compounds and Frau Fill for help with any kind of organizational problems.
- Josef Hintermair, Dr. Bernhard Gleich, Christine Rümenapp and all members of the IMETUM for the nice atmosphere and a good time.
- Bettina Kracke and Dr. Leif Schröder for an exciting trip to Berlin and the still-ongoing collaboration on micelles.
- My parents for their unconditional support.
- Dorothee Oestreicher for her wholehearted sympathy.